

**SINGLE PARTICLE INVESTIGATION OF DOPAMINE TRANSPORTERS:
TRANSITIONING FROM CULTURED CELLS TO LIVING BRAIN TISSUE**

By

Lucas Benjamin Thal

Dissertation

Submitted to the Faculty of the
Graduate School of Vanderbilt University
in partial fulfillment of the requirements
for the degree of

DOCTOR OF PHILOSOPHY

in

Chemistry

May 8, 2020

Nashville, Tennessee

Approved:

Sandra J. Rosenthal, Ph.D.

Craig W. Lindsley, Ph.D.

Janet E. Macdonald, Ph.D.

Randy D. Blakely, Ph.D.

Copyright © 2020 by Lucas Benjamin Thal
All Rights Reserved

*Dedicated to my family
and
the late Andrew Bledsoe*

ACKNOWLEDGEMENTS

While this dissertation is my own, I could not have seen these projects through without the training, guidance, and participation of other researchers. It truly takes a village to do meaningful science. The highest level of recognition is given to my adviser, Dr. Sandra J. Rosenthal. Thank you for allowing me to join your group and begin my PhD career with you. At the beginning, you agreed to let me be a materials scientist on the bio-side of the lab, bridging the gap. You kept your word by giving me the freedom to go after the probe design project. I am extremely thankful that you nominated me as a candidate for the training grant, allowed me to visit the Molecular Foundry, sent me around the world to present my dissertation work, and encouraged the projects that fed my creative side. Your mentorship was key to my growth as a scientist. I am and will be forever grateful.

Dr. Craig Lindsley, thank you for being so willing to help guide me in my science career and for your efforts as a member of my PhD committee. I always appreciated your invaluable advice for moving forward in my dissertation work. Dr. Janet Macdonald, although I was not studying directly under you, I consider you one of my mentors. I am immensely grateful of the time you took out of your day to offer your advice on science, career options, and life. Thank you. To Dr. Randy Blakely, you took me on as a trainee on the A559V project during your big move to FAU. You remained ever persistent in helping me with experimental design and guiding me in my writing. Thank you for your help in advancing me as a scientist. I also would like to pay special regard to Dr. Bruce Cohen. Meeting you in San Francisco marked a pivotal point in my PhD career. Thank you for being so open to meeting me and having me work at the Molecular Foundry.

I am very fortunate to have been funded by the NIH as a trainee in the Chemistry-Biology

Interface program. I would also like to thank CISR for providing excellent microscopes and expertise.

Thanks to my colleagues in the Rosenthal Lab for your help and support through the years. First, I would like to thank the trusty bio-side of the lab, especially Dr. Oleg Kovtun. Your help was priceless to me and I could not have done this without you. I always appreciated our chats, whether it be science or music. It was rich and filled with many fun memories. Dr. Ian Tomlinson, I am grateful for your contributions to my dissertation work. Dr. Danielle Bailey – thank you for helping me get acquainted with the lab and helping me through the tough times. I appreciated your participation in group meeting, helping me work through ideas and encourage me to keep going. Ruben, I've enjoyed our chats in the lab. Your drive and willingness to learn will serve you well in the Rosenthal lab. I am indebted to Dr. James McBride. My success in this dissertation work could not have been possible without your mentorship. First, your enormous contribution to my dissertation is acknowledged. I enjoyed traveling with you and learning how to get the most out of conferences. I am so glad I chose the desk next to yours and tremendously thankful to have had you as a mentor throughout these years. Dr. Kemar Reid, thank you for contributing your thoughts and advice on my science. I deeply appreciate our time in the lab and chats surrounding all things music and life in general. Cara, I am enormously thankful for our friendship. Thank you for always talking with me during the tough times and having my back. Your natural ability to find solutions in life and research has not gone unnoticed. I am certain you will be an asset wherever you land after graduate school. Sophie, your unbridled spirit and excitement for science is great for the lab. I very much enjoyed times with you, whether it was in the lab or checking out concerts. Good luck to everyone!

During my PhD, The Vanderbilt community has been a domain of intelligent, creative, and

thoughtful members. Particular mention is deserved for Sarah Ross for encouraging me to apply to graduate school. Sarah, I appreciate all your advice and you always looking out for my best interest. To Dr. Kristina Kitko, thank you for your willingness to give a helping hand, guiding me through graduate school and networking. I would like to especially acknowledge Quinn Bumpers, Ben Mueller, Dan Jefferies, Drew Kellum, and Ross Koby. I truly enjoyed our times out of the lab, and our collective enthusiasm to do good science. Your friendship has been invaluable. Stephanie Castillo, thank you for always willing to lend a listening ear. I believe your passion in STEM communication, and your grad school story will inspire many students. Special thanks to the Wright Lab members, particularly Kelly Richardson for help with experimental design and help in the cell room. Kelly, I am very grateful to have you as one of my close friends in grad school. Ron Benning and Jade Bing, you have been wonderful roommates and true friends. From Olive, Moe and me, thank you!

I wish to acknowledge my close circle of friends, Ben and Jillian Savage, and Caleb Myers, who have supported me since I veered toward a path in science, thank you. You three are talented in massive measure and you have thirst for life which I have admired greatly. I am forever grateful to have you as lifelong friends. To Liliya, thank you for your love and encouragement the last few months of my time in grad school. I am excited to travel and dance around the world with you.

To my loving family, your love and support are paramount to me. Mom and Dad, you always encouraged me go beyond the pale and take risks in life, to explore the world and never let me lose my curiosity. You instilled my fascination in the commonplace. While you always inspired me to go after my passions in life, you supported me when my passions came with pain. I am forever grateful. To my incredibly talented and loving brother, Max, thank you for your unconditional support. I am so proud of you and I truly believe you will inspire the world.

TABLE OF CONTENTS

	Page
DEDICATION	iii
ACKNOWLEDGEMENTS	iv
LIST OF TABLES	xi
LIST OF FIGURES	xii
LIST OF ABBREVIATIONS.....	xv
Chapter	
1 Introduction.....	1
1.1 Mental Illness in the World Today.....	1
1.2 Optical Microscopy in Neuroscience and the Need for Single Molecule Imaging.....	4
1.3 Quantum Dots as Probes for Single Molecule Imaging.....	7
1.4 Dissertation Outline.....	11
1.5 References	12
2 Experimental Methods	17
2.1 Mammalian Cell Culture and Tissue Preparation	17
2.1.1 HEK-293 and SK-N-MC Cells.....	17
2.1.2 Transfection of DAT Coding Variants	18
2.1.3 Acute Mouse Brain Slice Preparation	18
2.3 Single Quantum Dot Labeling and Fluorescence Microscopy of Biological Samples	19
2.3.1 Transiently Transfected DAT-expressing Cell Culture.....	19
2.3.2 Acute Striatal Brain Slices.....	20

2.4 Data Analysis	20
2.4.1 Single Quantum-dot Trajectory Generation	20
2.4.2 Mean Square and 5 Second Displacement	21
2.4.3 Target Cluster Propensity	22
2.5 Generation and Characterization of Quantum Dot Conjugates for Brain Slice Imaging....	22
2.5.1 Synthesis of Symmetrically Shelled CdSe/CdS QDs.....	22
2.5.2 Passivation of Core-shell CdSe/CdS QDs by an Amphiphilic Copolymer	24
2.5.3 QD-Cy5 Conjugation and Amine/QD Quantification.....	24
2.5.4 IDT725SE Synthesis	25
2.5.5 Surface Conjugation of Ligands.....	25
2.5.6 Dynamic Light Scattering.....	26
2.5.7 Electron Microscopy and Energy-dispersive X-ray Spectroscopy.....	26
2.5.8 Ensemble Spectroscopy	26
2.5.9 Time-Resolved Photoluminescence	27
2.5.10 Single QD Fluorescence Analysis	27
2.5.11 Surface-enhanced Raman Spectroscopy of QD Conjugates	28
2.6 QD-based Approach to Survey Endocytosed DAT	28
2.7 References	29
3 Single Quantum Dot Imaging Reveals PKCβ-Dependent Alterations in Membrane Diffusion and Clustering of an Attention-Deficit Hyperactivity Disorder/Autism/Bipolar Disorder-Associated Dopamine Transporter Variant.....	30
3.1 Introduction	30
3.2 Results and Discussion.....	33
3.2.1 Single QD Tracking Analysis Reveals DAT Val559 Has Aberrant Membrane Diffusion.....	34
3.2.2 DAT Val559 Membrane Mobility is Insensitive to PMA-Triggered PKC Activation but Can Be Diminished by PKC β Inhibition.....	36

3.2.3 A559V-Induced Ser53 Phosphorylation Increases Membrane DAT Mobility.	40
3.2.4 DAT Val559 Exhibits Reduced Clustering at the Apical Surface of HEK-293 Cells.	42
3.3 Conclusions	46
3.4 References	48
4 Ligand-conjugated Quantum Dots for Fast Sub-diffraction Protein Tracking in Acute Brain Slices	56
4.1 Introduction	56
4.2 Results and Discussion.....	58
4.2.1 Chemically Mapping Structural Differences in Core/Shell Aqueous Probes	58
4.2.2 Ensemble Photophysical Investigation.....	60
4.2.3 Single QD Analysis in Biological Media	62
4.2.4 Imaging Ligand-conjugated SPT Probes in Acute Brain Slices.....	66
4.3 Conclusions	71
4.4 References	71
5 Conclusion	78
5.1 Concluding Remarks	78
5.2 Future Directions.....	79
5.2.1 Interplay Between DAT and Membrane Binding Partners	79
5.2.2 Linking Endogenous DAT Membrane Dynamics to Animal Model Pathology	80
5.3 References	81
Appendix A - Supporting Information for Chapter III: Single Quantum Dot Imaging Reveals PKC β -Dependent Alterations in Membrane Diffusion and Clustering of an Attention-Deficit Hyperactivity Disorder/Autism/Bipolar Disorder-Associated Dopamine Transporter Variant ...	82
Appendix B - Supporting Information for Chapter IV: Ligand-conjugated Quantum Dots for Fast Sub-diffraction Protein Tracking in Acute Brain Slices	88
Appendix C - Quantum Dot Toolbox in Membrane Neurotransmitter Transporter Research	99
C.1 Introduction	99

C.2 Materials	101
C.3 Subcellular Localization of QD-Bound Neurotransmitter Transporters	102
C.3.1 Protocol	104
C.3.2 Experimental Considerations	105
C.4 Flow Cytometric Detection of Quantum Dot-Labeled Neurotransmitter Transporters in Single Cells	106
C.4.1 Protocol	108
C.4.2 Experimental Considerations	109
C.5 Single Particle Tracking of Neurotransmitter Transporters	110
C.5.1 Protocol	113
C.5.2 Experimental Considerations	113
C.6 References	114
Appendix D - QD-Based Approach to Survey 3D Distribution and Dynamics of Endocytosed Transporters	116
D.2 References	119
Appendix E - Verification of an Intact QD-IDT725 Conjugate by Surface-Enhanced Raman Spectroscopy	120
E.2 References	123
Appendix F - Structural Confirmation of IDT725-Succinimidyl Ester	124
Appendix G - Single Particle Analysis of Cadmium-free Quantum Dots in Ambient Atmosphere	129
F.2 References	133

LIST OF TABLES

Table	Page
A.1. N for each population of trajectories analyzed in both HEK-293 and SK-NMC Cells.....	82
B.1. Time-resolved PL lifetimes and relative amplitudes of (c) QD655s and (d) symmetrically shelled (symm-shelled) CdSe/CdS QDs.....	88
B.2. Summary of statistics value outputs from data analysis using bootstrap-coupled estimation (DABEST).....	95

LIST OF FIGURES

Figure	Page
1.1. The leading disease categories contributing to total United States disability is quantified using Disability Adjusted Life Years (DALY).....	2
1.2. Representative traces of mood states over time for bipolar disorder type I (top trace), type II (middle trace), and unipolar disorder (bottom trace).....	3
1.3. Two established approaches for QD labeling of neuronal proteins.....	8
1.4. DAT regulation separated into two trafficking modes.....	10
1.5. Sequence locations of DAT mutations associated to neurological diseases: ADHD, autism spectrum disorder, bipolar disorder, and dopamine transporter deficiency syndrome.....	11
3.1. Schematic outlining single QD-DAT labeling architecture and chemical structure of the DAT-specific IDT444 affinity tool.....	32
3.2. DAT Val559 exhibits faster mobility compared to that of DAT Ala559 transiently expressed in HEK-293 cells.....	35
3.3. DAT Val559 diffusion is unresponsive to protein kinase C (PKC) activation and is attenuated by PKC β inhibition in HEK-293 cells.....	37
3.4. Phosphomimetic YFP-DAT S/D exhibits faster membrane mobility than that of wild-type YFP-DAT in HEK-293 cells.....	39
3.5. S53 phosphorylation alters mobility of DAT and DAT Val559.....	41
3.6. Intensity-based widefield imaging analysis reveals clusters at the apical cell surface.....	44
3.7. DAT Val559 has a lower propensity to reside in clusters at the apical surface of HEK-293 cells.....	45
4.1. Elemental characterization of CdSe/CdS QD architectures.....	59
4.2. Ensemble photophysical profiles of symmetrically shelled (symm-shelled) CdSe/CdS QDs and QD655s in HEPES buffer or oxygenated cerebrospinal fluid (aCSF).....	62
4.3. Time series and blinking behavior of single QDs.....	65
4.4. (a) Acute brain slice imaging with CdSe/CdS QDs.....	67

4.5. Detection and tracking analysis of QD probes in acute brain slices.....	69
A.1. DAT Val559 exhibits faster mobility compared to wild-type DAT transiently expressed in SK-N-MC cells	84
A.2. DAT Val559 diffusion is unresponsive to protein kinase C (PKC) activation and attenuated by PKC β inhibition in SK-N-MC cells.....	85
A.3. Phosphomimetic YFP-DAT S/D exhibits faster membrane mobility than wild-type YFP-DAT in SK-N-MC cells	87
B.1. Transmission electron microscopy (TEM) particle sizing of symmetrically shelled (symm-shelled) QDs.....	89
B.2. High-resolution transmission electron microscopy (HRTEM) of (a) QD655s and (b) symm-shelled QDs.....	90
B.3. Individual scanning transmission electron microscopy (STEM) images including high angle annular dark field (HAADF, grey) and Cd (red), S (blue) and Se (green) chemical maps for QD655s	91
B.4. Individual scanning transmission electron microscopy (STEM) images including high angle annular dark field (HAADF, grey) and Cd (red), S (blue) and Se (green) chemical maps for symmetrically shelled (symm-shelled) CdSe/CdS QDs	92
B.5. Energy-dispersive X-ray spectrum of symmetrically shelled (symm-shelled) CdSe/CdS QDs.	93
B.6. (a) Dynamic light scattering size measurement of as-synthesized (hydrophobic, black) and PAOA-wrapped (aqueous, blue) symmetrically shelled CdSe/CdS QDs.....	94
B.7. Wide-window energy-dispersive X-ray spectrum of QD655s.....	95
B.8. Narrow-window energy-dispersive X-ray spectrum of QD655s highlighting little to no Zn signal.	96
B.9. Data analysis using bootstrap-coupled estimation (DABEST).....	97
C.1. Quantum dot toolbox in NTT studies.....	100
C.2. Visualization of NTT subcellular localization using laser-scanning confocal microscopy.	104
C.3. Flow cytometric detection QD-labeled cells transiently expressing NTT of interest	107
C.4. Typical video frame sequence of single QDs bound to NTT molecules.	112
C.5. Basic analysis of example trajectories shows plots of displacement from the starting position and MSD for a confined (red) and freely diffusing (blue) particle.....	112

D.1. Spinning-disk confocal microscopy and single QD localization to analyze endocytosed DAT	118
E.1. Surface-enhanced Raman spectroscopy (SERS) of QD-IDT725 using Ag nanoparticle substrates.....	121
E.2. Comparison of commercially available SERS substrates (Ocean Optics) to in-house produced paper-based SERS substrates.....	122
E.3. Determining the effectiveness of the in-house produced SERS substrates.....	123
F.1. HMBC of IDT725SE (600 MHz, CDCl ₃)	125
F.2. HMBC of IDT725SE (600 MHz, CDCl ₃ , subset around ¹³ C 172 ppm).....	126
F.3. HSQC of IDT725SE (600 MHz, CDCl ₃)	127
F.4. COSY of IDT725SE (600 MHz, CDCl ₃)	128
G.1. Elemental characterization of thick-shell InP–ZnSe QDs.	132
G.2. Blinking trace and intensity histogram of an individual thick-shell InP-ZnSe QD recorded in air using a low energy excitation source (488 nm, 2.5 eV)	132

LIST OF ABBREVIATIONS

aCSF - artificial cerebrospinal fluid
ADE - anomalous dopamine efflux
ADHD - attention-deficit/hyperactive disorder
ADI-R - Autism Diagnostic Interview
ADOS - Autism Diagnostic Observational Schedule
AMPA - α -amino-3-hydroxy-5-methyl-4-isoxazolepropionic acid receptor
AMPH - amphetamine
ASD - autism spectrum disorder
BPD - bipolar disorder
BSA - bovine serum albumin
COSY - correlation spectroscopy
D - diffusion coefficient
D2R - dopamine D2 receptor
DABEST - bootstrap-coupled estimation
DALY - disability adjusted life year
DAT - dopamine transporter
DMSO - dimethyl sulfoxide
DSM-V - Diagnostic and Statistical Manual of Mental Disorders
EDC - N-(3-Dimethylaminopropyl)-N'-ethylcarbodiimide
EDS or EDX - energy-dispersive X-ray spectroscopy
EMCCD - electron multiplying charge coupled device
Enz - enzastaurin
FBS - fetal bovine serum
FRAP - fluorescence recovery after photobleaching
GABA - gamma amino butyric acid
GFP - green fluorescent protein
GlyR - glycine receptor
HEPES - 4-(2-hydroxyethyl)-1-piperazineethanesulfonic acid

HMBC - heteronuclear multiple bond correlation
HRTEM - high-resolution transmission electron microscopy
HSQC - heteronuclear single quantum coherence
ID - integrated density
IDT307 or APP+ - 4-(4-dimethylamino)phenyl-1-methylpyridinium
MES - 2-(N-morpholino)ethanesulfonic acid
mGluR - metabotropic glutamate receptor
MPP+ - 1-methyl-4-phenylpyridinium
MSD - mean square displacement
M β CD - methyl- β -cyclodextrin
NHS - N-hydroxysuccinimide (NHS)
NMDAR - N-methyl-D-aspartate receptor
NMR - nuclear magnetic resonance
NTT - neurotransmitter transporters
ODE - 1-octadecene
ODPA - octadecylphosphonic acid
PALM - photoactivated localization microscopy
PAOA - poly(acrylic acid)-*co*-poly(*n*-octylacrylamide)-*co*-poly(2-aminoethylacrylamide)
PBS - phosphate buffer saline
PD - Parkinson's disease
PEG - polyethylene glycol
PIP₂ - phosphatidylinositol 4,5-bisphosphate
PKC - protein kinase C
PL - photoluminescence
PMA - Phorbol-12-myristate-13-acetate
PSD - postsynaptic density protein 95
PSF - point spread function
PVP - polyvinyl pyrrolidone
QD - quantum dot
Q-Q - quantile-quantile
QY - quantum yield

SavQD - streptavidin-conjugated QD
SBR - signal-to-background ratio
sCMOS - scientific complementary metal oxide semiconductor
SE - succinimidyl ester
SERS - surface-enhanced Raman spectroscopy
SERT - serotonin transporter
SNR - signal-to-noise ratio
SPAD - single-photon avalanche photo-diode
SPT - single particle tracking
STEM - scanning transmission electron microscopy
TALM - tracking and localization microscopy
TIRF - total internal reflection fluorescence
TM12 - transmembrane domain 12
TOP - trioctylphosphine
TRPL - time-resolved photoluminescence
WHO - World Health Organization
WT - wild-type
YFP - yellow fluorescent protein
YLD - years lived with disability
YLL - years of life lost to premature mortality
 β -CFT or WIN 35,428 - β -Carbomethoxy-3- β -(4-fluorophenyl)tropane

CHAPTER I

INTRODUCTION

1.1 Mental Illness in the World Today

Neuropsychiatric disorders severely harm the well-being of individuals, their families, and society on a global scale. Whether evaluated in regard to their detrimental effects on education, work life, or overall health, there is no denying the severity of their societal impact. In an effort to help guide countries to accurately assess their healthcare investment needs, the World Health Organization (WHO) devised a method for quantifying global burden of diseases.¹ One of the primary metrics used was the disability adjusted life year (DALY), calculated by summing the years of life lost to premature mortality (YLL) and the years lived with disability (YLD) in a given population.¹ The 2010 World Health Report determined that neuropsychiatric disorders rank third worldwide in DALY values.² Profoundly, these disorders are the leading cause of disability in the United States alone, accounting for 18.6% of total DALY values (Figure 1.1).² These complex and often misunderstood brain disorders inflict suffering on millions, even eclipsing the global burden of cancer.² Some of the more disabling neurological disorders are bipolar disorder and autism spectrum disorder, in which an estimated 2.8% and 1.7% of Americans are diagnosed, respectively.¹

While normal mood changes may be common occurrences, they can drastically impair quality of life when amplified in magnitude, duration, or frequency. Bipolar disorder is a recurrent neurological disorder marked by oscillations in both mood and energy.³ The fifth edition of the Diagnostic and Statistical Manual of Mental Disorders (DSM-V) classifies it into several subtypes:

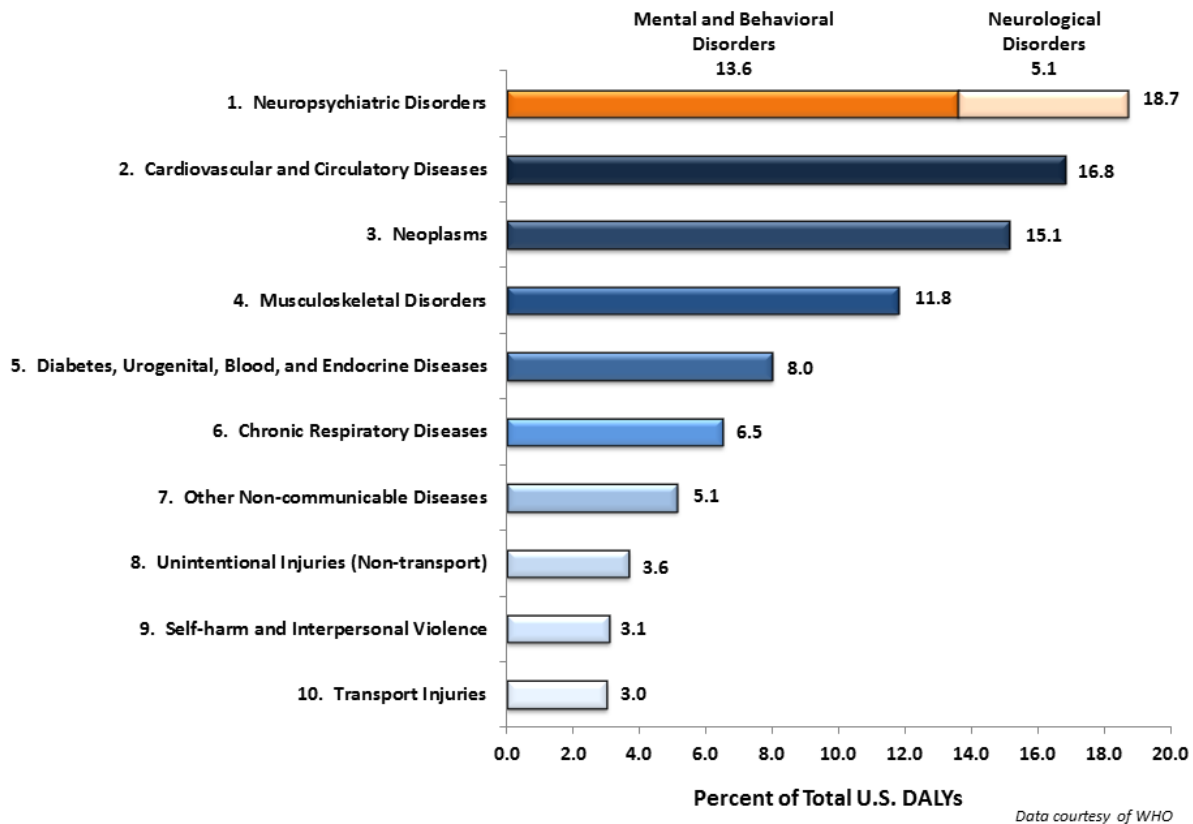


Figure 1.1. The leading disease categories contributing to total United States disability is quantified using Disability Adjusted Life Years (DALY). This graphic was reproduced with permission from the National Institution of Mental Health.¹

(i) *bipolar disorder type I* characterized by episodes of depression and at least one episode of peak mania, (ii) *bipolar disorder type II* characterized by several protracted depression episodes, at least one hypomanic episode, but no manic episodes. Other subtypes like *cyclothymic disorder* and *bipolar disorder not otherwise specified* are in place when some symptoms of mood disorders are exhibited by patients, but fail to satisfy diagnostic criteria. Effectively, the need for the DSM to include these other “fail-to-characterize” subtypes underline the ambiguity in bipolar disorder diagnosis. This disorder is particularly difficult to diagnose accurately due to the challenges in differentiating type I or type II from unipolar disorder, another affective disorder characterized by

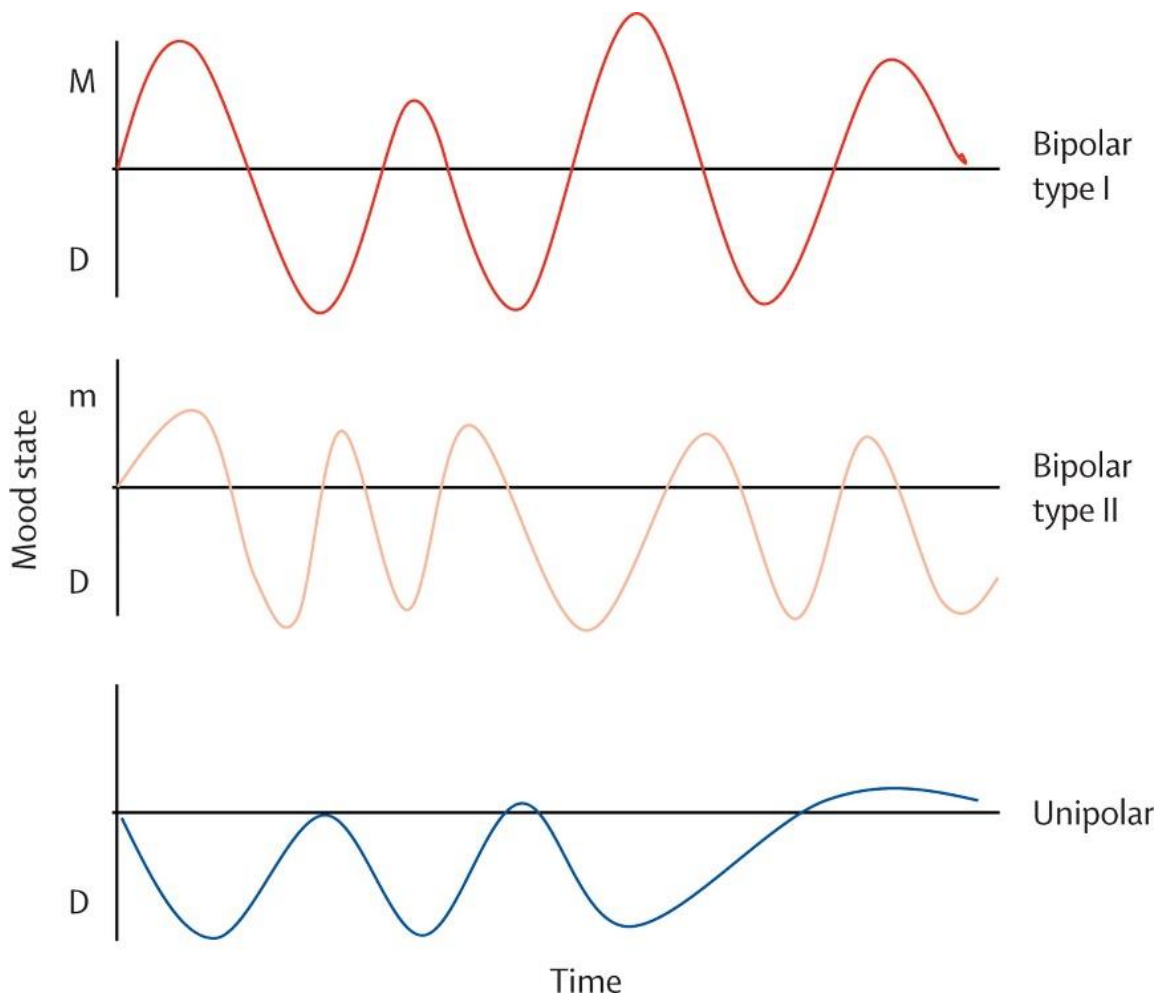


Figure 1.2. Representative traces of mood states over time for bipolar disorder type I (top trace), type II (middle trace), and unipolar disorder (bottom trace). Mood fluctuations range from depressed (D) to hypomania (m) and mania (M). This graphic was reproduced with permission from Elsevier.³

recurring depressive episodes (Figure 1.2).³ Misdiagnoses are most prevalent in patients experiencing the onset of bipolar disorder, which is thought to be the result of depression-like symptoms at early stages with no apparent history of mania or hypomania.^{4,5}

Unlike bipolar disorder, autism spectrum disorder, or simply autism, is typically diagnosed during childhood, when the child displays a range of symptoms that reside in two impairment domains: (i) restricted interests and repetitive behaviors, and (ii) verbal and non-verbal

communication. Autism symptoms can range from mild to severe, and affected individuals exhibit intellectual capacities ranging from gifted to greatly disabled. The revised Autism Diagnostic Interview (ADI-R) and the Autism Diagnostic Observational Schedule (ADOS) are examples of standardized interview-based exams that function as the current diagnostic gold standard in behavioral research and clinical settings for both autism and bipolar disorder.^{6,7} Unfortunately, there are no diagnostically informative biological tests available which could serve as a basis for developing targeted pharmaceutical- or genetic-based disease interventions. Indeed, the lack of diagnostic alternatives illustrates the need for new analytical tools and a better fundamental understanding of brain function, particularly in regions that heavily rely on dopaminergic neurotransmission.

1.2 Optical Microscopy in Neuroscience and the Need for Single Molecule Imaging

Elements of this chapter are derived from Thal, L.B., Kovtun, O., and Rosenthal, S.J., Labeling Neuronal Proteins with Quantum Dots for Single Molecule Imaging, Methods in Molecular Biology, Copyright 2020, Springer Science+Business Media, LLC.

The structural and functional complexity of the human brain has defied explanation. Until the 20th century, cognition research was largely a philosophical endeavor. Combined with the first electrophysiological studies, the optical imaging of neurons, pioneered by Spanish neuroanatomist Santiago Ramón y Cajal, catapulted brain research from pure theory to empirical science. He modified the Golgi staining technique, now ubiquitously known as Cajal staining, to employ the use of silver to stain mammalian cells.^{8,9} Cajal then famously imaged neuronal morphology and

constructed the first map of a neuronal network, two landmark events that contributed immensely to the burgeoning field of neuroscience.⁸ Optical microscopy has since served as one of neuroscience's cardinal tools. Initially, scientists like Cajal would represent their microscopy data by pictography, simply drawing the structures observed at the eyepiece. The incorporation of cameras into microscopes afforded not only more representative data acquisition, but also a means to assign intensity values for each pixel. This technological advancement enabled computational approaches to neuroscience, making optical microscopy a quantitative technique. But with the advent analytical tools developed in recent decades, our knowledge of the brain structure-function relationship has only grown in complexity, leading to our present time as "a revolution in neurotechnology" (coined by Dr. John Donoghue as the 2018 Cell-Neurotechnology Symposium in Leuven, Belgium). This spring of neurotechnology originated from the need to overcome the limitations in characterizing the brain in full, but more importantly, the pressing need to understand the root causes of neuropsychiatric diseases and ultimately aid in development of diseases intervention.

Neuroscience has largely adopted optical imaging methods as one of its primary methods for investigating the properties of neuronal proteins (*e.g.* ion channels, G-protein coupled receptors, and transporters). Specifically, fluorescence microscopy has been used to investigate intrinsic properties such as conformational changes, spatial distribution, and clustering propensity, as well as extrinsic properties such as heteromer complex formation, intracellular signaling capacity, and membrane potential.¹⁰⁻¹⁵ Consequent to the dynamic nature of neuronal proteins, sensitive analytical techniques must be employed to observe their dynamics at plasma membranes. In the 1970s, scientists measured the membrane diffusion dynamics of a host of transmembrane proteins by first exhaustively photobleaching stained subregions then monitoring the replenished

fluorescence of protein-bound fluorophores laterally diffusing from the surrounding areas.^{16, 17} While this widely adopted technique, now known as fluorescence recovery after photobleaching (FRAP), affords ensemble information about cell surface protein diffusion dynamics, it does not provide information about protein membrane subdomains important to cellular function.

With advances in microscope optics and camera sensitivity, resolution below the diffraction limit of visible light is now achievable allowing the detection of single proteins in live cells. This yields spatiotemporal information of the protein that would not otherwise be apparent using conventional imaging approaches. Several techniques have been developed to achieve the spatial resolution needed to detect single emitters. One of these novel techniques is photoactivated localization microscopy, or PALM developed by Eric Betzig, which uses stochastically illuminated fluorophore subsets to construct superresolved maps. Betzig was awarded the 2014 Nobel Prize in Chemistry for this novel technique.¹⁸ One of the most powerful sub-diffraction single emitter imaging strategies, single particle tracking (SPT), employs very bright fluorophores, which enables the direct real-time monitoring of a single fluorophore.¹⁹

Several lines of evidence, particularly those from SPT analysis, demonstrate that the lateral surface mobility of proteins is implicated in biological function.²⁰⁻²⁷ SPT combined with electrophysiology measurements demonstrated a majority of neurotransmitter receptors undergo diffusion exchange between extrasynaptic and synaptic regions, a mechanism that shapes synaptic strength.^{20, 21} This receptor flux can be modulated by interactions with scaffolding elements resident to synaptic terminals such that when housed at the synapse, the receptor mobility is confined until a stimuli-dependent disruption of the scaffold-receptor interaction occurs. For example, α -amino-3-hydroxy-5-methyl-4-isoxazolepropionic acid receptors (AMPA receptors) engage in this synaptic interaction with postsynaptic density protein 95 (PSD-95) and stargazin,²²

metabotropic glutamate receptors (mGluRs) interact with homer,²³ and glycine receptors (GlyRs) interact with gephyrin or the cytoskeleton at the synapse.²⁴⁻²⁶ Intriguingly, a rigorous set of experiments showed that the autoantibodies of neuropsychiatric patients, particularly those experiencing psychosis, altered the diffusion dynamics of N-methyl-D-aspartate receptors (NMDARs), inducing synaptic disorganization and ultimately reinforcing the clinically relevant role of surface trafficking.²⁷

1.3 Quantum Dots as Probes for Single Molecule Imaging

Elements of this chapter are derived from Thal, L.B., Kovtun, O., and Rosenthal, S.J., Labeling Neuronal Proteins with Quantum Dots for Single Molecule Imaging, Methods in Molecular Biology, Copyright 2020, Springer Science+Business Media, LLC.

Along with advances in microscopy instrumentation, considerable effort toward the development of molecular probe design has further refined single molecule imaging capabilities. At the forefront of these advances are bright, photostable fluorescent probes called quantum dots (QDs).²⁸⁻³¹ QDs are fluorescent semiconductor nanocrystals typically synthesized with a core/shell composition (e.g. CdSe/CdS) with diameters ranging from 4 to 10 nm.³² As a result of quantum confinement, QDs have size-tunable and narrow Gaussian emission spectra, which allow for feasible selection of orthogonal fluorophores in multi-color imaging experiments. Unlike the limited photon counts exhibited by conventional fluorophores, their large absorption cross-sections and high quantum yields also make QDs extraordinarily bright, a property that contributes to signal-to-noise ratios (SNR) suitable for SPT experiments.³³ QDs also exhibit excellent

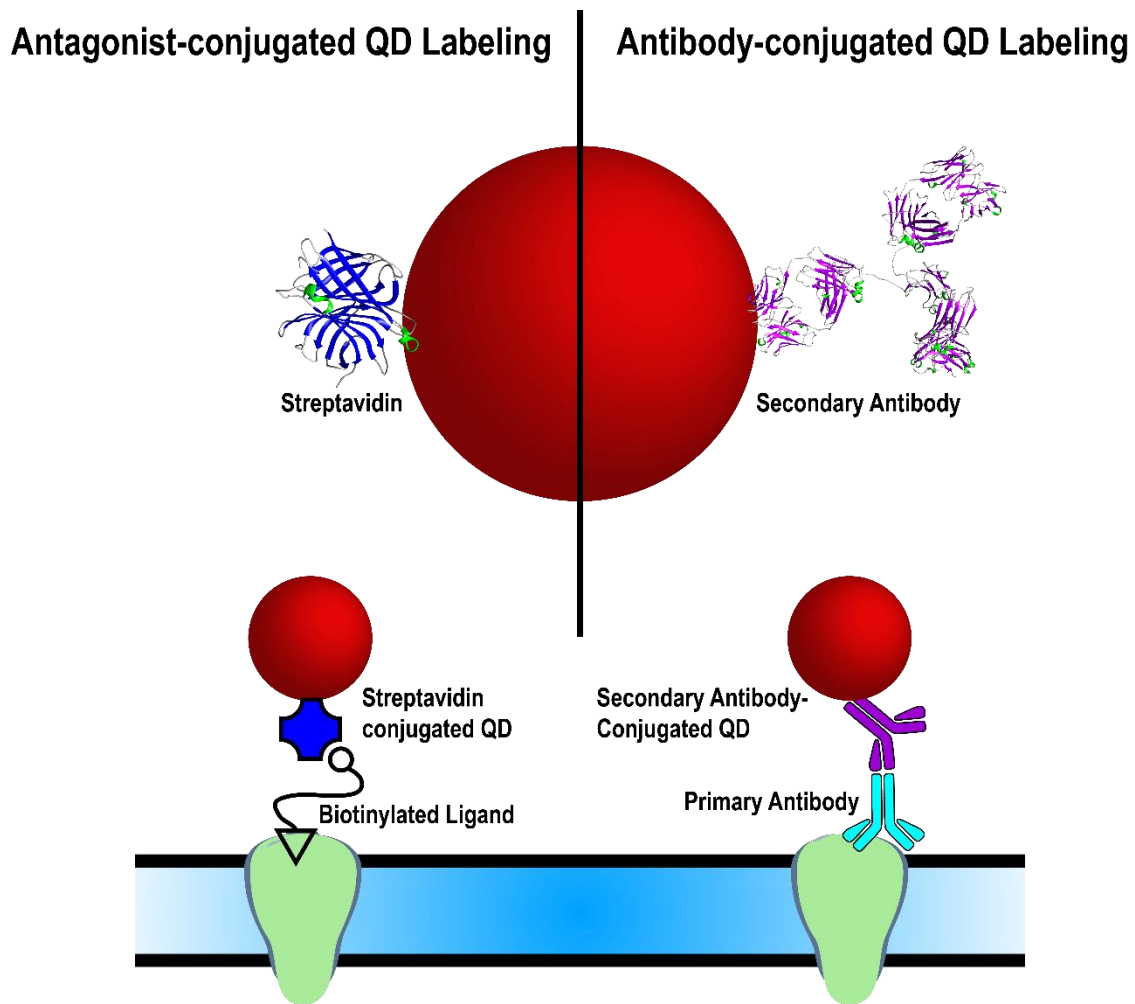


Figure 1.3. Two established approaches for QD labeling of neuronal proteins. Left: streptavidin-conjugated QDs target membrane proteins (green) employing a biotinylated ligand specific for target of interest. Right: secondary antibody-conjugated QDs target membrane proteins pretreated with a specific primary antibody.

photostability, which allows for single particle trajectory collection on the order of minutes.³⁴ Demonstrating such a robust profile of photophysical properties, QDs have played a critical role in the implementation of single protein imaging experiments, particularly in the field of chemical neuroscience, where the imaging of neuronal proteins, such as dopamine D2 receptors (D2R), gamma amino butyric acid (GABA)-gated receptors, dopamine transporters (DAT), and serotonin transporters (SERT), elucidated the membrane trafficking mechanisms in signaling and transport

regulation.³⁴⁻⁴²

Specific target recognition is perhaps the most critical property to consider when building a QD probe. To facilitate specificity, a variety of conjugation approaches have been designed. The most popular option is one in which QDs are conjugated to secondary antibodies, in full or the fragment structure, containing epitopes specific to primary antibodies bound to their biomolecular target (Figure 1.3). An alternative approach involves biotinylating the primary antibody to enable high-affinity labeling using streptavidin-conjugated QDs. In 2002, the Rosenthal group conjugated a small-molecule ligand to successfully target and image SERT proteins in transfected cells.⁴³ With the installment of a biotin handle in conjunction with a small alkyl spacer which promotes flexibility and hydrophobicity for drug-binding site interaction, and a polyethylene glycol (PEG) spacer for aqueous solubility and mitigation of non-specific binding, the neuroactive ligand (antagonist or agonist) can both bind to its target and QD-bound streptavidin.²⁸

By combining ligand-conjugated QD probe architecture with SPT analysis, the Rosenthal research group discovered that in immortalized serotonergic rat embryo cells (RN46A), receptor-linked signaling known to enhance transporter activity also increases the mobile population of SERT proteins that would otherwise be confined by cholesterol-enriched microdomains.⁴¹ In dissociated rat midbrain neurons, a similar shift in mobile SERT population was found to be dependent on the phosphorylation status of the Thr276 site of SERT. These results were consistent with an increase in mobility for the autism-linked SERT Gly56Ala coding variant, which harbors a hyperphosphorylation phenotype.²⁸

DAT, the dopaminergic sister protein of SERT, establishes functional neurotransmission by clearing the synapse of dopamine. Importantly, DAT is known to have two primary modes of

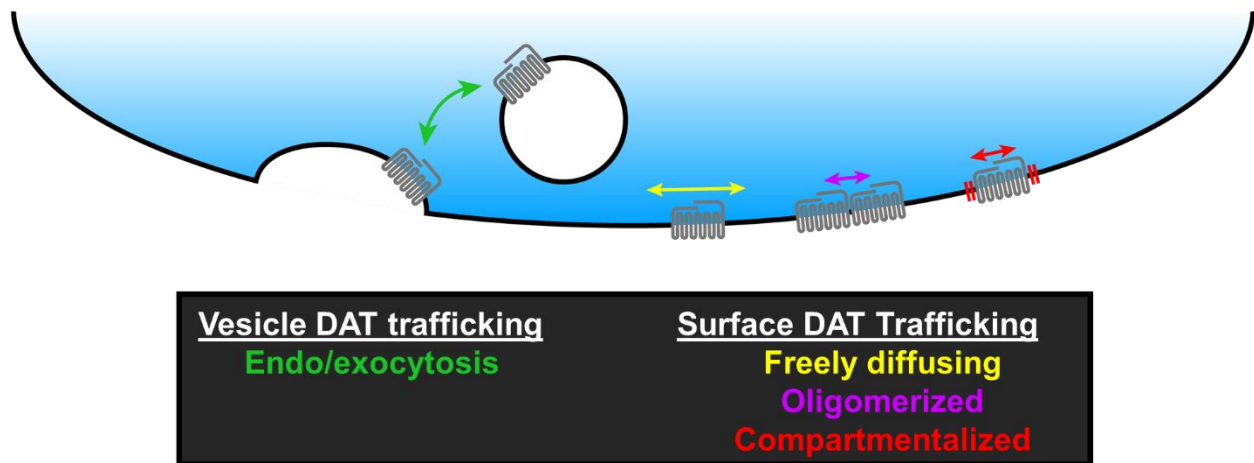


Figure 1.4. DAT regulation separated into two trafficking modes. This cartoon depicts the presynaptic terminal reduced to DAT trafficking examples. Vesicle trafficking is characterized by endo/exocytosis. Surface trafficking is characterized by various membrane statuses: freely diffusing, oligomerized, and compartmentalized.

regulation: (i) the heavily studied vesicle trafficking in which endocytosis and exocytosis work in concert to simply regulate the availability of DAT and (ii) the lesser studied, more elaborate surface trafficking (as mentioned at the end of Section 1.2) in which DAT can exist in freely diffusing, oligomerized, or compartmentalized states (Figure 1.4). Aiming to understand the DAT surface trafficking, the Rosenthal laboratory successfully labeled DAT with a cocaine analog ligand (IDT444) conjugation approach and spent considerable effort interrogating DAT membrane mobility in transfected cell culture.^{38-40,44} A large host of DAT coding variants have been identified in neuropsychiatric patients (Figure 1.5). Remarkably, the Rosenthal group also showed that the rare DAT Cys615 coding variant found in individuals diagnosed with attention-deficit/hyperactive disorder (ADHD) exhibited faster membrane mobility and larger area explored than the wild-type.³⁹ The enhanced mobility of the DAT mutant resembled DAT mobilities upon methyl- β -cyclodextrin (M β CD)-mediated cholesterol depletion and amphetamine treatment.³⁹ Using

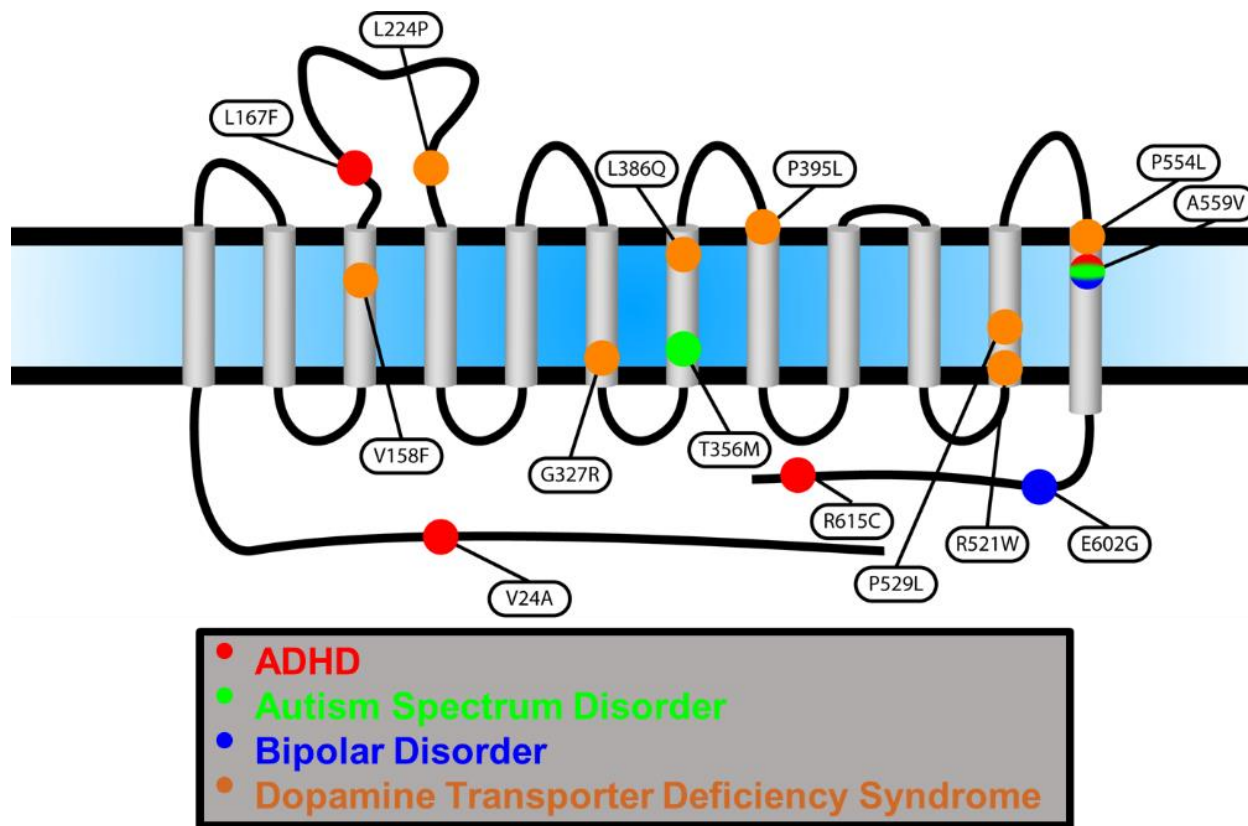


Figure 1.5. Sequence locations of DAT mutations associated to neurological diseases: ADHD, autism spectrum disorder, bipolar disorder, and dopamine transporter deficiency syndrome.

IDT444-conjugated QDs, this study unveiled the first direct single-particle observation of DAT in response to a neuropsychiatric disease-associated mutation, and membrane destabilization, as well as a pharmacologically relevant psychostimulant.³⁹

1.4 Dissertation Outline

This dissertation focuses on using single-particle data as the primary analytical source to address questions both in biological and chemical settings. I begin with providing detail on

experimental methods used in my research. This chapter is broken up into sections so the reader can easily refer to specific experiments highlighted in subsequent chapters. In Chapter 3, I then discuss how single QD imaging revealed abnormal membrane diffusion of an ADHD/autism/bipolar disorder-derived DAT variant (DAT Val559, Figure 1.5). I further provide evidence that alterations in surface trafficking operates in a protein kinase C (PKC)- β pathway-dependent manner.

While these studies in heterologous cells build a pharmacological and biophysical profile of DAT, they remain quite removed from the *in vivo* regime. In the interest of transitioning to a more physiologically relevant environment, I discuss advances made in imaging QDs deep in living brain tissue in Chapter 4. This chapter also provides a blueprint of probe characterization useful to those designing probes in chemically and physically challenging environments. I discuss how both shell thickness and *geometry* are important properties for QDs in neurophysiological environments. This chapter also includes single particle imaging of symmetrically shelled QDs that enable SPT deep in acute striatal brain slices. Chapter 5 completes my dissertation with concluding remarks and future directions.

1.5 References

1. U.S. Department of Health and Human Services, National Institutes of Health, National Institute of Mental Health. (2015).
2. Whiteford, H. A., Degenhardt, L., Rehm, J., Baxter, A. J., Ferrari, A. J., Erskine, H. E., Charlson, F. J., Norman, R. E., Flaxman, A. D., Johns, N., Burstein, R., Murray, C. J. L., and Vos, T., Global burden of disease attributable to mental and substance use disorders: findings from the Global Burden of Disease Study 2010, *The Lancet*, **2013**, 382, 1575-1586.
3. Phillips, M. L. and Kupfer, D. J., Bipolar disorder diagnosis: challenges and future directions. *The Lancet*, **2013**, 381, 1663-1671.

4. Goodwin, F. K. and Jamison, K. R., *Manic-depressive illness: bipolar disorders and recurrent depression*. Oxford University Press: 2007; Vol. 1.
5. Hirschfeld, R. M. A., Lewis, L., and Vornik, L. A., Perceptions and impact of bipolar disorder: How far have we really come? Results of the National Depressive and Manic-Depressive Association 2000 survey of individuals with bipolar disorder, *J. Clin. Psychiatry*, **2003**, *64*, 161-174.
6. Lord, C., Rutter, M., and Le Couteur, A., Autism Diagnostic Interview-Revised: a revised version of a diagnostic interview for caregivers of individuals with possible pervasive developmental disorders, *J Autism Dev Disord*, **1994**, *24*, 659-85.
7. Reaven, J. A., Hepburn, S. L., and Ross, R. G., Use of the ADOS and ADI-R in Children with Psychosis: Importance of Clinical Judgment, *Clin. Child Psychol. Psychiatry*, **2008**, *13* (1), 81-94.
8. De Carlos, J. A. and Borrell, J., A historical reflection of the contributions of Cajal and Golgi to the foundations of neuroscience, *Brain Res. Rev.*, **2007**, *55*, 8-16.
9. y Cajal, S. R., *Recuerdos de mi vida*. Librería de Nicolás Moya: 1917.
10. Harms, G. S., Cognet, L., Lommerse, P. H. M., Blab, G. A., Kahr, H., Gamsjäger, R., Spaink, H. P., Soldatov, N. M., Romanin, C., and Schmidt, T., Single-Molecule Imaging of L-Type Ca²⁺ Channels in Live Cells, *Biophys. J.*, **2001**, *81* (5), 2639-2646.
11. Marcott, P. F., Gong, S., Donthamsetti, P., Grinnell, S. G., Nelson, M. N., Newman, A. H., Birnbaumer, L., Martemyanov, K. A., Javitch, J. A., and Ford, C. P., Regional Heterogeneity of D2-Receptor Signaling in the Dorsal Striatum and Nucleus Accumbens, *Neuron*, **2018**, *98* (3), 575-587.e4.
12. Weiss, S., Measuring conformational dynamics of biomolecules by single molecule fluorescence spectroscopy, *Nat. Struct. Biol.*, **2000**, *7*, 724.
13. Vilardaga, J.P., Nikolaev, V. O., Lorenz, K., Ferrandon, S., Zhuang, Z., and Lohse, M. J., Conformational cross-talk between α_2A -adrenergic and μ -opioid receptors controls cell signaling, *Nat. Chem. Biol.*, **2008**, *4*, 126.
14. Grenier, V., Walker, A. S., and Miller, E. W., A Small-Molecule Photoactivatable Optical Sensor of Transmembrane Potential, *J. Am. Chem. Soc.*, **2015**, *137*, 10894-10897.
15. Mason, J. N., Farmer, H., Tomlinson, I. D., Schwartz, J. W., Savchenko, V., DeFelice, L. J., Rosenthal, S. J., and Blakely, R. D., Novel fluorescence-based approaches for the study of biogenic amine transporter localization, activity, and regulation, *J. Neurosci. Methods*, **2005**, *143*, 3-25.
16. Axelrod, D., Koppel, D. E., Schlessinger, J., Elson, E., and Webb, W. W., Mobility measurement by analysis of fluorescence photobleaching recovery kinetics, *Biophys. J.*, **1976**, *16*,

1055-1069.

17. Axelrod, D., Ravdin, P., Koppel, D. E., Schlessinger, J., Webb, W. W., Elson, E. L., and Podleski, T. R., Lateral motion of fluorescently labeled acetylcholine receptors in membranes of developing muscle fibers, *Proceedings of the National Academy of Sciences*, **1976**, 73, 4594-4598.

18. Betzig, E., Patterson, G. H., Sougrat, R., Lindwasser, O. W., Olenych, S., Bonifacino, J. S., Davidson, M. W., Lippincott-Schwartz, J., and Hess, H. F., Imaging Intracellular Fluorescent Proteins at Nanometer Resolution, *Science*, **2006**, 313, 1642-1645.

19. Dahan, M., Lévi, S., Luccardini, C., Rostaing, P., Riveau, B., and Triller, A., Diffusion Dynamics of Glycine Receptors Revealed by Single-Quantum Dot Tracking, *Science* **2003**, 302, 442-445.

20. Triller, A. and Choquet, D., Surface trafficking of receptors between synaptic and extrasynaptic membranes: and yet they do move!, *Trends Neurosci.*, **2005**, 28, 133-139.

21. Choquet, D. and Triller, A., The role of receptor diffusion in the organization of the postsynaptic membrane, *Nat. Rev. Neurosci.*, **2003**, 4, 251.

22. Bats, C., Groc, L., and Choquet, D., The Interaction between Stargazin and PSD-95 Regulates AMPA Receptor Surface Trafficking, *Neuron*, **2007**, 53, 719-734.

23. Sergé, A., Fourgeaud, L., Hémar, A., and Choquet, D., Receptor Activation and Homer Differentially Control the Lateral Mobility of Metabotropic Glutamate Receptor 5 in the Neuronal Membrane, *J. Neurosci.*, **2002**, 22, 3910-3920.

24. Meier, J., Vannier, C., Sergé, A., Triller, A., and Choquet, D., Fast and reversible trapping of surface glycine receptors by gephyrin, *Nat. Neurosci.*, **2001**, 4, 253-260.

25. Ehrensperger, M.V., Hanus, C., Vannier, C., Triller, A., and Dahan, M., Multiple Association States between Glycine Receptors and Gephyrin Identified by SPT Analysis, *Biophys. J.*, **2007**, 92, 3706-3718.

26. Charrier, C., Ehrensperger, M.V., Dahan, M., Lévi, S., and Triller, A., Cytoskeleton Regulation of Glycine Receptor Number at Synapses and Diffusion in the Plasma Membrane, *J. Neurosci.*, **2006**, 26, 8502-8511.

27. Jézéquel, J., Johansson, E. M., Dupuis, J. P., Rogemond, V., Gréa, H., Kellermayer, B., Hamdani, N., Le Guen, E., Rabu, C., and Lepleux, M., Dynamic disorganization of synaptic NMDA receptors triggered by autoantibodies from psychotic patients, *Nat. Commun.*, **2017**, 8, 1791.

28. Kovtun, O., Tomlinson, I. D., Bailey, D. M., Thal, L. B., Ross, E. J., Harris, L., Frankland, M. P., Ferguson, R. S., Glaser, Z., Greer, J.; and Rosenthal, S. J., Single quantum dot tracking illuminates neuroscience at the nanoscale, *Chem. Phys. Lett.*, **2018**, 706, 741-752.

29. Thal, L. B., Bailey, D. M., Kovtun, O., and Rosenthal, S. J., Quantum Dot Toolbox in Membrane Neurotransmitter Transporter Research. In *Chemical and Synthetic Approaches in Membrane Biology*, Shukla, A. K., Ed. Springer New York: New York, NY, 2017; pp 219-230.
30. Rosenthal, S. J. and Wright, D. W., *Nanobiotechnology protocols*, Springer: 2005; Vol. 1.
31. Chang, J. C. and Rosenthal, S. J., Single Quantum Dot Imaging in Living Cells. In *Cellular and Subcellular Nanotechnology: Methods and Protocols*, Weissig, V.; Elbayoumi, T.; Olsen, M., Eds. Humana Press: Totowa, NJ, 2013; pp 149-162.
32. McBride, J., Treadway, J., Feldman, L. C., Pennycook, S. J., and Rosenthal, S. J., Structural Basis for Near Unity Quantum Yield Core/Shell Nanostructures, *Nano Lett.*, **2006**, 6, 1496-1501.
33. Rosenthal, S. J., Chang, J. C., Kovtun, O., McBride, J. R., and Tomlinson, I. D., Biocompatible Quantum Dots for Biological Applications, *Chem. Biol.*, **2011**, 18, 10-24.
34. Yanagawa, M., Hiroshima, M., Togashi, Y., Abe, M., Yamashita, T., Shichida, Y., Murata, M., Ueda, M., and Sako, Y., Single-molecule diffusion-based estimation of ligand effects on G protein-coupled receptors, *Sci. Signal.*, **2018**, 11, eaa01917.
35. Gussin, H. A., Tomlinson, I. D., Muni, N. J., Little, D. M., Qian, H., Rosenthal, S. J., and Pepperberg, D. R., GABA_C Receptor Binding of Quantum-Dot Conjugates of Variable Ligand Valency, *Bioconjugate Chem.*, **2010**, 21, 1455-1464.
36. Gussin, H. A., Tomlinson, I. D., Little, D. M., Warnement, M. R., Qian, H., Rosenthal, S. J., and Pepperberg, D. R., Binding of Muscimol-Conjugated Quantum Dots to GABA_C Receptors, *J. Am. Chem. Soc.*, **2006**, 128, 15701-15713.
37. Gussin, H. A., Tomlinson, I. D., Cao, D., Qian, H., Rosenthal, S. J., and Pepperberg, D. R., Quantum Dot Conjugates of GABA and Muscimol: Binding to $\alpha_1\beta_2\gamma_2$ and ρ_1 GABA_A Receptors, *ACS Chem. Neurosci.*, **2013**, 4, 435-443.
38. Kovtun, O., Tomlinson, I. D., Sakrikar, D. S., Chang, J. C., Blakely, R. D., and Rosenthal, S. J., Visualization of the Cocaine-Sensitive Dopamine Transporter with Ligand-Conjugated Quantum Dots, *ACS Chem. Neurosci.*, **2011**, 2, 370-378.
39. Kovtun, O., Sakrikar, D., Tomlinson, I. D., Chang, J. C., Arzeta-Ferrer, X., Blakely, R. D., and Rosenthal, S. J., Single-Quantum-Dot Tracking Reveals Altered Membrane Dynamics of an Attention-Deficit/Hyperactivity-Disorder-Derived Dopamine Transporter Coding Variant, *ACS Chem. Neurosci.*, **2015**, 6, 526-534.
40. Thal, L. B., Tomlinson, I. D., Quinlan, M. A., Kovtun, O., Blakely, R. D., and Rosenthal, S. J., Single Quantum Dot Imaging Reveals PKC β -Dependent Alterations in Membrane Diffusion and Clustering of an Attention-Deficit Hyperactivity Disorder/Autism/Bipolar Disorder-Associated Dopamine Transporter Variant, *ACS Chem. Neurosci.*, **2019**, 10, 460-471.

41. Chang, J. C., Tomlinson, I. D., Warnement, M. R., Ustione, A., Carneiro, A. M. D., Piston, D. W., Blakely, R. D., and Rosenthal, S. J., Single Molecule Analysis of Serotonin Transporter Regulation Using Antagonist-Conjugated Quantum Dots Reveals Restricted, p38 MAPK-Dependent Mobilization Underlying Uptake Activation, *J. Neurosci.*, **2012**, 32, 8919-8929.
42. Bailey, D. M., Catron, M. A., Kovtun, O., Macdonald, R. L., Zhang, Q., and Rosenthal, S. J., Single Quantum Dot Tracking Reveals Serotonin Transporter Diffusion Dynamics are Correlated with Cholesterol-Sensitive Threonine 276 Phosphorylation Status in Primary Midbrain Neurons, *ACS Chem. Neurosci.*, **2018**, 9, 2534-2541.
43. Rosenthal, S. J., Tomlinson, I., Adkins, E. M., Schroeter, S., Adams, S., Swafford, L., McBride, J., Wang, Y., DeFelice, L. J., and Blakely, R. D., Targeting Cell Surface Receptors with Ligand-Conjugated Nanocrystals, *J. Am. Chem. Soc.*, **2002**, 124, 4586-4594.
44. Kovtun, O., Tomlinson, I. D., Ferguson, R. S., and Rosenthal, S. J., Quantum dots reveal heterogeneous membrane diffusivity and dynamic surface density polarization of dopamine transporter, *PLOS ONE*, **2019**, 14, e0225339.

CHAPTER II

EXPERIMENTAL METHODS

Elements of this section were reprinted with permission from:

1. Thal, L. B., Tomlinson, I. D., Quinlan, M. A., Kovtun, O., Blakely, R. D., and Rosenthal, S. J., *Single Quantum Dot Imaging Reveals PKC β -Dependent Alterations in Membrane Diffusion and Clustering of an Attention-Deficit Hyperactivity Disorder/Autism/Bipolar Disorder-Associated Dopamine Transporter Variant*, *ACS Chem. Neurosci.*, **2019**, 10, 460-471. Copyright 2019. American Chemical Society.
2. Thal, L.B., Mann, V.R., Sprinzen, D., McBride, J.R., Reid, K.R., Tomlinson, I.D., McMahon, D.G., Cohen, B.E., and Rosenthal S.J., *Ligand-conjugated quantum dots for fast sub-diffraction protein tracking in acute brain slices*, *Biomater Sci.* **2020**, 8, 837-845, Copyright 2020. Royal Chemical Society.

2.1 Mammalian Cell Culture and Tissue Preparation

HEK-293 cells were a kind gift from Eva Harth, Ph.D. at Vanderbilt University, and SK-N-MC cells were kindly provided by Jerry Chang, Ph.D. at the Rockefeller University Laboratory of Molecular and Cellular Neuroscience. Mice were kindly provided by Dr. Douglas McMahon in the BRAIN Institute at Vanderbilt University.

2.1.1 HEK-293 and SK-N-MC Cells

HEK-293 cells were maintained using a complete growth medium comprised of DMEM with 2 mM L-glutamine, 10% fetal bovine serum (FBS), and 1% penicillin/streptomycin, incubated at 37°C at a 5% atmospheric CO₂. SK-N-MC cells were grown using a complete growth medium comprised of EMEM with 2 mM L-glutamine, 10% fetal bovine serum (FBS), and 1% penicillin/streptomycin, incubated at 37°C at a 5% atmospheric CO₂. Cells were then seeded in poly-D-lysine coated (1 hr at 37 °C) MatTek dishes at a cell density that produced a subconfluent monolayer.

2.1.2 Transfection of DAT Coding Variants

pcDNA3.1(+) DAT and pcDNA3.1(+) DAT Val559 constructs were previously detailed.¹ yfpsyndat (Addgene plasmid # 19991) and YFP-synDAT-S/D (Addgene plasmid # 48793) were gifts from Jonathan Javitch, Ph.D. at Columbia University. Q5 site directed mutagenesis (NEB Inc.) was used to generate hDAT A53 and D53 on both the hDAT and hDAT A559V plasmid with forward primer RB5576 5'-CCCGCGGCAGgccCCCGTGGAGG-3' and RB5578 5'-CCCGCGGCAGgacCCCGTGGAGG-3', respectively, and reverse primer RB5577 5'-TTGGTGAGGGTGGAGCTGG-3'. Both HEK-293 and SK-N-MC cell cultures were transiently transfected 24 h prior to labeling at 1 µg DNA:3 µL Lipofectamine 3000 ratio. Typically, this involved adding a lipofectamine/DNA mixture that contained 500 ng DNA per dish.

2.1.3 Acute Mouse Brain Slice Preparation

Brains were dissected and blocked in cold, oxygenated 95% O₂ artificial cerebrospinal fluid (aCSF) solution (in mM: 114.5 NaCl, 3.5 KCl, 1 NaH₂PO₄, 1.3 MgSO₄, 2.5 CaCl₂, 10 D-glucose

and 35.7 NaCHO₃). Striatal slices (300 μm) were cut with a Leica vibrotome at 4–10 °C and transferred directly to a continually oxygenated chamber with cold aCSF.

2.3 Single Quantum Dot Labeling and Fluorescence Microscopy of Biological Samples

2.3.1 Transiently Transfected DAT-expressing Cell Culture

DAT-expressing HEK-293 and SK-N-MC cells were plated on MatTek No. 1.5 coverslips coated with poly-D-lysine and laminin, respectively. QD labeling was employed following a two-step protocol previously outlined.² Briefly, cells in 2 mL of full growth medium were spiked with 20 μL of 10 μM IDT444 suspended in phosphate buffer saline (PBS) (w/o Ca²⁺, Mg²⁺) and incubated at 37 °C and 5% CO₂ for 10 min. Three washes with warm DMEM Fluorobrite were performed prior to treating cells with 10 pM SavQD 2% dialyzed FBS in DMEM Fluorobrite. The QD-IDT444 DAT-labeled cells were washed three times with warm DMEM Fluorobrite. Activation of PKC and inhibition of PKCβ were performed by administering 100 nM Phorbol-12-myristate-13-acetate (PMA) 30 min prior to washing and 1 μM Enzastaurin (Enz) prior to PMA treatment, respectively. PMA- and Enz-treated cells were washed an additional 3 times with warm DMEM Fluorobrite. At the microscope, IDT307 was added to the MatTek dish prior to imaging.

Time-series images were generated by total internal reflection fluorescence (TIRF) and widefield epifluorescence microscopy on a Nikon Eclipse Ti-E inverted microscope equipped with an Andor Zyla 4.2 PLUS scientific complementary metal oxide semiconductor (sCMOS) camera and viewed with an Apo TIRF 60×/1.49 NA oil objective. Excitation at 488 nm was sourced by a

Nikon LU-NV laser unit. Yellow fluorescent protein-fused DAT (YFP-DAT) and IDT307 emissions were collected with a 525 ± 18 nm emission filter. Streptavidin-conjugated QD (SavQD-605 and SavQD-655) signals were collected with 603 ± 15 nm and 655 ± 15 nm emission filters, respectively. For SPT experiments, time series were produced at a 10 Hz frame rate. For clustering experiments, time series were produced at a 17 Hz frame rate.

2.3.2 Acute Striatal Brain Slices

Slices were incubated with a mixture of 1X CellMask deep red stain and 50 nM QD-IDT725 for 10 minutes prior to three washes with cold aCSF. QDs in the striatum were visualized using a Nikon Eclipse Ti-E inverted microscope equipped with a Yokogawa CSU-X1 spinning disk head and an Andor DU-897 electron multiplying charge coupled device (EMCCD). QDs and the CellMask stain were excited with a 405 nm and 488 nm excitation sources, respectively. Emissions were collected with a 640 ± 75 nm and 700 ± 37 nm emission filters, respectively. In-house MATLAB routines were used for automated analysis of all imaging data. Labeling and tracking protocols were previously detailed.⁷

2.4 Data Analysis

2.4.1 Single Quantum-dot Trajectory Generation

Raw TIFF stacks were extracted from Nikon Elements ndl files in Fiji, an ImageJ distribution (National Institutes of Health, Bethesda, MD). Trajectories were compiled from these

raw data given the conditions that (i) the particle emission is intermittent to ensure discrimination of single particles, (ii) the blinking gap is less than 10 frames, (iii) the point spread function (PSF) is located within a 3×3 pixel area surrounding the PSF location from the previous frame, and (iv) the trajectory persists at least 50 frames.

2.4.2 Mean Square and 5 Second Displacement

Mean square displacement (MSD), $\langle r^2(n\delta t) \rangle$, values were calculated for each of the trajectories collected for time intervals of 0.1–1.5 s in 0.1 s intervals via

$$\langle r^2(n\delta t) \rangle = \frac{1}{N-n} \sum_{j=0}^{N-n-1} \{ [x(j\delta t + n\delta t) - x(j\delta t)]^2 + [y(j\delta t + n\delta t) - y(j\delta t)]^2 \}$$

$(n = 0, 1, 2, \dots, N - 1)$

where δt is the temporal resolution, $(x(j\delta t), y(j\delta t))$ is the coordinate at $t = j\delta t$, and N is the number of total frames recorded during a single trajectory. Diffusion coefficients (D_{1-3}) were determined from the linear fits of the first three MSD values in the algorithm

$$r^2(t)_{1-3} = 4D_{1-3}t + 4\sigma^2$$

where σ is the uncertainty of particle localization. The uncertainty, dependent on the SNR and limited by the diffraction limit using visible light, was estimated by $\Delta\sigma \approx \omega/SNR$, where ω is approximately the widefield mode diffraction limit and SNR values for QD emitters excited by an evanescent field in TIRF mode range between 20 and 30. D_{1-3} values were populated, and a significant difference between distributions was determined by one-way ANOVA followed by Bonferroni's multiple comparison test. 5 s displacement vectors were obtained by indexing particle coordinates after 50 frames and normalizing to the particle origin. Populated 5 s displacement

values were analyzed by unpaired Student's *t* test. All analysis was performed and automated by MATLAB codes. For extensive detail regarding microscopy and analysis in SPT experiments, see Chang and Rosenthal et al.³

2.4.3 Target Cluster Propensity

Raw TIFF stacks were extracted from Nikon Elements ndl files in Fiji. PSF centroids were subsequently identified and indexed. For the intensity of each PSF to be quantified, integrated density (ID) values were calculated by integrating raw intensity values in a 5×5 pixel matrix and normalized to the particle centroid coordinate. Because background in widefield mode is heterogeneous due to emission from QDs outside of the focal plane, background values were calculated by averaging intensity counts of a 9×9 pixel parameter centered around each centroid. Raw IDs were then corrected by their assigned backgrounds. All analysis was performed and automated by an in-house MATLAB script. The QuickPALM plugin in Fiji was used to generate tracking and localization microscopy (TALM) images.

2.5 Generation and Characterization of Quantum Dot Conjugates for Brain Slice Imaging

2.5.1 Synthesis of Symmetrically Shelled CdSe/CdS QDs

CdSe cores were synthesized as previously described.⁴⁻⁶ In an Ar glovebox, 0.058 g of Se powder (Aldrich, 99.99% trace metal basis) was added to 0.36 g of trioctylphosphine (TOP, Aldrich, 97%) in a glass vial and stirred overnight, yielding TOP-Se as a clear, colorless solution.

On a Schlenk line, 0.060 g of CdO (Aldrich, 99.99% trace metal basis, 0.47 mmol), 0.28 g of octadecylphosphonic acid (ODPA, 0.84 mmol), and 3.0 g of TOP oxide were combined in a 50-mL flask fitted with a condenser and temperature probe. The flask was heated under N₂ to 150 °C and stirred under vacuum for 1 hr. The flask was purged with N₂ and heated to 320 °C until the Cd complexed with the ODPA to become clear and colorless. TOP (1.50 g) was injected into the flask drop-wise and the temperature was then raised to 370 °C. The TOP-Se precursor was then rapidly injected, and allowed to react for 70 sec. The flask was cooled with air to below 110 °C, and 2 mL of dry ice-cooled toluene was injected. The final reaction solution was removed and the total volume of the solution was diluted with toluene to 15 mL. The particles were then precipitated with 15 mL of acetone and centrifuged at 4000 x g for 5 min. The pellet was dispersed in a minimum of CHCl₃, precipitated with 10 mL of acetone, centrifuged at 4000 x g for 5 min, dispersed in a minimum of hexane (~1 mL), and precipitated with acetone again. These cores were dispersed in 5 mL of hexane and stored in a glovebox.

Stock solutions of 0.1 M Cd oleate in 1-octadecene (ODE) and 0.1 M octanethiol in ODE were prepared in a glovebox. On a Schlenk line, 5 mL of ODE was placed in a 3-neck flask under N₂ and 100 nmol of CdSe core nanocrystals in hexane were injected. Solvent was removed under vacuum at room temperature and then at 120 °C for 20 min. The reaction was purged with N₂ and the glovebox solutions containing 7 mL of 0.1 M Cd oleate in ODE and 7 mL of 0.1 M octanethiol in ODE were injected at 310 °C via syringe pumps over 2.5 hr. After injection, 1 mL of oleic acid (OA) was quickly injected and the reaction was maintained at 310 °C for 1 hr. The reaction flask was cooled with air, the nanocrystals were cleaned by repeated precipitation as above, and the were nanocrystals dispersed in 10 mL of hexane with 1% OA (v/v) for storage under ambient conditions.

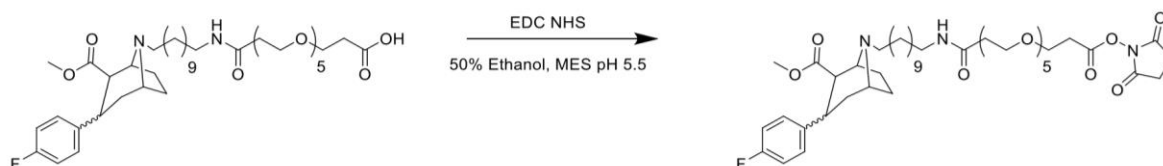
2.5.2 Passivation of Core-shell CdSe/CdS QDs by an Amphiphilic Copolymer

CdSe/CdS QDs with emission maxima of 640 nm were dispersed in hexane with 1% (v/v) OA to 3.75 μ M, as determined by first exciton absorbance. Poly(acrylic acid)-*co*-poly(*n*-octylacrylamide)-*co*-poly(2-aminoethylacrylamide) (PAOA, MW ~3000 Da) random copolymer was prepared as previously described.^{2,3} For aqueous dispersion, PAOA (24 mg, 7.5 μ mol, 10,000-fold molar excess over QDs) was dissolved in 1 mL of MeOH and 15 mL of CHCl₃. QDs in hexane (*e.g.*, 200 μ L of 3.75 μ M 640 nm CdSe/CdS QDs, 0.75 nmol) were added with stirring, and the solvents were removed under a gentle stream of N₂ overnight. The dried residue was then resuspended in 15 mL of 200 mM sodium bicarbonate buffer, pH 8.0. This suspension was sonicated for 30 min, heated in an 80 °C water bath for 60 min, slowly cooled in the bath to <30 °C, and then sonicated for 30 min. Excess polymer was removed by spin dialysis (Amicon Ultra-15, 50 kDa MWCO), washing with 3 \times 15 mL of 100 mM 4-(2-hydroxyethyl)-1-piperazineethanesulfonic acid (HEPES, pH 7.8). The retentate was diluted to 750 μ L with HEPES buffer and centrifuged at 16,100 \times *g* for 5 min to remove residual polymer and insoluble aggregates. Aqueous QD dispersions were stored under ambient conditions.

2.5.3 QD-Cy5 Conjugation and Amine/QD Quantification

10 μ L of 10 μ M Cy5-succinimidyl ester (Cy5-SE) in dimethyl sulfoxide (DMSO), 5 μ L of 2 μ M aqueous QDs, and 200 μ L of 100 mM HEPES pH 7.8 were mixed and incubated in a microfuge tube in the dark overnight. The next day, 30,000 MW spin filters were treated with polyvinyl pyrrolidone (PVP) for 15 min prior to washing excess Cy5-SE via spin dialysis filtering. Two additional washes were performed with 100 mM HEPES pH 7.8 followed by reconstituting

the QD-Cy5 conjugates to a final concentration of 20 nM. Absorbance spectra was acquired with a Cary UV-Vis spectrometer. An absorbance value at 650 nm was used to calculate Cy5 concentration by Beer-Lambert Law. Assuming a 1:1 stoichiometry for amines and Cy5 molecules, Amines/QD were obtained by normalizing the concentration of Cy5 to concentration of QDs.



2.5.4 IDT725SE Synthesis

Acid IDT725 (10 mg, 13.3 mmol) was dissolved in 500 μ L of ethanol and 500 μ L of 5 mM 2-(N-morpholino)ethanesulfonic acid (MES) buffer pH 5.5 in a 10-mL round bottom flask. N-(3-Dimethylaminopropyl)-N'-ethylcarbodiimide (EDC) (24.9 mg, 130 mmol) and N-hydroxysuccinimide (NHS) alcohol (14.9 mg, 130 mmol) were added, and the reaction stirred for 10 minutes. The product was purified at on a C18 HPLC column using a linear 40-60% CH_3CN gradient over 40 minutes, eluting at 34 minutes (53% CH_3CN) and unreacted free acid eluted at 27 minutes (49.5% CH_3CN) MS for $\text{C}_{44}\text{H}_{68}\text{FN}_3\text{O}_{12}$. (MH^+) calculated: 849.49; found: 850.96. See Appendix F for 2D nuclear magnetic resonance (NMR) spectra.

2.5.5 Surface Conjugation of Ligands

Polymer-encapsulated QDs (0.5 μM , 300 μL) in 0.1 M HEPES, pH 8.0, were mixed with 8.7 μL of 90% 1 mg/mL IDT725SE and 10% methoxy-PEG8-SE dissolved in EtOH, and vortexed well. After incubating overnight, the volume was increased to 500 μL with 0.1 M HEPES, pH 8.0,

and excess SE reagents were removed via spin dialysis (Amicon Ultra, 30 kDa MWCO) by washing 12 additional times with HEPES.

2.5.6 Dynamic Light Scattering

Diameters were measured using a Malvern Zetasizer. Aqueous QDs were diluted to ~20 nM with distilled water and filtered through a 0.2- μ m cut-off PVDF filter (Pall) before analysis. Typical count rates were 200 kilocounts per second. Data were collected for 150 seconds in triplicate and fit using Malvern Zetasizer software to a volume-weighted size distribution of hydrodynamic diameter.

2.5.7 Electron Microscopy and Energy-dispersive X-ray Spectroscopy

High-resolution transmission electron microscopy (HRTEM) and energy-dispersive X-ray spectroscopy (STEM-EDS) were performed on a Tecnai Osiris TEM/STEM operating at 200 kV equipped with a SuperX™ quad EDS detection system. Samples were prepared by drop casting or dip-coating dilute dispersions of the QDs onto ultrathin on lacey carbon support film (TED Pella 1824) and baked at 145 °C overnight under high vacuum prior to imaging. STEM-EDS maps were collected using Bruker Esprit software with a sub-nm probe having ~ 0.8 nA of beam current.

2.5.8 Ensemble Spectroscopy

Absorption spectra were collected using a Cary 60 UV-VIS spectrometer.

Photoluminescence (PL) spectra were collected using a PTI QuantaMaster fluorescence spectrophotometer equipped with a 75 W Xe arc lamp as the excitation source. PL was acquired in 1 s integration time intervals with a 1 nm slit width.

2.5.9 Time-Resolved Photoluminescence

Time-resolved photoluminescence (TRPL) measurements were performed on dilute solutions of QDs with optical densities below 0.2 at the lowest-energy absorption transition.^{7,8} The QD solutions were excited under widefield illumination using a 405 nm pulsed source at a 1 MHz repetition rate. PL from the solutions was filtered with an appropriate long-pass filter and directed onto a single-photon avalanche photo-diode (SPAD, Micro Photon Devices, PD-050-0TC). A time-correlated single photon-counting unit (TCSPC, PicoHarp 300) was used to generate a histogram of photon arrival times. Ensemble lifetimes were determined by fitting the histogram of arrival times to a tri-exponential function.

2.5.10 Single QD Fluorescence Analysis

QDs were first diluted to a 100 pM concentration and drop cast on an untreated no. 1.5 MatTek dish. The coverslip was incubated at room temperature for 3 minutes prior to aspiration. The dried coverslips were subsequently treated with either 100 mM HEPES pH 7.8 buffer or oxygenated aCSF. Intensity traces were acquired with a Nikon Eclipse Ti-E inverted microscope equipped with a Yokogawa CSU-X1 spinning-disk head, 1.4 NA 60× oil objective, Andor DU-897 EMCCD.⁶ QDs were excited using a dedicated 405 nm laser at 51 W/cm² with emission

collected with a 640 ± 75 nm emission filter. Blinking and photobleaching traces were acquired in 100 ms and 1 s time intervals, respectively. In-house MATLAB routines were used for automated analysis of all imaging data.

2.5.11 Surface-enhanced Raman Spectroscopy of QD Conjugates

15 μ L of 1 μ M QD samples were deposited on Ag surface-enhanced Raman spectroscopy (SERS) substrates immediately prior to Raman spectra collection. Raman spectra of SERS substrates were acquired by a Thermo Scientific DXR Raman microscope with a 532nm laser excitation source. 5 x 5 μ m matrices were collected per sample with a 4 second integration time and 10 scans per spectra. The 25 spectra collected were subsequently averaged.

2.6 QD-based Approach to Survey Endocytosed DAT

Detection of QDs and cell membrane was performed by using a Nikon Ti-E microscope equipped with a Yokogawa CSU-X1 spinning disk head and a high-speed piezo [z] stage. The system included a live-cell incubation chamber kept at 37 °C and 5% CO₂. Images were collected with a Plan Apo Lambda 60x oil objective with a 1.40 NA. 512 x 512 pixel (166 x 166 μ m) stacks with voxel depths of 300 nm were acquired with an Andor DU-897 EMCCD camera. Gain for the EMCCD camera was set at 150. QDs and the CellMask membrane stain were excited at 100 ms exposure time by 405 nm and 488 nm diode lasers, respectively, with detection through 605 ± 70 nm and 700 ± 70 nm filters, respectively. Nikon Elements Advanced Research software was used for image analysis.

2.7 References

1. Hamilton, P. J., Campbell, N. G., Sharma, S., Erreger, K., F. Herborg Hansen, F., Saunders, C., Belovich, A. N., N. A. A. S. Consortium, Sahai, M. A., Cook, E. H., Gether, U., McHaourab, H. S., Matthies, H. J. G., Sutcliffe, J. S., and Galli, A., *De novo* mutation in the dopamine transporter gene associates dopamine dysfunction with autism spectrum disorder, *Mol. Psychiatry*, **2013**, 18, 1315.
2. Thal, L. B., Bailey, D. M., Kovtun, O., and Rosenthal, S. J., Quantum Dot Toolbox in Membrane Neurotransmitter Transporter Research. In *Chemical and Synthetic Approaches in Membrane Biology*, Shukla, A. K., Ed. Springer New York: New York, NY, 2017; pp 219-230.
3. Chang, J. C. and Rosenthal, S. J., Real-time quantum dot tracking of single proteins. In *Biomedical Nanotechnology: Methods and Protocols*, ed. S. J. Hurst, Humana Press, Totowa, NJ, 2011, pp. 51-62.
4. Chen, O., Zhao, J., Chauhan, V. P., Cui, J., Wong, C., Harris, D. K., Wei, H., Han, D., Fukumura, D., Jain, R. K., and Bawendi, M. G., Compact high-quality CdSe-CdS core-shell nanocrystals with narrow emission linewidths and suppressed blinking, *Nat. Mater.*, **2013**, 12, 445.
5. Wichner, S. M., Mann, V. R., Powers, A. S., Segal, M. A., Mir, M., Bandaria, J. N., DeWitt, M. A., Darzacq, X., Yildiz, A., and Cohen, B. E., Covalent Protein Labeling and Improved Single-Molecule Optical Properties of Aqueous CdSe/CdS Quantum Dots, *ACS Nano*, **2017**, 11, 6773-6781.
6. Mann, V. R., Powers, A. S., Tilley, D. C., Sack, J. T., and Cohen, B. E., Azide-Alkyne Click Conjugation on Quantum Dots by Selective Copper Coordination., *ACS Nano*, **2018**, 12, 4469-4477.
7. Dukes, A. D., Samson, P. C., Keene, J. D., Davis, L. M., Wikswa, J. P., and Rosenthal, S. J., Single-Nanocrystal Spectroscopy of White-Light-Emitting CdSe Nanocrystals, *J. Phys. Chem. A*, **2011**, 115, 4076-4081.
8. Orfield, N. J., McBride, J. R., Wang, F., Buck, M. R., Keene, J. D., Reid, K. R., Htoon, H., Hollingsworth, J. A., and Rosenthal, S. J., Quantum Yield Heterogeneity among Single Nonblinking Quantum Dots Revealed by Atomic Structure-Quantum Optics Correlation, *ACS Nano*, **2016**, 10, 1960-1968.

CHAPTER III

SINGLE QUANTUM DOT IMAGING REVEALS PKC β -DEPENDENT ALTERATIONS IN MEMBRANE DIFFUSION AND CLUSTERING OF AN ATTENTION-DEFICIT HYPERACTIVITY DISORDER/AUTISM/BIPOLAR DISORDER-ASSOCIATED DOPAMINE TRANSPORTER VARIANT

Reprinted with permission from Thal, L. B., Tomlinson, I. D., Quinlan, M. A., Kovtun, O., Blakely, R. D., and Rosenthal, S. J., Single Quantum Dot Imaging Reveals PKC β -Dependent Alterations in Membrane Diffusion and Clustering of an Attention-Deficit Hyperactivity Disorder/Autism/Bipolar Disorder-Associated Dopamine Transporter Variant, ACS Chem. Neurosci., 2019, 10, 460-471. Copyright 2019. American Chemical Society.

3.1 Introduction

The catecholamine neurotransmitter dopamine is central to the modulation of neuronal pathways that control diverse behaviors including those linked to movement, reward, mood, attention, and cognition.^{1,2} Disrupted dopamine signaling is associated with multiple brain disorders such as Parkinson's disease (PD), schizophrenia, bipolar disorder (BPD), attention-deficit/hyperactive disorder (ADHD), and addiction.³⁻⁶ The presynaptic Na⁺/Cl⁻-coupled dopamine transporter (DAT) determines dopamine signaling amplitude and duration by actively clearing synaptic dopamine following vesicular release.⁷⁻⁹ Importantly, genetic polymorphisms of the human DAT gene (*DAT1*, *SLC6A3*) have been identified in cases of ADHD, BPD, autism spectrum disorder (ASD), PD, and juvenile dystonia.¹⁰⁻¹⁵ DAT endocytic trafficking at presynaptic terminals is likely a major regulatory mode of synaptic strength in dopamine neurons,¹⁶⁻¹⁹ a

process that can be referred to as vesicle trafficking, wherein DAT proteins are moved into and out of the plasma membrane from intracellular compartments. Consequently, constitutive and regulated vesicle trafficking is considered to be the principal determinant of functional DAT availability, though engagement of these mechanisms appears to be region dependent.^{20,21} DAT proteins can also engage cell surface trafficking or lateral membrane diffusion that can be impacted by DAT-associated proteins and disease-associated mutations revealed by total internal reflection fluorescence (TIRF) microscopy,^{22,23} fluorescence recovery after photobleaching (FRAP),²⁴ and single particle tracking (SPT) techniques.^{25,26}

Single molecule imaging offers information such as kinetics and dynamics of molecules in real-time, which would be lost in conventional ensemble measurements. The study of lateral diffusion at a single protein level requires an approach that uses bright probes, such as quantum dots (QDs), to achieve signal-to-noise ratios suitable for high spatiotemporal resolution. QDs exhibit unique photophysical properties that make them an attractive first choice for single molecule imaging applications,²⁷ which many groups have employed to investigate the diffusion dynamics of single transmembrane, neurotransmitter receptors, and transporter proteins (e.g., GABA receptors, glycine receptors, serotonin transporters, DAT).^{26,28-32} First, QDs offer a prolonged photostability required for imaging acquisition times on the order of minutes.²⁷ Second, QDs have broad absorption spectra and size-tunable narrow Gaussian photoluminescence profiles that permit simultaneous multicolor tracking with little to no spectral bleedthrough. As a product of high quantum yields and large absorption cross sections, QDs are also very bright upon laser irradiation.³³ Together, these properties have enabled the detection of single proteins in living cells targeted by antagonist- and antibody-conjugated biocompatible QDs.^{27,34} Because surface trafficking is believed to be a critical posttranslational regulatory mechanism,³⁵⁻³⁷ our group

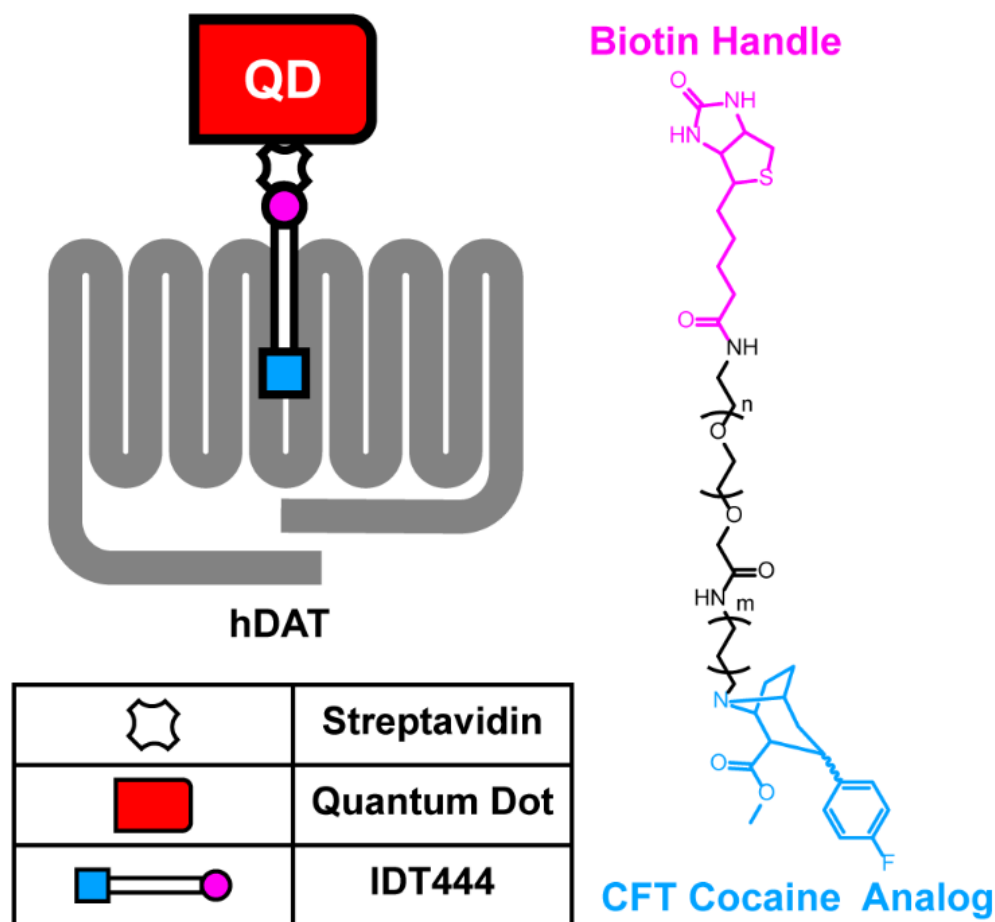


Figure 3.1. Schematic outlining single QD-DAT labeling architecture and chemical structure of the DAT-specific IDT444 affinity tool.

developed an antagonist-conjugated QD labeling approach to monitor individual membrane proteins in live cells (Figure 3.1).³⁸⁻⁴¹ Subsequently, we reported that the ADHD-associated DAT Cys615 coding variant exhibited significantly increased membrane mobility and a pronounced lack of dynamic response to lipid raft disruption and amphetamine (AMPH) stimulation.²⁶ Along with Cys615 as one of the multiple genetic DAT variants, a second variant, Val559, has been identified in subjects with distinct disorders associated with dopamine signaling dysfunction. The Val559 mutation was first identified in a female proband presenting with BPD¹¹ followed by its detection in two brothers with ADHD¹⁰ and subsequently in two unrelated adolescent males with

ASD.⁴² Studies with mice expressing the DAT Val559 variant demonstrate elevated extracellular dopamine levels, altered biochemical and behavioral responses to psychostimulants, and changes in behaviors linked to reward and impulsivity circuits.^{43,44} In live cell culture, the mutant transporter displays multiple, striking phenotypes. Mazei-Robison and colleagues demonstrated that the Val559 mutation, though not impacting DAT surface expression or dopamine uptake, induces anomalous dopamine efflux (ADE), whereby mutant transporters spontaneously move dopamine from the cytosol to the extracellular space.⁴⁵ DAT Val559 also demonstrates elevated levels of N-terminal phosphorylation at distal Ser residues.⁴² Mutation of these sites eliminates ADE, suggesting that N-terminal phosphorylation plays an essential role in sustaining dopamine reverse transport. Whether ADE is induced directly by transporter phosphorylation or is a consequence of changes in membrane distribution, lateral membrane trafficking, and/or the spatiotemporal organization of DAT with membrane partners is unclear. Here, we implemented our dynamic QD-based DAT monitoring approach to examine the impact of the DAT Val559 mutation on DAT membrane diffusion dynamics. We demonstrate that DAT exhibits increased lateral mobility in transiently transfected HEK-293 and SK-N-MC cells, movements that are also sensitive to mutations and pharmacological approaches impacting DAT phosphorylation. Using tracking and localization microscopy (TALM) and an intensity-based clustering analysis we developed, we demonstrate that the mutant targets to surface membrane clusters of HEK-293 cells to a lesser degree than the wild-type transporter. Our findings support the idea that disruption of normal DAT spatiotemporal organization may impose elevated risk for neuropsychiatric disorders linked to perturbed dopamine signaling.

3.2 Results and Discussion

3.2.1 Single QD Tracking Analysis Reveals DAT Val559 Has Aberrant Membrane Diffusion Dynamics.

DAT Val559 has been reported to display altered vesicle trafficking *in vitro* and *in vivo*.^{21,42} To assess the impact of the DAT Val559 mutation on lateral membrane trafficking, we targeted DATs with DAT antagonist-conjugated QDs.⁴⁰ Figure 3.1 illustrates the chemical structure of IDT444, the DAT-specific ligand used in our labeling paradigm, which makes use of the high-affinity carbomethoxy-fluorophenyl cocaine analog β -CFT (also known as WIN 35,428), an 11-carbon alkyl spacer to allow the antagonist to access its DAT binding site, and a PEG linker connected to a biotin molecule to provide for streptavidin-mediated QD binding.⁴⁰ This QD-IDT444 labeling strategy has proven successful in single QD tracking of DAT proteins.^{26,40} At concentrations of 100 nM IDT444 and <0.1 nM QD, we previously demonstrated that nonspecific binding was virtually eliminated.^{26,40} Because DAT Val559 is similar to wild-type DAT Ala559 in both β -CFT binding affinity and cocaine inhibition of [³H]-DA uptake,^{46,47} we expect IDT444 labeling to be comparable across cells expressing DAT Ala559 or Val559. Because dopamine D2 receptors (D2Rs) physically associate with DAT and promote DAT Val559-induced ADE,⁴⁸⁻⁵⁰ we pursued studies of multiple DAT variants (e.g., A559V, YFPDAT, YFPDAT S/ D, DAT S53A, DAT S53D, A559V + S53A, A559V + S53D) in HEK-293 cells that endogenously express D2Rs.⁵⁰ QD-labeled human DAT Ala559 and human DAT Val559 were studied in live, transiently transfected HEK-293 cells and imaged using TIRF microscopy at 10 Hz. Representative trajectories for both DAT Ala559 and DAT Val559 coding variants are shown in Figure 3.2a and b. 4-(4-dimethylamino)phenyl-1-methylpyridinium (IDT307, APP+),^{51,52} a DAT-specific fluorescent analog of 1-methyl-4-phenylpyridinium (MPP+), was used to outline the cell

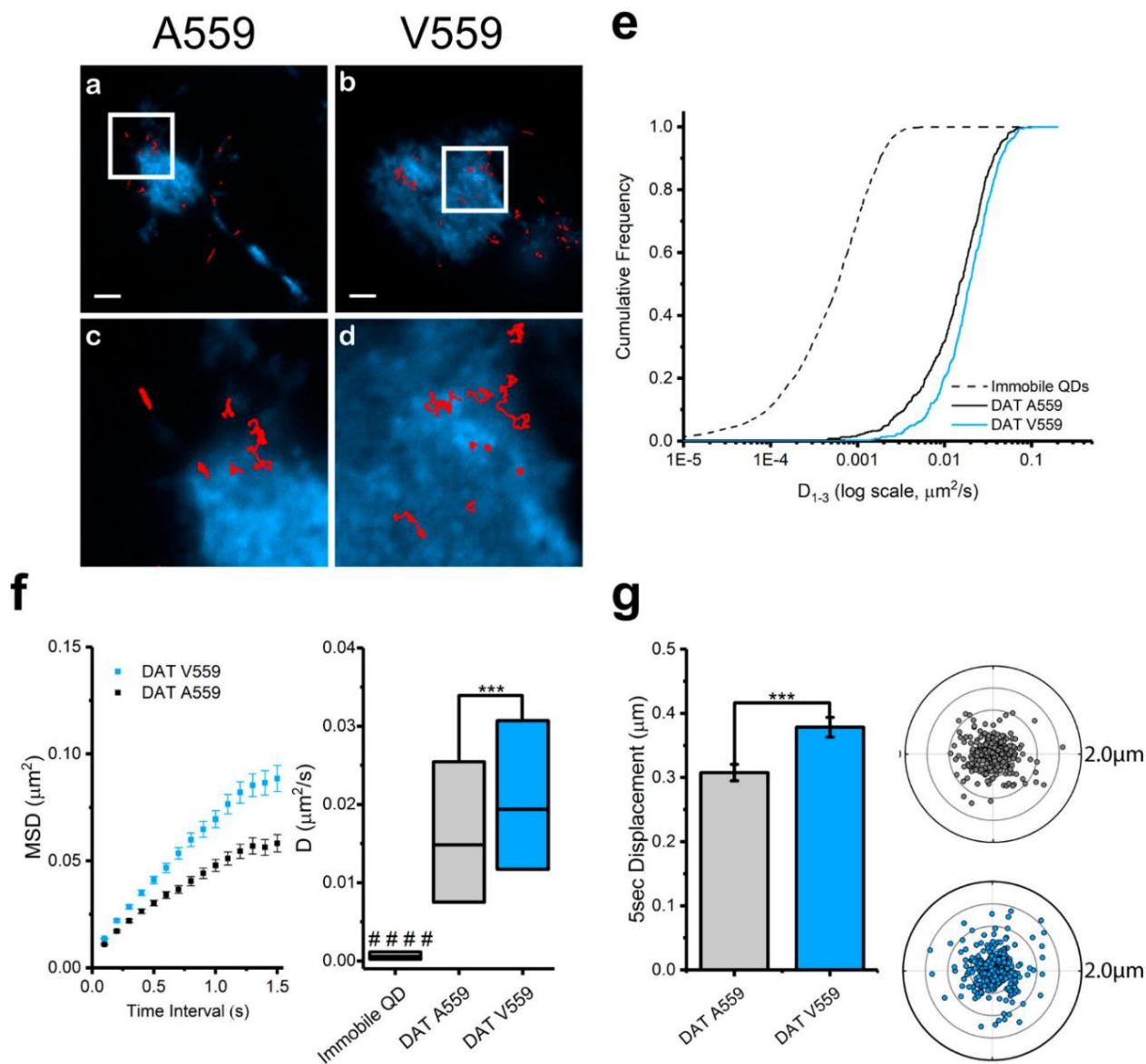


Figure 3.2. DAT Val559 exhibits faster mobility compared to that of DAT Ala559 transiently expressed in HEK-293 cells. (a,b) Representative trajectories collected over 60 s of QD-bound DAT and DAT Val559 coding variants superimposed to the IDT307 channel (scale bar = 5 μm). (c,d) Images at 4 \times magnification of images in a and b, respectively. (e) Cumulative frequency distributions of diffusion coefficients (D_{1-3}) of immobile QDs, DAT Ala559, and DAT Val559 (Kolmogorov–Smirnov 2-sample test, $p < 0.0001$). (f) Averaged mean square displacement (MSD) plots (mean \pm S.E.M.) and diffusion coefficient box plots (median, 25% and 75% interquartiles, one-way ANOVA followed by Bonferroni’s multiple comparison test, *** $p < 0.001$, ##### $p < 0.001$ comparing data sets to immobilized QDs as control) of trajectories analyzed for DAT Ala559 and DAT Val559. (g) A 5 s displacement bar graph (mean \pm S.E.M., unpaired Student’s t test, *** $p < 0.001$) and polar plots (outer radius limit = 2 μm) of single DAT Ala559 (gray) and DAT Val559 (blue). DAT displacements are normalized to their spatial origin. N (trajectories) are provided in Table A.1.

boundaries (Figure 3.2a–d). Diffusion coefficients (D_{1-3} , see Chapter 2 for details on calculations and analysis) were determined for populations of DAT Ala559 and DAT Val559 trajectories. Cumulative probability distributions (Figure 3.2e) of D_{1-3} values reveal a significant increase in DAT Val559 diffusion rates under basal conditions as compared to DAT Ala559. Averaged mean square displacement (MSD) curves show confined motion for both DAT Ala559 and DAT Val559, though the Val559 slope is significantly larger than the wild-type. DAT Val559 D_{1-3} interquartile ranges (25–75%) are also significantly greater than DAT Ala559 (Figure 3.2f). In addition to diffusion coefficients, 5 s radial displacement vectors were calculated by obtaining QD particle distance and direction traveled in 5 s (50 frames at 10 Hz) normalized to the particle position at the first frame (see Chapter 2). Averaged 5 s displacements for DAT Ala559 and DAT Val559 under basal conditions proved to be significantly different (Figure 3.2g). To increase the physiological relevance of our studies, we repeated our experiments using catecholaminergic neuroblastoma cells (SK-N-MC) derived from the human brain. Results in Figure A.1 demonstrate findings similar to those in our HEK-293 studies using SK-N-MC cells expressing DAT Ala559 and DAT Val559.

3.2.2 DAT Val559 Membrane Mobility is Insensitive to PMA-Triggered PKC Activation but Can Be Diminished by PKC β Inhibition.

DAT-mediated dopamine efflux and DAT surface density are impacted by protein kinase C (PKC) signaling.⁵ To examine whether faster DAT Val559 mobility is associated with transporter phosphorylation status, we examined the effects of general PKC activation on DAT Ala559 and DAT Val559 mobility using phorbol-12-myristate13-acetate (PMA), a diester that

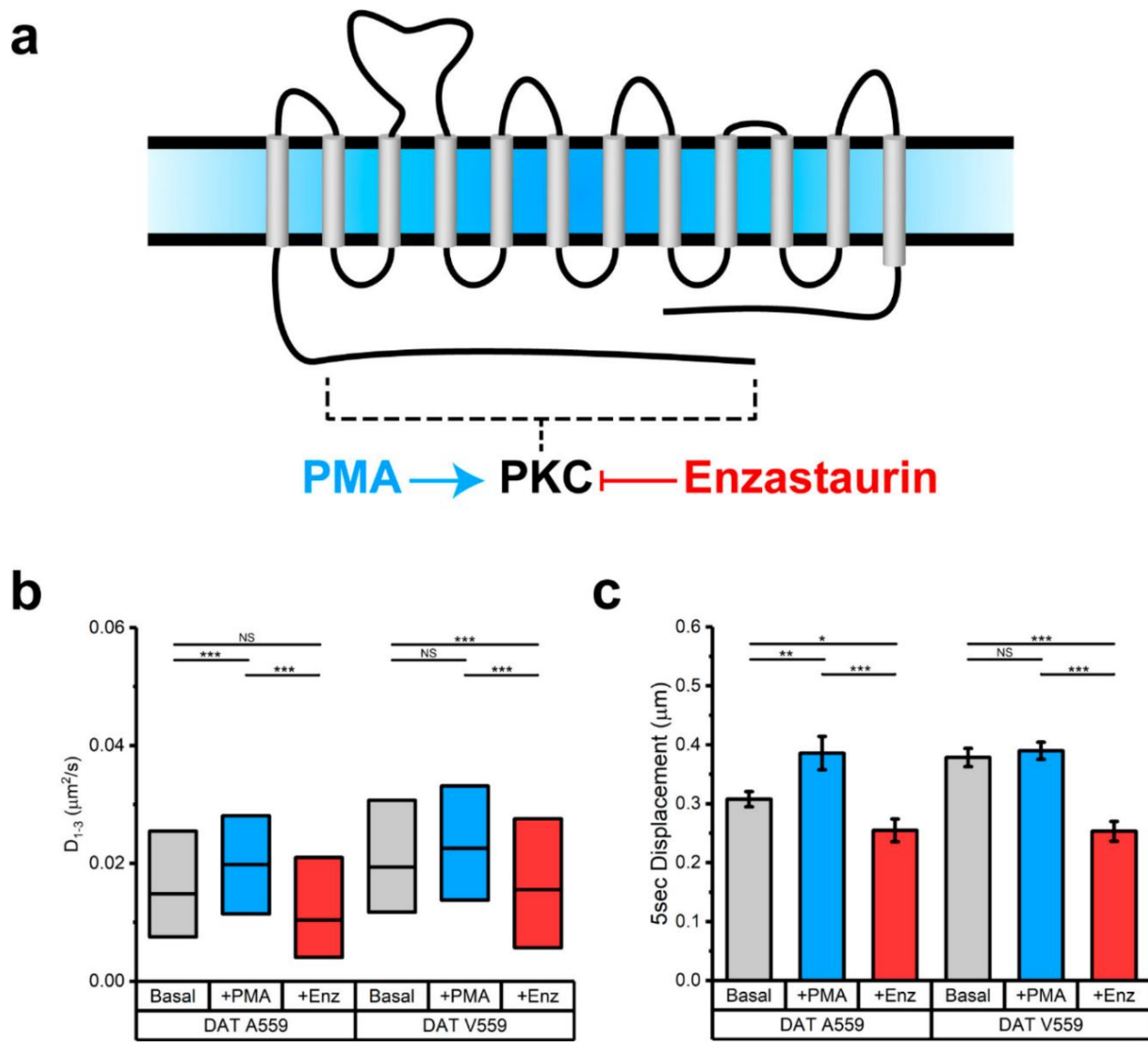


Figure 3.3. DAT Val559 diffusion is unresponsive to protein kinase C (PKC) activation and is attenuated by PKC β inhibition in HEK-293 cells. (a) Schematic of DAT with PKC activation by PMA highlighted in blue and PKC β inhibition by enzastaurin (Enz) highlighted in red. The dashed line denotes the general region of phosphorylation mediated by PKC activation. (b) Diffusion coefficient box plot (median, 25% and 75% interquartiles, one-way ANOVA followed by Bonferroni's multiple comparison test, NS $p > 0.05$, *** $p < 0.001$) of trajectories analyzed for DAT Ala559 and DAT Val559 under basal, stimulated (+PMA) conditions, and inhibited (+Enz) conditions. (c) A 5 s displacement bar graph (mean \pm S.E.M., unpaired Student's t test, NS $p > 0.05$ * $p < 0.05$, ** $p < 0.01$, *** $p < 0.001$) of trajectories analyzed for DAT Ala559 and DAT Val559 under basal, stimulated (+PMA), and inhibited (+Enz) conditions. N (trajectories) are provided in Table A.1.

binds to the catalytic C1 domain of PKC, which leads to stimulation of PKC activity. HEK-293 cells were preincubated with 100 nM PMA for 30 min prior to QD labeling. PKC activation induced an increase in DAT Ala559 D_{1-3} and 5 s displacements. However, these effects of PMA were not observed for DAT Val559 (Figure 3.3b, c). Similar results to those observed in HEK-293 cells were obtained with transfected SK-N-MC cells, demonstrating consistency across cell lines (Figure B.2).

PMA activates multiple PKC isoforms that can regulate DAT.⁵ Because PKC β regulates dopamine efflux,⁵³ PKC β activity is elevated in DAT Val559 expressing HEK-293 cells,⁴² and antagonism of PKC β restores AMPH-induced DAT internalization,⁵⁴ we focused further studies on this PKC isoform. Specifically, we tested the effects of the PKC β -specific inhibitor enzastaurin, previously shown to attenuate dopamine efflux *in vivo*,⁵⁵ to determine whether PKC β activity supports enhanced DAT Val559 membrane diffusion. DAT Ala559 and DAT Val559 transfected cells were preincubated with 1 μ M enzastaurin for 30 min prior to PMA treatment and QD labeling. Both DAT and DAT Val559 responded to PKC β inhibition by reduced D_{1-3} and reduced 5 s displacements (Figure 3.3b, c). Similar results were obtained using SK-N-MC cells as well (Figure A.2). These findings indicate that PKC β tone exists in our cell models that supports basal DAT Ala559 and DAT Val559 lateral mobility and that PMA can further enhance wild-type but not mutant DAT lateral mobility in a PKC β -dependent manner. Our findings are also consistent with a model whereby the elevated PKC β activity reported in DAT Val559 transfected cells leads to elevated DAT phosphorylation and increased lateral mobility,⁴² effects mimicked by treating DAT Ala559 expressing cells with PMA.

DAT Val559 has been shown to exhibit elevated phosphorylation of multiple N-terminal Ser residues, which is essential for DAT Val559 ADE.⁵⁰ We hypothesized that elevated Ser

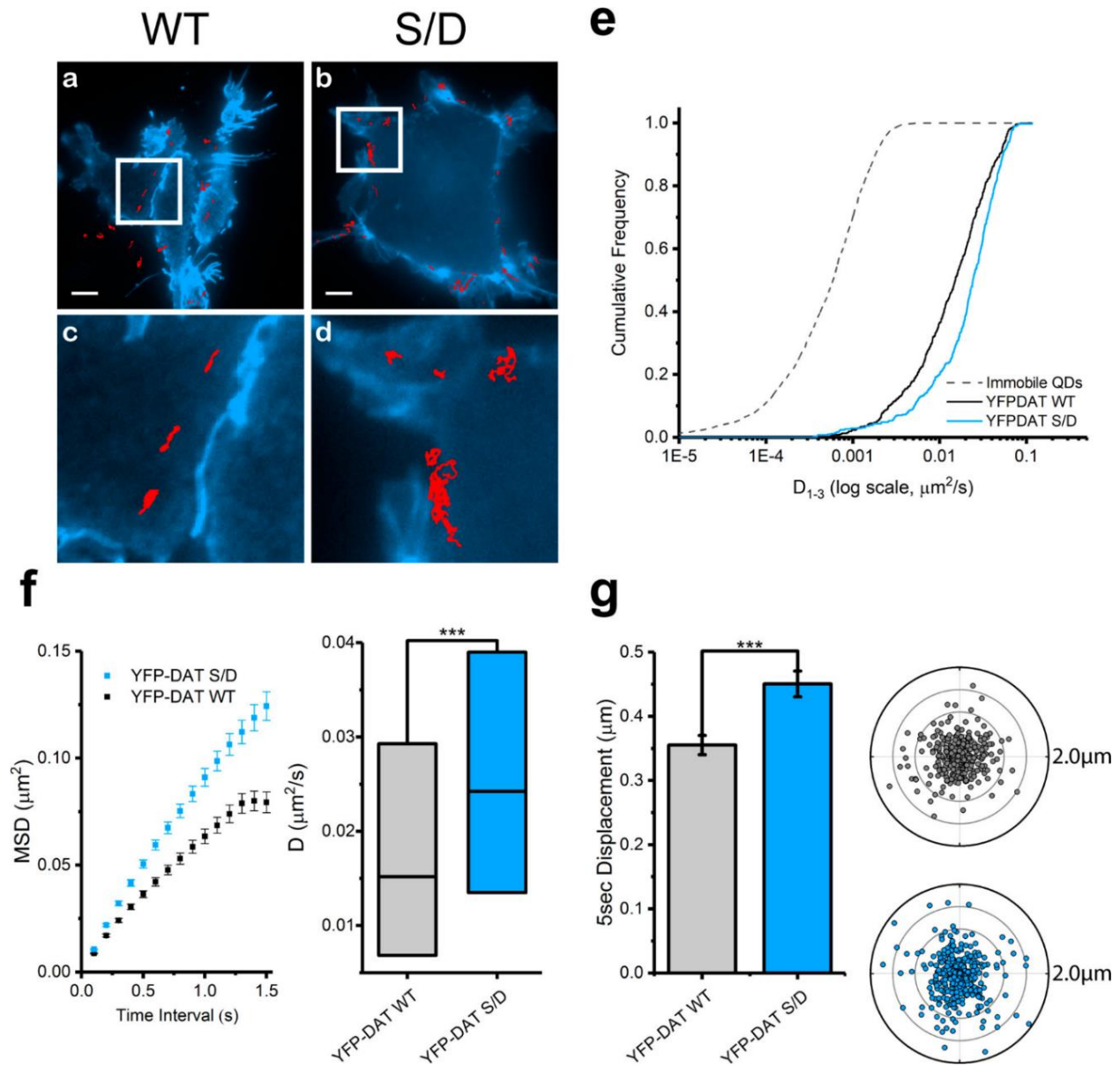


Figure 3.4. Phosphomimetic YFP-DAT S/D exhibits faster membrane mobility than that of wild-type YFP-DAT in HEK-293 cells. (a,b) Representative trajectories collected over 60 s of QD-bound YFP-DAT WT and YFP-DAT S/D superimposed to cell membranes outlined by YFP (scale bar = 5 μm). (c,d) Images at 4 \times magnification of images in a and b, respectively. (e) Cumulative frequency distributions of diffusion coefficients (D_{1-3}) of immobile QDs, YFP-DAT WT, and YFP-DAT S/D (Kolmogorov–Smirnov 2-sample test, $p < 0.0001$). (f) Averaged mean square displacement (MSD) plots (mean \pm S.E.M.) and a diffusion coefficient box plot (median, 25% and 75% interquartiles, one-way ANOVA followed by Bonferroni’s multiple comparison test, *** $p < 0.001$) of trajectories analyzed for YFP-DAT WT and YFP-DAT S/D. (g) A 5 s displacement bar graph (mean \pm S.E.M., unpaired Student’s t test, *** $p < 0.001$) and polar plots (outer radius limit = 2 μm) of single YFP-DAT WT (gray) and YFP-DAT S/D (blue). DAT-QD displacements are normalized to their spatial origin. N (trajectories) are provided in Table A.1.

phosphorylation of the DAT Val559 N-terminus might also be involved in the enhanced lateral mobility of this variant. To test this idea, we evaluated the impact of phosphomimetic mutations of the N-terminal Ser residues on lateral mobility using our antagonist-coupled QD approach. Here, Ser residues were mutated to Asp residues (S/D), which are negatively charged at pH 7, thus mimicking a phosphorylated state. We chose to use YFP-DAT and YFP-DAT S/D available for purchase from Addgene (see Chapter 2) considering green and yellow fluorescent proteins (GFP and YFP) moieties have been reported to induce no adverse effects on DAT function.^{56,57} Representative trajectories of QD-labeled YFP-DAT S/D demonstrate a greater area explored compared to QD-labeled YFP-DAT (Figure 3.4a–d). In Figure 3.4e, the cumulative probability distribution plot of D_{1-3} clearly demonstrates an increase in YFP-DAT S/D diffusion rate compared to that of YFP-DAT. Complementing the mobility of DAT Val559, YFP-DAT S/D has elevated D_{1-3} and 5 s displacements compared to those of YFP-DAT. Results using SK-N-MC are in agreement with these data (Figure A.3).

3.2.3 A559V-Induced Ser53 Phosphorylation Increases Membrane DAT Mobility.

In addition to the phosphorylation of N-terminal Ser residues, juxtamembrane DAT residue Thr53 (Ser53 in humans) accounts for a portion of basal DAT phosphorylation in transfected cells and *in vivo*.⁵⁸ Phosphorylation of Thr53 has been reported to impact dopamine uptake and AMPH-induced efflux,⁵⁸ whereas spatiotemporal effects of Thr53 phosphorylation on DAT lateral mobility remain unexplored. Intriguingly, elevated DAT Thr53 phosphorylation is evident in DAT Val559 knock-in mice²¹ in concert with elevated DAT Val559 surface expression and ADE. Thus, we explored a possible contribution of Ser53 phosphorylation to DAT membrane mobility. Upon

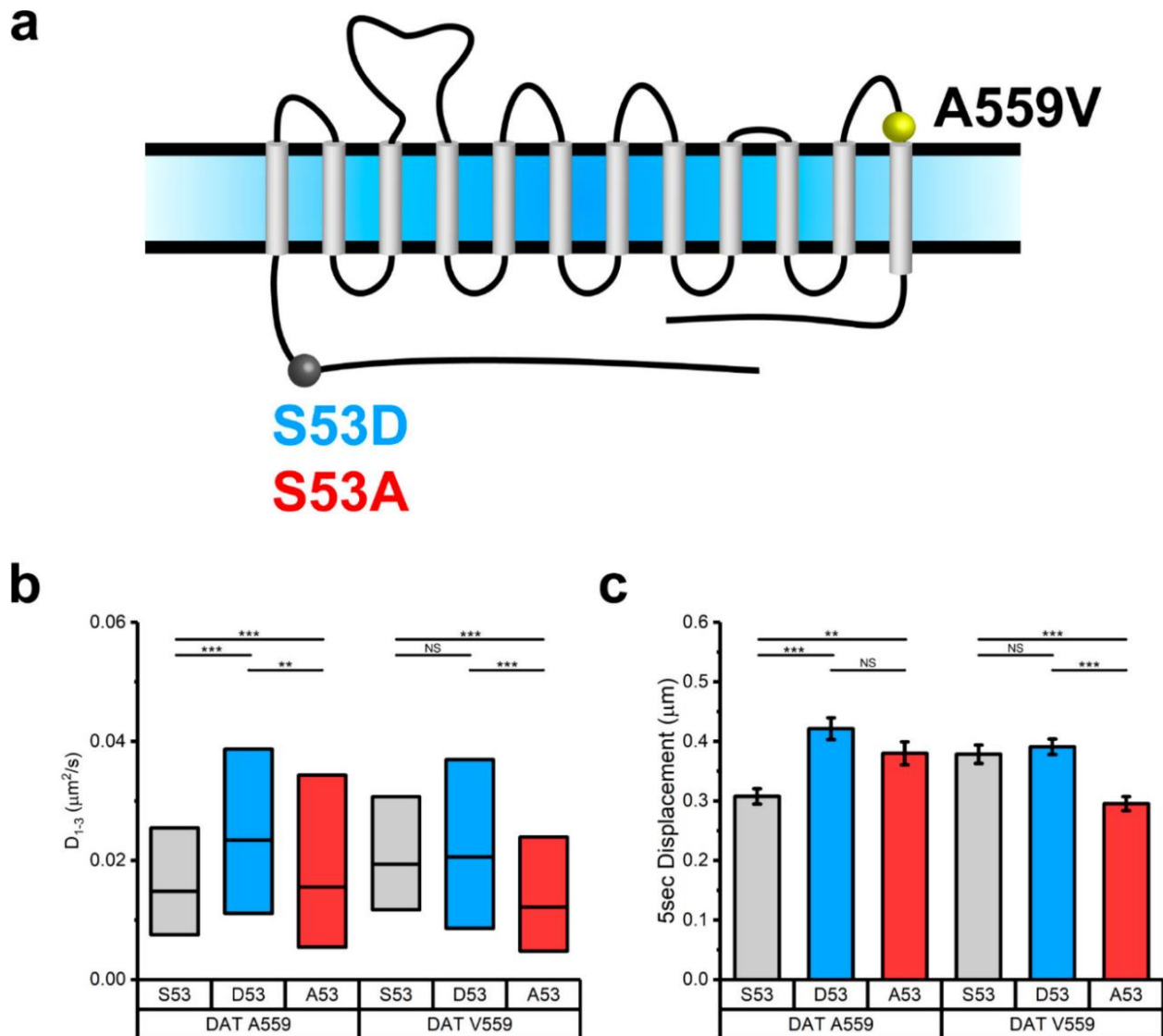


Figure 3.5. S53 phosphorylation alters mobility of DAT and DAT Val559. (a) Schematic of DAT and positions of variants tested. The A559V site is highlighted in yellow; S53A is highlighted in blue, and S53D is highlighted in red. (b) Diffusion coefficient box plot (median, 25% and 75% interquartiles, one-way ANOVA followed by Bonferroni's multiple comparison test, NS $p > 0.05$, ** $p < 0.01$ *** $p < 0.001$) of trajectories analyzed for Ser53, Asp53, and Ala53 under DAT Ala559 and DAT Val559 backgrounds. (c) A 5 s displacement bar graph (mean \pm S.E.M., unpaired Student's t test, NS $p > 0.05$, ** $p < 0.01$, *** $p < 0.001$) of trajectories analyzed for Ser53, Asp53, and Ala53 under DAT Ala559 and DAT Val559 backgrounds. N (trajectories) are provided in Table A.1.

generating diffusion profiles for DAT Ala559 and DAT Val559 expressing phosphorylation-occluded (S53A) and phosphomimetic (S53D) mutations, we observed a significant increase in D_{1-3} and 5 s displacements comparing DAT Ala559,Asp53 to DAT Ala559 populations, whereas DAT Val559,Asp53 exhibited no significant difference in D_{1-3} or 5 s displacements compared to those of DAT Val559 populations (Figure 3.5b, c).

Additionally, we observed that the DAT Val559,Ala53 mutant exhibited lower D_{1-3} and 5 s displacements compared to those of DAT Val559. Unexpectedly, the DAT Ala559,Ala53 mutant exhibited higher D_{1-3} and faster 5 s displacements than those of DAT Ala559, which may reflect a nonspecific impact of the Ala53 substitution on the membrane transporter diffusion. Nonetheless, occluding Ser53 phosphorylation in DAT Val559 with the Ala53 substitution resulted in diffusion coefficients comparable to those of DAT Ala559, consistent with a model where elevated phosphorylation at Ser53 in DAT Val559 is essential to the mutant's increased lateral mobility. Given that phosphorylation at distal N-terminal Ser residues as well as at Ser53 appears required for increased lateral mobility of DAT Val559, we suggest that these sites may “communicate” with each other through either transmitted conformational changes in the N-terminus or through changes in protein associations that impact transporter lateral mobility. In this regard, a number of DAT-associated proteins interact with the N-terminus including D2Rs, syntaxin 1A, and kappa opioid receptors.^{49,59,60} Future studies of DAT Val559 lateral mobility should explore contributions of disrupted associations of one or more of these proteins.

3.2.4 DAT Val559 Exhibits Reduced Clustering at the Apical Surface of HEK-293 Cells.

Several groups demonstrated that DAT undergoes oligomerization via various biochemical

and optical approaches.⁶¹⁻⁶⁵ A more recent superresolution microscopy study demonstrated that DAT proteins are organized into functional, cholesterol-dependent nanodomains in both transfected CAD cells and dopamine neurons.⁶⁶ Moreover, transmembrane domain 12 (TM12), where the Ala559Val mutation is located, has been suggested to support dimer formation in DAT via *in silico* experiments as well as SERT proteins via *in vitro* and *in silico* studies.⁶⁷⁻⁶⁹ To explore the possibility of the Ala559Val mutation altering DAT clustering, we evaluated DAT Val559 clustering at the apical surface of HEK-293 cells by widefield epifluorescence microscopy. Consistent with our tracking experiments, we treated cells expressing DAT Ala559 and DAT Val559 with 100 nM IDT444 and <0.1 nM QD. Briefly, we analyzed clusters by an in-house-developed intensity-based algorithm (see Chapter 2, Figure 3.6a) where integrated density (ID) values were obtained by integrating PSF from acquired images (Figure 6b, c). Higher ID values indicate the presence of clustered DAT-QDs (Figure 3.6c). For the best visualization of clusters, TALM reconstructed maps are provided (Figure 3.7a) for both DAT Ala559 and DAT Val559. We fit ID distributions with a lognormal function and used quantile-quantile (Q-Q) plots to compare ID values that fall outside of the fit with a 99% confidence value. DAT Ala559 ID values clearly indicate a distinct population of density values that fall outside the lognormal fit in the cluster regime, unlike DAT Val559 ID values that deviate less from the reference line (Figure 3.7b). These findings indicate that, in addition to an increase in lateral mobility, DAT Val559 proteins appear to cluster less on the apical surface of HEK-293 cells with other labeled transporters. These changes may preclude interactions with other DAT regulators that support normal dopamine influx/efflux bias and proper regulation of the transporter by cell signaling mechanisms. Notably, studies in the literature are mixed with respect to whether cocaine impacts multimer formation with differences possibly related to expression systems, levels of DAT

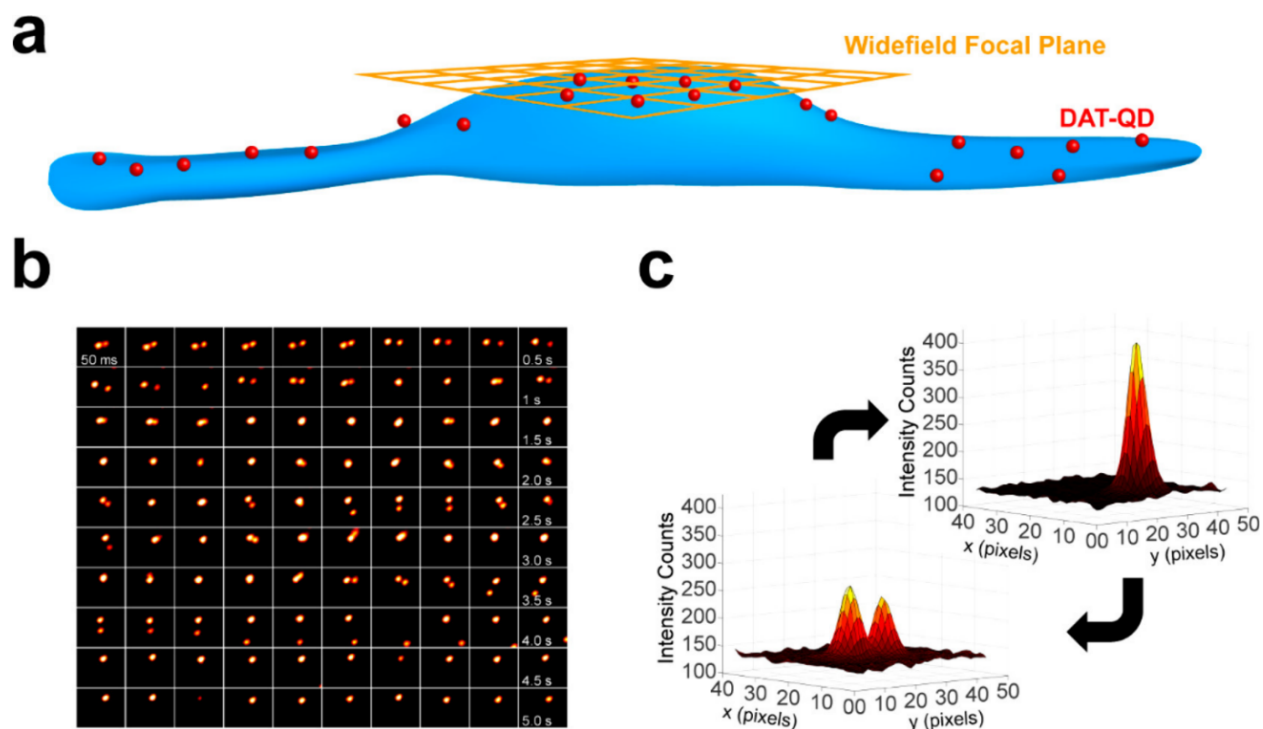


Figure 3.6. Intensity-based widefield imaging analysis reveals clusters at the apical cell surface. (a) Cartoon outlining the experimental widefield focal plane (orange) and DAT-QD (red) localization. (b) Representative montage of widefield epifluorescence micrographs of two DAT-QD PSFs interacting over a period of 5 s. (c) 3D surface plots of representative PSFs for single DAT-QDs and DAT-QD clusters.

expressed, and methods for multimer capture.^{63,64,70–72} Although we used low concentrations of IDT444-conjugated QDs to afford labeling of a small number of targets, additional studies are needed to know whether the binding of probes to these transporters has effects on multimer formation probability on its own. Studies using TIRF approaches with GFP-tagged transporters in the presence and absence of IDT444 present one possible route to explore this possibility.⁷³

In the model suggesting that alterations in cholesterol may indirectly influence DAT Val559 engagement in multi-transporter clusters, conformational changes and/or steric clashes that DAT Val559 imparts on TM12 may shift the equilibrium from a stabilized clustered state in

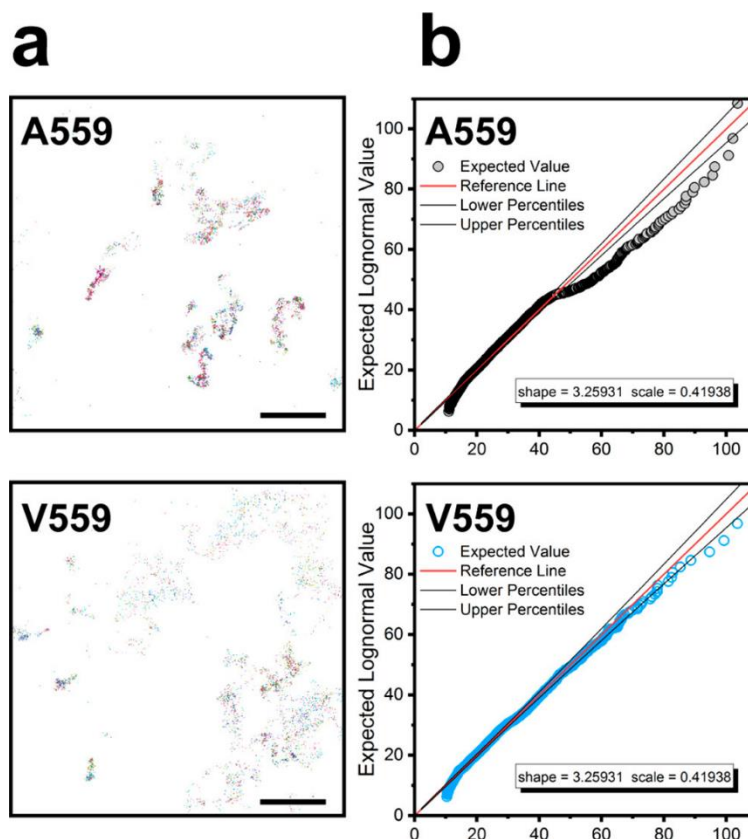


Figure 3.7. DAT Val559 has a lower propensity to reside in clusters at the apical surface of HEK-293 cells. (a) TALM reconstructions of DAT Ala559-QD and DAT Val559-QD PSFs from 1000-frame time series (scale bars = 2 μ m). Q-Q plots (99% confidence intervals, black) of background-subtracted integrated intensity values for DAT Ala559 and DAT Val559. Upper and lower percentiles are calculated with a 99% confidence. $N_{A559} = 1871$, $N_{V559} = 1864$, 26 cells analyzed.

membrane rafts toward a more mobile, efflux-prone dissociated state. This would agree with the idea explored by Sitte and Freissmuth in which oligomerization acts as an important factor in reverse dopamine transport.⁷⁴ Such modification in the DAT membrane lipid environment could affect the efficacy of DAT regulation by endogenous G protein coupled receptors, such as D2R, that result in dysfunctional DAT Val559 phenotypes. Another component that could be affecting DAT clustering is phosphatidylinositol 4,5-biphosphate (PIP₂) interaction with the N-terminus of Val559. Interestingly, an unphosphorylated DAT N-terminus interacts with PIP₂ *in silico*,⁷⁵ which

the Galli group reported enables consequent AMPH-induced efflux.⁷⁶ The possibility of impaired efflux as a result of Val559 mistargeting PIP₂ pools cannot be easily reconciled with the observation of PIP₂ electrostatic interaction with the N-terminus being necessary for AMPH-induced efflux.⁷⁶ However, considering the phosphorylation status of DAT is important in PIP₂ binding and direct PIP₂ binding has been shown to facilitate membrane oligomerization of SERT,⁷³ we cannot exclude the possibility of impaired interaction between the DAT Val559 and PIP₂.

3.3 Conclusions

Neuropsychiatric disease-derived DAT missense mutations demonstrate both trafficking-dependent and -independent DAT modes of transporter dysfunction, reinforcing perturbed synaptic dopamine homeostasis as a risk determinant for neuropsychiatric disease. Although the underlying molecular mechanisms of DAT dysregulation in neuropsychiatric disorders remain to be fully elucidated, recent evidence suggests that disrupted DAT membrane microdomain compartmentalization is potentially a common culprit of DAT-mediated dopamine pathology.^{26,77} Previously, we demonstrated that the ADHD-associated DAT coding Cys615 demonstrates alterations in membrane lateral mobility. Here, we provide the first single molecule tracking evidence for the DAT Val559 variant, a mutation found in subjects with ADHD, ASD, and BPD. Like DAT Cys615, DAT Val559 is more mobile compared to DAT under basal conditions. Longstanding evidence indicating that PKC mediates N-terminal phosphorylation of DAT at Ser and Thr residues,⁵ and our observation of the DAT Val559 variant exhibiting altered diffusion rates, led us to perform pharmacological investigation of requirements for PKC-mediated phosphorylation. We demonstrate that DAT Val559 mobility is unresponsive to PKC activation

but is attenuated by a potent and selective PKC β inhibitor. Furthermore, DAT phosphomimicked at distal serine residues is more mobile, supporting N-terminal phosphorylation as one determinant of DAT membrane diffusion. Adding to the growing appreciation of the role of Ser/Thr53 phosphorylation in DAT function, we provide evidence that phosphorylation at this site mobilizes DAT for increased lateral diffusion, effects (phosphorylation and mobilization) instituted constitutively in the DAT Val559 variant. We report here the first experimental evidence of reduced DAT Val559 clustering related to aberrant membrane mobility.

Several groups have reported PKC modulation of DAT endocytic trafficking observed in heterologous cells to be absent in cultured midbrain neurons.^{24,78–80} In contrast, Gabriel et al. recently reported PKC-mediated action on DAT trafficking observed intact striatal slices.²³ It is possible that some of this discrepancy may derive from culture versus slice approaches or the study of circuits that differentially support regulated DAT trafficking. For instance, Gowrishankar et al. found in studies of acute brain slices that D2R-dependent DAT trafficking occurs in dorsal but not ventral striatum.²¹ Currently, the degree to which Val559 variant proteins diffuse and cluster *in vivo* is unknown, though this is a goal for our efforts moving forward.

As the ADHD-associated DAT Cys615 variant also demonstrates increased lateral mobility,²⁶ disrupted membrane localization may be a common attribute of disease-associated changes in neurotransmitter transporter availability and/or function. Beyond this more general conclusion, our results reveal previously unreported perturbations of the DAT Val559 variant membrane dynamics implicating PKC β activation as an important determinant of transporter lateral mobility. Future studies are needed to dissect whether altered DAT Val559 membrane dynamics are a consequence of disrupted interactions between membrane domains enriched with cholesterol and/or PIP₂. Resolution of this question may lead to new opportunities for

neuropsychiatric disease intervention.

3.4 References

1. Giros, B. and Caron, M. G., Molecular characterization of the dopamine transporter, *Trends Pharmacol. Sci.*, **1993**, 14, 43–49.
2. Palmiter, R. D., Dopamine signaling in the dorsal striatum Is essential for motivated behaviors. *Ann. N. Y. Acad. Sci.*, **2008**, 1129, 35–46.
3. Bannon, M. J., Michelhaugh, S. K., Wang, J., and Sacchetti, P. The human dopamine transporter gene: gene organization, transcriptional regulation, and potential involvement in neuropsychiatric disorders, *Eur. Neuropsychopharmacol.*, **2001**, 11, 449–455.
4. Howes, O., McCutcheon, R., and Stone, J., Glutamate and dopamine in schizophrenia: An update for the 21st century, *J. Psychopharmacol.*, **2015**, 29, 97–115.
5. Bermingham, D. P. and Blakely, R. D., Kinase-dependent regulation of monoamine neurotransmitter transporters, *Pharmacol. Rev.*, **2016**, 68, 888–953.
6. Nutt, D. J., Lingford-Hughes, A., Erritzoe, D., and Stokes, P. R. A., The dopamine theory of addiction: 40 years of highs and lows, *Nat. Rev. Neurosci.*, **2015**, 16, 305.
7. Giros, B., Jaber, M., Jones, S. R., Wightman, R. M., and Caron, M. G., Hyperlocomotion and indifference to cocaine and amphetamine in mice lacking the dopamine transporter, *Nature*, **1996**, 379, 606.
9. Gainetdinov, R. R., Jones, S. R., and Caron, M. G., Functional hyperdopaminergia in dopamine transporter knock-out mice, *Biol. Psychiatry*, **1999**, 46, 303–311.
9. Ralph, R. J., Paulus, M. P., Fumagalli, F., Caron, M. G., and Geyer, M. A., Prepulse inhibition deficits and perseverative motor patterns in dopamine transporter knock-out mice: Differential effects of D1 and D2 receptor antagonists, *J. Neurosci.*, **2001**, 21, 305– 313.
10. Mazei-Robison, M. S., Couch, R. S., Shelton, R. C., Stein, M. A., and Blakely, R. D., Sequence variation in the human dopamine transporter gene in children with attention deficit hyperactivity disorder, *Neuropharmacology*, **2005**, 49, 724–736.
11. Grünhage, F., Schulze, T. G., Müller, D. J., Lanczik, M., Franzek, E., Albus, M., Borrmann-Hassenbach, M., Knapp, M., Cichon, S., Maier, W., Rietschel, M., Propping, P., and Nöthen, M. M., Systematic screening for DNA sequence variation in the coding region of the human dopamine transporter gene (DAT1), *Mol. Psychiatry*, **2000**, 5, 275.

12. Hahn, M. K. and Blakely, R. D., The functional impact of SLC6 transporter genetic variation, *Annu. Rev. Pharmacol. Toxicol.*, **2007**, 47, 401–441.
13. Hansen, F. H., Skjørringe, T., Yasmineen, S., Arends, N. V., Sahai, M. A., Erreger, K., Andreassen, T. F., Holy, M., Hamilton, P. J., Neergheen, V., Karlsborg, M., Newman, A. H., Pope, S., Heales, S. J. R., Friberg, L., Law, I., Pinborg, L. H., Sitte, H. H., Loland, C., Shi, L., Weinstein, H., Galli, A., Hjermind, L. E., Møller, L. B., and Gether, U., Missense dopamine transporter mutations associate with adult parkinsonism and ADHD, *J. Clin. Invest.*, **2014**, 124, 3107–3120.
14. Kurian, M. A., Gissen, P., Smith, M., Heales, S. J. R., and Clayton, P. T., The monoamine neurotransmitter disorders: an expanding range of neurological syndromes, *Lancet Neurol.*, **2011**, 10, 721–733.
15. Hamilton, P. J., Campbell, N. G., Sharma, S., Erreger, K., Herborg Hansen, F., Saunders, C., Belovich, A. N., Consortium, N. A. A. S., Sahai, M. A., Cook, E. H., Gether, U., McHaourab, H. S., Matthies, H. J. G., Sutcliffe, J. S., and Galli, A., *De novo* mutation in the dopamine transporter gene associates dopamine dysfunction with autism spectrum disorder, *Mol. Psychiatry*, **2013**, 18, 1315.
16. Wu, S., Fagan, R. R., Uttamapinant, C., Lifshitz, L. M., Fogarty, K. E., Ting, A. Y., and Melikian, H. E., The dopamine transporter recycles via a retromer-dependent post-endocytic mechanism: Tracking studies using a novel fluorophore-coupling approach, *J. Neurosci.*, **2017**, 37, 9438–9452.
17. Wu, S., Bellve, K. D., Fogarty, K. E., and Melikian, H. E., Ack1 is a dopamine transporter endocytic brake that rescues a trafficking-dysregulated ADHD coding variant, *Proc. Natl. Acad. Sci. U. S. A.*, **2015**, 112, 15480–15485.
18. Wheeler, D. S., Underhill, S. M., Stolz, D. B., Murdoch, G. H., Thiels, E., Romero, G., and Amara, S. G., Amphetamine activates Rho GTPase signaling to mediate dopamine transporter internalization and acute behavioral effects of amphetamine, *Proc. Natl. Acad. Sci. U. S. A.*, **2015**, 112, E7138–E7147.
19. Zhu, S., Zhao, C., Wu, Y., Yang, Q., Shao, A., Wang, T., Wu, J., Yin, Y., Li, Y., Hou, J., Zhang, X., Zhou, G., Gu, X., Wang, X., Bustelo, X. R., and Zhou, J., Identification of a Vav2-dependent mechanism for GDNF/Ret control of mesolimbic DAT trafficking, *Nat. Neurosci.*, **2015**, 18, 1084.
20. Block, E. R., Nuttle, J., Balcita-Pedicino, J. J., Caltagarone, J., Watkins, S. C., Sesack, S. R., and Sorkin, A., Brain region-specific trafficking of the dopamine transporter, *J. Neurosci.*, **2015**, 35, 12845–12858.
21. Gowrishankar, R., Gresch, P. J., Davis, G. L., Katamish, R. M., Riele, J. R., Stewart, A. M., Vaughan, R. A., Hahn, M. K., and Blakely, R. D., Region-specific regulation of presynaptic dopamine homeostasis by D2 autoreceptors shapes the *In Vivo* impact of the neuropsychiatric

disease-associated DAT variant Val559, *J. Neurosci.*, **2018**, 38, 5302-5312.

22. Furman, C. A., Chen, R., Guptaroy, B., Zhang, M., Holz, R. W., and Gnegy, M., Dopamine and amphetamine rapidly increase dopamine transporter trafficking to the surface: Live-cell imaging using total internal reflection fluorescence microscopy, *J. Neurosci.*, **2009**, 29, 3328–3336.

23. Gabriel, L. R., Wu, S., Kearney, P., Bellve, K. D., Standley, C., Fogarty, K. E., and Melikian, H. E., Dopamine transporter endocytic trafficking in striatal dopaminergic neurons: differential dependence on dynamin and the actin cytoskeleton, *J. Neurosci.*, **2013**, 33, 17836–17846.

24. Eriksen, J., Rasmussen, S. G. F., Rasmussen, T. N., Vaegter, C. B., Cha, J. H., Zou, M.-F., Newman, A. H., and Gether, U., Visualization of dopamine transporter trafficking in live neurons by use of fluorescent cocaine analogs, *J. Neurosci.*, **2009**, 29, 6794–6808.

25. Sorkina, T., Caltagareone, J., and Sorkin, A., Flotillins regulate membrane mobility of the dopamine transporter but are not required for its protein kinase C dependent endocytosis, *Traffic*, **2013**, 14, 709–724.

26. Kovtun, O., Sakrikar, D., Tomlinson, I. D., Chang, J. C., ArzetaFerrer, X., Blakely, R. D., and Rosenthal, S. J., Single-quantum dot tracking reveals altered membrane dynamics of an attentiondeficit/hyperactivity-disorder-derived dopamine transporter coding variant, *ACS Chem. Neurosci.*, **2015**, 6, 526–534.

27. Rosenthal, S. J., Chang, J. C., Kovtun, O., McBride, J. R., and Tomlinson, I. D., Biocompatible quantum dots for biological applications, *Chem. Biol.*, **2011**, 18, 10–24.

28. Dahan, M., Levi, S., Luccardini, C., Rostaing, P., Riveau, B., and Triller, A., Diffusion dynamics of glycine receptors revealed by single-quantum dot tracking, *Science*, **2003**, 302, 442–445.

29. Bouzigues, C., Morel, M., Triller, A., and Dahan, M., Asymmetric redistribution of GABA receptors during GABA gradient sensing by nerve growth cones analyzed by single quantum dot imaging, *Proc. Natl. Acad. Sci. U. S. A.*, **2007**, 104, 11251–11256.

30. Frischknecht, R., Heine, M., Perrais, D., Seidenbecher, C. I., Choquet, D., and Gundelfinger, E. D., Brain extracellular matrix affects AMPA receptor lateral mobility and short-term synaptic plasticity, *Nat. Neurosci.*, **2009**, 12, 897–904.

31. Chang, J. C., Tomlinson, I. D., Warnement, M. R., Ustione, A., Carneiro, A. M. D., Piston, D. W., Blakely, R. D., and Rosenthal, S. J., Single molecule analysis of serotonin transporter regulation using antagonist-conjugated quantum dots reveals restricted, p38 MAPK-dependent mobilization underlying uptake activation, *J. Neurosci.*, **2012**, 32, 8919–8929.

32. Bailey, D. M., Catron, M. A., Kovtun, O., Macdonald, R. L., Zhang, Q., and Rosenthal, S. J., Single Quantum Dot Tracking Reveals Serotonin Transporter Diffusion Dynamics are Correlated

with Cholesterol-Sensitive Threonine 276 Phosphorylation Status in Primary Midbrain Neurons, *ACS Chem. Neurosci.*, **2018**, 9, 2534-2541.

33. McBride, J., Treadway, J., Feldman, L. C., Pennycook, S. J., and Rosenthal, S. J., Structural basis for near unity quantum yield core/shell nanostructures, *Nano Lett.*, **2006**, 6, 1496–1501.

34. Kovtun, O., Tomlinson, I. D., Bailey, D. M., Thal, L. B., Ross, E. J., Harris, L., Frankland, M. P., Ferguson, R. S., Glaser, Z., Greer, J., and Rosenthal, S. J., Single quantum dot tracking illuminates neuroscience at the nanoscale, *Chem. Phys. Lett.*, **2018**, 706, 741–752.

35. Choquet, D. and Triller, A., The role of receptor diffusion in the organization of the postsynaptic membrane, *Nat. Rev. Neurosci.*, **2003**, 4, 251.

36. Triller, A. and Choquet, D., New concepts in synaptic biology derived from single-molecule imaging, *Neuron*, **2008**, 59, 359–374.

37. Kahlig, K. M., Lute, B. J., Wei, Y., Loland, C. J., Gether, U., Javitch, J. A., and Galli, A., Regulation of dopamine transporter trafficking by intracellular amphetamine, *Mol. Pharmacol.*, **2006**, 70, 542–548.

38. Gussin, H. A., Tomlinson, I. D., Cao, D., Qian, H., Rosenthal, S. J., and Pepperberg, D. R., Quantum dot conjugates of GABA and muscimol: Binding to $\alpha_1\beta_2\gamma_2$ and ρ_1 GABA_A receptors, *ACS Chem. Neurosci.*, **2013**, 4, 435–443.

39. Gussin, H. A., Tomlinson, I. D., Little, D. M., Warnement, M. R., Qian, H., Rosenthal, S. J., and Pepperberg, D. R., Binding of muscimol-conjugated quantum dots to GABA_C receptors, *J. Am. Chem. Soc.*, **2006**, 128, 15701–15713.

40. Kovtun, O., Tomlinson, I. D., Sakrikar, D. S., Chang, J. C., Blakely, R. D., and Rosenthal, S. J., Visualization of the cocaine-sensitive dopamine transporter with ligand-conjugated quantum dots, *ACS Chem. Neurosci.*, **2011**, 2, 370–378.

41. Rosenthal, S. J., Tomlinson, I., Adkins, E. M., Schroeter, S., Adams, S., Swafford, L., McBride, J., Wang, Y., DeFelice, L. J., and Blakely, R. D., Targeting cell surface receptors with ligand-conjugated nanocrystals, *J. Am. Chem. Soc.*, **2002**, 124, 4586–4594.

42. Bowton, E., Saunders, C., Reddy, I. A., Campbell, N. G., Hamilton, P. J., Henry, L. K., Coon, H., Sakrikar, D., Veenstra-VanderWeele, J. M., Blakely, R. D., Sutcliffe, J., Matthies, H. J. G., Erreger, K., and Galli, A., SLC6A3 coding variant Ala559Val found in two autism probands alters dopamine transporter function and trafficking, *Transl. Psychiatry*, **2014**, 4, No. e464.

43. Mergy, M. A., Gowrishankar, R., Gresch, P. J., Gantz, S. C., Williams, J., Davis, G. L., Wheeler, C. A., Stanwood, G. D., Hahn, M. K., and Blakely, R. D., The rare DAT coding variant Val559 perturbs DA neuron function, changes behavior, and alters in vivo responses to psychostimulants, *Proc. Natl. Acad. Sci. U. S. A.*, **2014**, 111, E4779–E4788.

44. Davis, G. L., Stewart, A., Stanwood, G. D., Gowrishankar, R., Hahn, M. K., and Blakely, R. D., Functional coding variation in the presynaptic dopamine transporter associated with neuropsychiatric disorders drives enhanced motivation and context-dependent impulsivity in mice, *Behav. Brain Res.*, **2018**, 337, 61–69.
45. Mazei-Robison, M. S., Bowton, E., Holy, M., Schmudermaier, M., Freissmuth, M., Sitte, H. H., Galli, A., and Blakely, R. D., Anomalous dopamine release associated with a human dopamine transporter coding variant, *J. Neurosci.*, **2008**, 28, 7040–7046.
46. Mazei-Robison, M. S., and Blakely, R. D., Expression studies of naturally occurring human dopamine transporter variants identifies a novel state of transporter inactivation associated with Val382Ala, *Neuropharmacology*, **2005**, 49, 737–749.
47. Herborg, F., Andreassen, T. F., Berlin, F., Loland, C. J., and Gether, U., Neuropsychiatric disease-associated genetic variants of the dopamine transporter display heterogeneous molecular phenotypes, *J. Biol. Chem.*, **2018**, 293, 7250.
48. Bolan, E. A., Kivell, B., Jaligam, V., Oz, M., Jayanthi, L. D., Han, Y., Sen, N., Urizar, E., Gomes, I., Devi, L. A., Ramamoorthy, S., Javitch, J. A., Zapata, A., and Shippenberg, T. S., D2 receptors regulate dopamine transporter function via an extracellular signal-regulated kinases 1 and 2-dependent and phosphoinositide 3 kinase-independent mechanism, *Mol. Pharmacol.*, **2007**, 71, 1222–1232.
49. Lee, F. J., Pei, L., Moszczynska, A., Vukusic, B., Fletcher, P. J., and Liu, F., Dopamine transporter cell surface localization facilitated by a direct interaction with the dopamine D2 receptor, *EMBO J.*, **2007**, 26, 2127–2136.
50. Bowton, E., Saunders, C., Erreger, K., Sakrikar, D., Matthies, H. J., Sen, N., Jessen, T., Colbran, R. J., Caron, M. G., Javitch, J. A., Blakely, R. D., and Galli, A., Dysregulation of dopamine transporters via dopamine D2 autoreceptors triggers anomalous dopamine efflux associated with attention-deficit hyperactivity disorder, *J. Neurosci.*, **2010**, 30, 6048–6057.
51. Blakely, R. D., Mason, J. N., Tomlinson, I. D., and Rosenthal, S. J. Fluorescent substrates for neurotransmitter transporters. Google Patents US8647827B2, 2011.
52. Mason, J. N., Farmer, H., Tomlinson, I. D., Schwartz, J. W., Savchenko, V., DeFelice, L. J., Rosenthal, S. J., and Blakely, R. D., Novel fluorescence-based approaches for the study of biogenic amine transporter localization, activity, and regulation, *J. Neurosci. Methods*, **2005**, 143, 3–25.
53. Johnson, L. A. A., Guptaroy, B., Lund, D., Shamban, S., and Gnegy, M. E., Regulation of amphetamine-stimulated dopamine efflux by protein kinase C β , *J. Biol. Chem.*, **2005**, 280, 10914–10919.
54. Chen, R., Furman, C. A., Zhang, M., Kim, M. N., Gereau, R. W., Leitges, M., and Gnegy, M. E., Protein kinase C β is a critical regulator of dopamine transporter trafficking and regulates the behavioral response to amphetamine in mice, *J. Pharmacol. Exp. Ther.*, **2009**, 328, 912–920.

55. Zestos, A. G., Mikelman, S. R., Kennedy, R. T., and Gnegy, M. E., PKC β inhibitors attenuate amphetamine-stimulated dopamine efflux, *ACS Chem. Neurosci.*, **2016**, 7, 757–766.
56. Daniels, G. M. and Amara, S. G., Regulated trafficking of the human dopamine transporter: Clathrin-mediated internalization and lysosomal degradation in response to phorbol esters, *J. Biol. Chem.*, **1999**, 274, 35794–35801.
57. Carvelli, L., Moron, J. A., Kahlig, K. M., Ferrer, J. V., Sen, N., Lechleiter, J. D., Leeb-Lundberg, L. M., Merrill, G., Lafer, E. M., Ballou, L. M., Shippenberg, T. S., Javitch, J. A., Lin, R. Z., and Galli, A., PI 3-kinase regulation of dopamine uptake, *J. Neurochem.*, **2002**, 81, 859–869.
58. Foster, J. D., Yang, J.-W., Moritz, A. E., ChallaSivaKanaka, S., Smith, M. A., Holy, M., Wilebski, K., Sitte, H. H., and Vaughan, R. A., Dopamine transporter phosphorylation site threonine 53 regulates substrate reuptake and amphetamine-stimulated efflux, *J. Biol. Chem.*, **2012**, 287, 29702–29712.
59. Binda, F., Dipace, C., Bowton, E., Robertson, S. D., Lute, B. J., Fog, J. U., Zhang, M., Sen, N., Colbran, R. J., Gnegy, M. E., Gether, U., Javitch, J. A., Erreger, K., and Galli, A., Syntaxin 1A interaction with the dopamine transporter promotes amphetamine-induced dopamine efflux, *Mol. Pharmacol.*, **2008**, 74, 1101–1108.
60. Kivell, B., Uzelac, Z., Sundaramurthy, S., Rajamanickam, J., Ewald, A., Chefer, V., Jaligam, V., Bolan, E., Simonson, B., Annamalai, B., Mannangatti, P., Prisinzano, T. E., Gomes, I., Devi, L. A., Jayanthi, L. D., Sitte, H. H., Ramamoorthy, S., and Shippenberg, T. S., Salvinorin A regulates dopamine transporter function via a kappa opioid receptor and ERK1/2-dependent mechanism, *Neuropharmacology*, **2014**, 86, 228–240.
61. Torres, G. E., Carneiro, A., Seamans, K., Fiorentini, C., Sweeney, A., Yao, W.-D., and Caron, M. G., Oligomerization and trafficking of the human dopamine transporter: Mutational analysis identifies critical domains important for the functional expression of the transporter, *J. Biol. Chem.*, **2003**, 278, 2731–2739.
62. Sorkina, T., Doolen, S., Galperin, E., Zahniser, N. R., and Sorkin, A., Oligomerization of dopamine transporters visualized in living cells by fluorescence resonance energy transfer microscopy, *J. Biol. Chem.*, **2003**, 278, 28274–28283.
63. Hastrup, H., Sen, N., and Javitch, J. A., The human dopamine transporter forms a tetramer in the plasma membrane: Cross-linking of a cysteine in the fourth segment is sensitive to cocaine analogs, *J. Biol. Chem.*, **2003**, 278, 45045–45048.
64. Chen, N. and Reith, M. E. A., Substrates dissociate dopamine transporter oligomers, *J. Neurochem.*, **2008**, 105, 910–920.
65. Egaña, L. A., Cuevas, R. A., Baust, T. B., Parra, L. A., Leak, R. K., Hochendoner, S., Peña, K., Quiroz, M., Hong, W. C., Dorostkar, M. M., Janz, R., Sitte, H. H., and Torres, G. E., Physical

and functional interaction between the dopamine transporter and the synaptic vesicle protein synaptogyrin-3, *J. Neurosci.*, **2009**, 29, 4592–4604.

66. Rahbek-Clemmensen, T., Lycas, M. D., Erlendsson, S., Eriksen, J., Apuschkin, M., Vilhardt, F., Jørgensen, T. N., Hansen, F. H., and Gether, U., Super-resolution microscopy reveals functional organization of dopamine transporters into cholesterol and neuronal activity-dependent nanodomains, *Nat. Commun.*, **2017**, 8, 740.

67. Periole, X., Zeppelin, T., and Schiøtt, B., Dimer interface of the human serotonin transporter and effect of the membrane composition, *Sci. Rep.*, **2018**, 8, 5080.

68. Just, H., Sitte, H. H., Schmid, J. A., Freissmuth, M., and Kudlacek, O., Identification of an additional interaction domain in transmembrane domains 11 and 12 that supports oligomer formation in the human serotonin transporter, *J. Biol. Chem.*, **2004**, 279, 6650–6657.

69. Jayaraman, K., Morley, A. N., Szöllösi, D., Wassenaar, T. A., Sitte, H. H., and Stockner, T., Dopamine transporter oligomerization involves the scaffold domain, but spares the bundle domain, *PLoS Comput. Biol.*, **2018**, 14, No. e1006229.

70. Anderluh, A., Klotzsch, E., Reismann, A. W. A. F., Brameshuber, M., Kudlacek, O., Newman, A. H., Sitte, H. H., and Schütz, G. J., Single molecule analysis reveals coexistence of stable serotonin transporter monomers and oligomers in the live cell plasma membrane, *J. Biol. Chem.*, **2014**, 289, 4387.

71. Siciliano, C. A., Saha, K., Calipari, E. S., Fordahl, S. C., Chen, R., Khoshbouei, H., and Jones, S. R., Amphetamine reverses escalated cocaine intake via restoration of dopamine transporter conformation, *J. Neurosci.*, **2018**, 38, 484–497.

72. Sorkina, T., Ma, S., Larsen, M. B., Watkins, S. C., and Sorkin, A., Small molecule induced oligomerization, clustering and clathrin-independent endocytosis of the dopamine transporter, *eLife*, **2018**, 7, No. e32293.

73. Anderluh, A., Hofmaier, T., Klotzsch, E., Kudlacek, O., Stockner, T., Sitte, H. H., and Schütz, G. J., Direct PIP2 binding mediates stable oligomer formation of the serotonin transporter, *Nat. Commun.*, **2017**, 8, 14089.

74. Sitte, H. H. and Freissmuth, M., Amphetamines, new psychoactive drugs and the monoamine transporter cycle, *Trends Pharmacol. Sci.*, **2015**, 36, 41–50.

75. Khelashvili, G., Stanley, N., Sahai, M. A., Medina, J., LeVine, M. V., Shi, L., De Fabritiis, G., and Weinstein, H., Spontaneous inward opening of the dopamine transporter is triggered by PIP2-regulated dynamics of the N-terminus, *ACS Chem. Neurosci.*, **2015**, 6, 1825–1837.

76. Hamilton, P. J., Belovich, A. N., Khelashvili, G., Saunders, C., Erreger, K., Javitch, J. A., Sitte, H. H., Weinstein, H., Matthies, H. J., and Galli, A., PIP2 regulates psychostimulant behaviors through its interaction with a membrane protein, *Nat. Chem. Biol.*, **2014**, 10, 582.

77. Robinson, S. B., Hardaway, J. A., Hardie, S. L., Wright, J., Glynn, R. M., Bermingham, D. P., Han, Q., Sturgeon, S. M., Freeman, P., and Blakely, R. D., Sequence determinants of the *Caenorhabditis elegans* dopamine transporter dictating *in vivo* axonal export and synaptic localization, *Mol. Cell. Neurosci.*, **2017**, 78, 41–51.
78. Sorkina, T., Miranda, M., Dionne, K. R., Hoover, B. R., Zahniser, N. R., and Sorkin, A., RNA interference screen reveals an essential role of *nedd4-2* in dopamine transporter ubiquitination and endocytosis, *J. Neurosci.*, **2006**, 26, 8195–8205.
79. Rao, A., Simmons, D., and Sorkin, A., Differential subcellular distribution of endosomal compartments and the dopamine transporter in dopaminergic neurons, *Mol. Cell. Neurosci.*, **2011**, 46, 148–158.
80. Rao, A., Richards, T. L., Simmons, D., Zahniser, N. R., and Sorkin, A., Epitope-tagged dopamine transporter knock-in mice reveal rapid endocytic trafficking and filopodia targeting of the transporter in dopaminergic axons, *FASEB J.*, **2012**, 26, 1921–1933.

CHAPTER IV

LIGAND-CONJUGATED QUANTUM DOTS FOR FAST SUB-DIFFRACTION

PROTEIN TRACKING IN ACUTE BRAIN SLICES

Reprinted with permission of Thal, L.B., Mann, V.R., Sprinzen, D., McBride, J.R., Reid, K.R., Tomlinson, I.D., McMahon, D.G., Cohen, B.E., and Rosenthal S.J., Ligand-conjugated quantum dots for fast sub-diffraction protein tracking in acute brain slices, Biomater Sci. 2020, 8, 837-845, Copyright 2020. Royal Chemical Society.

4.1 Introduction

Fluorescence microscopy has long served as a cornerstone technique in biology for addressing many of the fundamental processes of life. Consequent to the dynamic nature of biomolecules, single molecule imaging approaches have been developed to achieve finer spatiotemporal resolution sufficient for dynamic molecular imaging in live cells.^{1,2} Single particle tracking (SPT) has been used to investigate protein localization and dynamics in mammalian cells and established the basis of protein dynamics such as membrane protein trafficking and clustering in detail.³⁻⁵ Neuronal membrane protein membrane dynamics have been investigated by SPT image analysis, proteins such as glycine,⁵ GABA, and glutamate-gated receptors,⁶⁻⁹ as well as epidermal growth factor receptors,¹⁰⁻¹² and G-protein coupled receptors.¹³ SPT approaches like these require bright probes such as semiconductor quantum dots (QDs) to achieve the high signal-to-background ratios (SBRs) needed to track individual proteins. In 2002, ligand-conjugated QDs were introduced as probes in order to specifically label serotonin transporters (SERT).¹⁴ Ligand conjugation of QDs have since been adapted to image single SERT and dopamine transporter

(DAT) proteins, finding alterations in diffusion patterns associated with neuropsychiatric diseases.^{15–21}

Many single molecule imaging studies rely on heterologous expression systems and cultured neurons, systems in which large SBRs arise from having imaging planes close to the glass substrate. In acute brain slices and other physiologically relevant environments, single molecule imaging has remained challenging and is a necessary next step to link mammalian physiology to protein dynamics. A key challenge is the development of specific, bright, and stable probes that can be imaged deep in tissue at millisecond SPT frame rates. While some organic fluorophores and fluorescent proteins exhibit high fluorescence quantum yields, the high excitation powers needed for SPT have been shown to cause significant photodamage to cells and the probes themselves.^{22–24} QDs may be tracked at lower fluences because of their large absorption cross-sections, which lead to enhanced emission, reduced photobleaching, and lower phototoxicity compared to conventional probes.²⁵

While various tissues have been imaged with QD labeling for ensemble analysis,^{26–28} few examples of QD tracking in brain tissue have been reported, leaving native 3D neuronal architectures largely unexplored.^{29–31} In this study, we provide a structural and photophysical basis for the importance of shell *geometry* of high quality CdSe/CdS QDs in single molecule imaging deep in living brain slices. These pseudo type II core/shell structures have been reported to have enhanced photon output,³² stability in common aqueous buffer, as well as much smaller hydrodynamic diameters compared to streptavidin-coated QDs frequently used in SPT experiments (Figure B.1).^{24,33} In the interest of transitioning single particle studies from *in vitro* to *ex vivo* platforms, we demonstrate here that these nanoparticles (i) maintain their photostability in oxygenated brain slice media (i.e., artificial cerebrospinal fluid, aCSF) and (ii) show significantly

great stability and less blinking than the widely-used QD655 probes (ThermoFisher) via a detailed ensemble and single particle investigation. Using energy-dispersive X-ray (EDS) chemical mapping, we show that thick, *symmetric* CdS shells are required for prolonged photostability in brain slice media. We substantiate our motivation for this study by successful subcellular localization imaging of dopamine transporters and SPT experiments of these probes in acute brain slices (20 nm localization precision, 10 Hz frame rates) using a conventional spinning-disk confocal microscope. To address commonly available QDs falling short of meeting the photophysical criteria for SPT of membrane proteins in oxygenated brain slice media, we introduce the blueprint of critical considerations in probe design. This study paves the way to development of probes for long-term monitoring of targeted protein dynamics in their native environments and sets the course for direct observation of these dynamics deep in the brain tissue of neuropsychiatric disease models.

4.2 Results and Discussion

4.2.1 Chemically Mapping Structural Differences in Core/Shell Aqueous Probes

The fluorescence efficiency and stability of a QD is exceedingly dependent on how well the shell passivates the core surface. Proper passivation relies on the degree of lattice mismatch, surface coverage, as well as by how many layers of shell are grown.³⁴ Although a thin shell can significantly enhance the QD fluorescence, these particles are far from robust and will photobleach rapidly in all but the most benign environments.³⁵ Conversely, too thick of a shell, as in those for ‘giant’ shelled quantum dots, leads to significant charge state emission that caps the ensemble

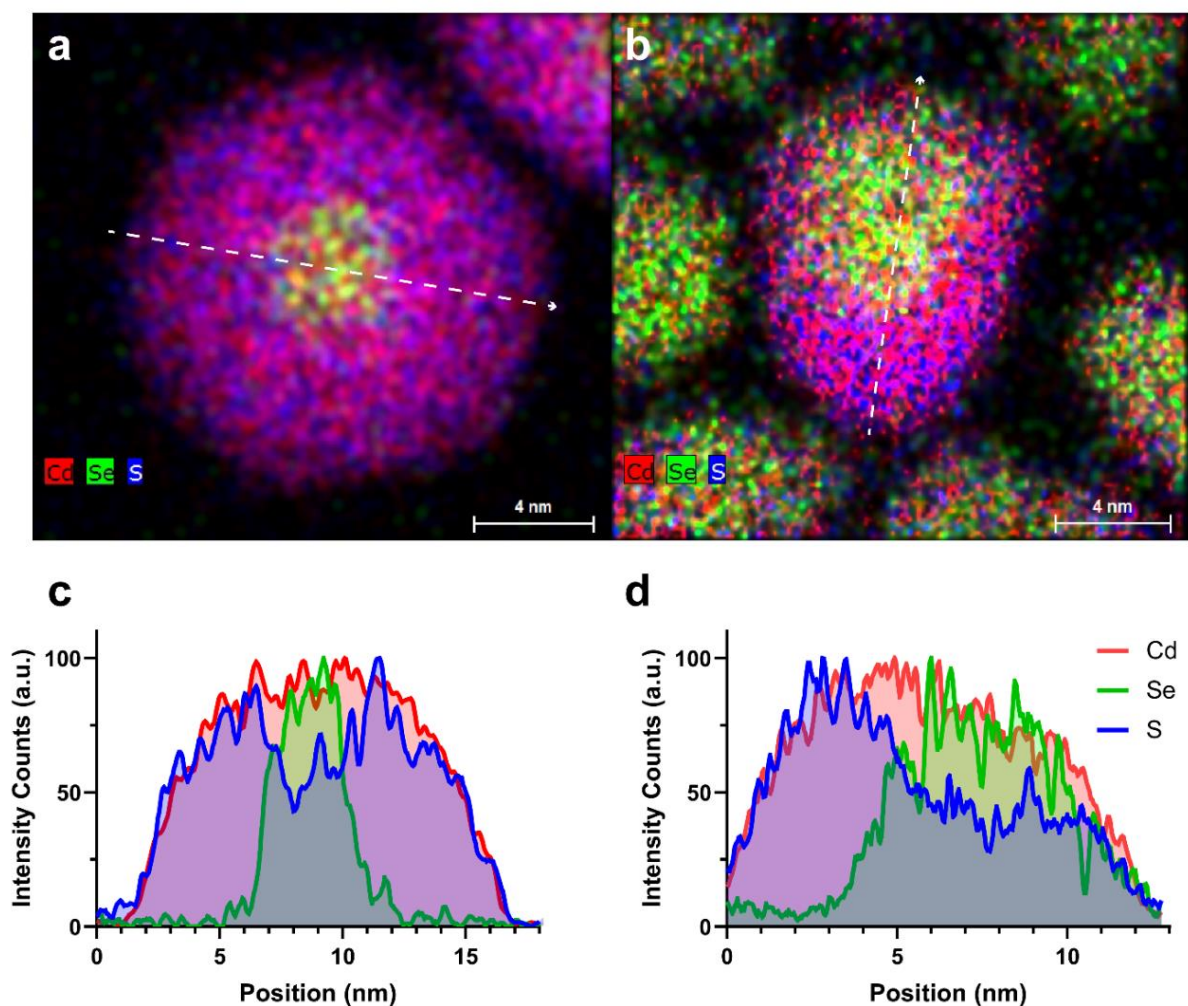


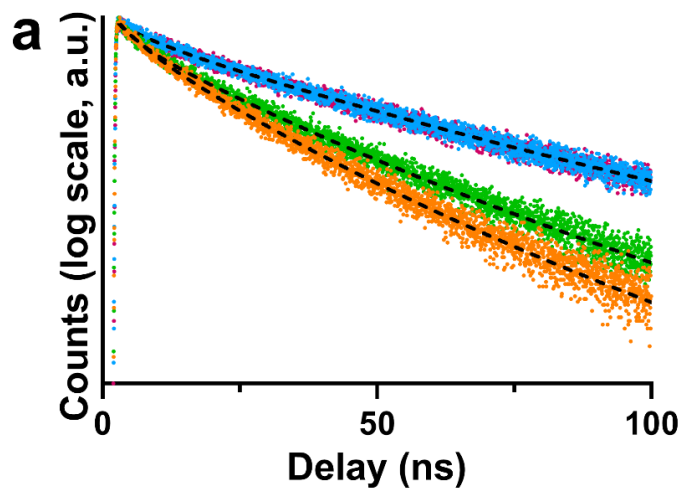
Figure 4.1. Elemental characterization of CdSe/CdS QD architectures. Combined Cd (red), Se (green), and S (blue) elemental maps of (a) symmetrically shelled QDs and (b) QD655s show core/shell structures. Linescans of the elemental maps (white arrows) Se distribution relative to Cd and S in both (c) symmetrically shelled QDs and (d) QD655s.

fluorescence to a maximum of roughly 50%.³⁵⁻³⁸ Ou Chen demonstrated that ~ 8 monolayers of a uniform CdS shell leads to a balance of high quantum yield and improved stability.³² Ultimately, in a chemically and physically challenging environment where a minimum QD hydrodynamic radius is desired, the amount and location of shell is critical for long-term performance. The clearest way to observe shell coverage is through STEM-EDS imaging.^{37,39} Figure 4.1 shows

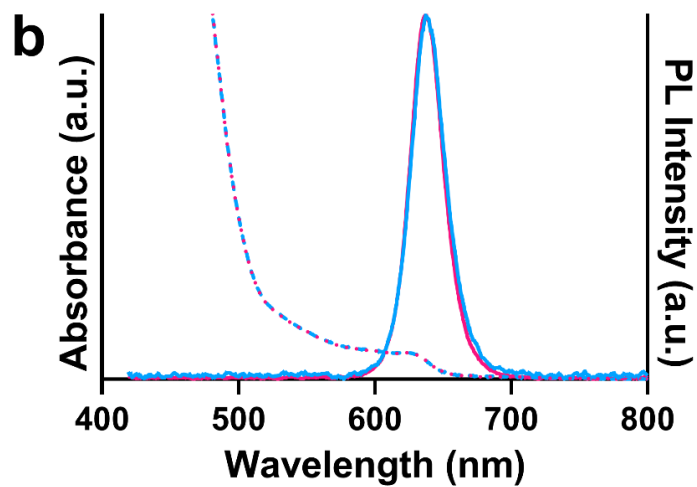
STEM-EDS maps of the QDs engineered for brain slice imaging and QD655s (HRTEM images also provided in Figure B.2). While both exhibit thick CdS shells, the QD655s dissimilar to our symmetrically shelled QDs show preferential shell growth along the c-axis leading to asymmetric shell coverage, as evident in the line scan (Figures 4.1c, d and B.3–B.5). The close proximity of the core to the surface likely enhances electron and hole overlap with trap sites that form during illumination. Notably, the native ligands on both types of QDs are encapsulated with an amphiphilic polymer which enables water solubility, while maintaining a similar particle size and colloidal stability (Figure B.6). Although ligand shells are needed for solution stability and chemical functionality, long term photostability relies on inorganic shell passivation. It is also worth noting that although these QD655s are quoted as having a ZnS shell, only trace amounts of Zn signal were detected for this particular batch (Figures B.7 and B.8).⁴⁰

4.2.2 Ensemble Photophysical Investigation

In order to compare the photostability of both these QD constructs in brain slice media, we performed time-resolved photoluminescence (TRPL) measurements on dilute concentrations of each QD type suspended in both 4-(2-hydroxyethyl)-1-piperazineethanesulfonic acid (HEPES) buffer and oxygenated cerebrospinal fluid. We note that HEPES is a commonly used buffer for storing QDs as well as for coupling techniques such as diimide/N-hydroxysuccinimide (e.g. EDC/NHS), making it a useful control. The samples were excited at low fluences ($\sim 1 \mu\text{J cm}^{-2}$). At these low fluences, we expect the majority of photo-excited QDs to contain a single electron–hole pair.³⁹ Interestingly, the symmetrically shelled QDs displayed similar lifetimes in both HEPES and oxygenated cerebrospinal fluid ($\tau_{\text{avg}} \sim 46.0 \pm 0.2 \text{ ns}$), indicating that the QDs retain



● symm-shelled QDs in HEPES ● QD655 in HEPES
 ● symm-shelled QDs in aCSF ● QD655 in aCSF



● symm-shelled QDs in HEPES ● QD655 in HEPES
 ● Symm-shelled QDs in aCSF ● QD655 in aCSF

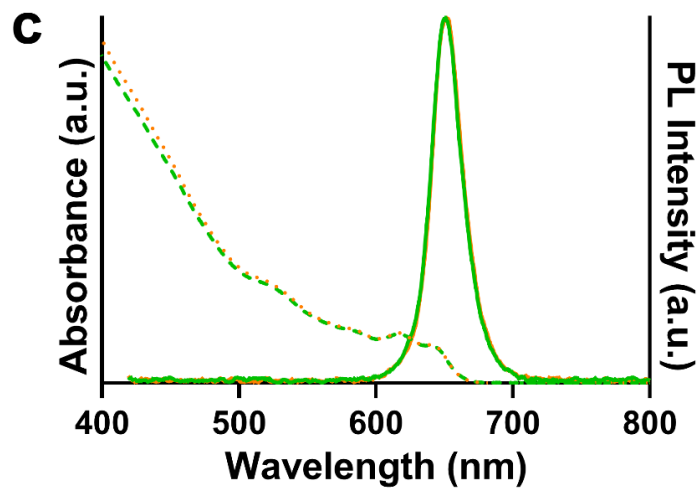


Figure 4.2. Ensemble photophysical profiles of symmetrically shelled (symm-shelled) CdSe/CdS QDs and QD655s in HEPES buffer or oxygenated cerebrospinal fluid (aCSF). (a) Transient PL dynamics of symm-shelled QDs and QD655s in HEPES and oxygenated aCSF. Absorbance (dotted) and emission (solid) spectra of (b) symm-shelled QDs and (c) QD655s in HEPES and oxygenated aCSF.

their photostability on exchange in the brain slice media (Figure 4.2a). In comparison, the lifetime of QD655s was notably shortened upon exchange into the brain slice media ($\tau_{\text{avg}} = 27.0 \pm 0.2$ ns in HEPES, $\tau_{\text{avg}} = 22.0 \pm 0.1$ ns in oxygenated cerebrospinal fluid) (Table B.1), suggesting symmetric shells are required to suppress O₂-mediated quenching.

To examine whether this apparent quenching is due to spectral-shifting processes such as etching or aggregation, UV-visible and PL spectroscopy in various buffers were performed. Interestingly, the differences observed in PL lifetimes of the commercial QD655s are not observed in the absorbance and photoluminescence spectra (Figure 4.2b,c). Considering oxygenated environments have been shown in general to quench the photoluminescence of QDs by creating defects at the nanocrystal surface that introduce nonradiative recombination centers, a process that is accelerated under high flux,⁴¹⁻⁴³ it is likely that O₂-rich media further quenches QD655s. In combination with our structural results that the cores of the QD655 probes are asymmetrically passivated (Figure 4.1b), these findings support the possibility of the cores being vulnerable to their environment. More generally, our results emphasize the need to investigate photoluminescence lifetimes of probes in their intended environments (e.g. oxygenated tissue media) during development and optimization.

4.2.3 Single QD Analysis in Biological Media

Further photophysical differences between QDs systems were measured using single-molecule imaging modalities. We first set out to test whether QD blinking is altered in brain slice media. Using a spinning-disk confocal microscope system (100 ms exposure time at 51 W cm^{-2}), PL intensity traces of single QDs incubated in oxygenated cerebrospinal fluid were compared to QDs incubated in HEPES as a negative control. Representative PL intensity time traces (Figure 4.3a) of the two QD types in both HEPES and oxygenated cerebrospinal fluid show QD classic PL fluctuations between high (ON) and low (OFF) emission intensity values. Binarization of the intensity traces by assigning time bins with intensity above 6σ of the background level (Figure 4.3b) clearly reveals strong blinking suppression of the symmetrically shelled QDs in both HEPES and cerebrospinal fluid. Furthermore, distributions in ON-fractions—the fraction of time a QD spends in the emissive state over the course of the experiment—display no significant difference between symmetrically shelled QD populations (Figure 4.3c) diluted in HEPES (ON-fraction = 0.87 ± 0.03) and oxygenated cerebrospinal fluid (ON-fraction = 0.89 ± 0.02). In contrast, QD655s are characterized by strong blinking with low ON-times in HEPES (ON-fraction = 0.27 ± 0.02) and even lower ON-times (ON-fraction = 0.16 ± 0.03) were observed for QDs in oxygenated cerebrospinal fluid (see Appendix B for statistics using data analysis with bootstrap-coupled estimation,⁴⁵ Figure B.9 and Table B.2). These low ON-times can also be attributed to incomplete passivation of the CdSe core in QD655s, resulting in greater overlap of excited charge carriers with the nanocrystal surface where they can become trapped and render the particles non-emissive.^{46–49} CdSe/CdS heterostructures display type II exciton behavior, in which holes are confined to the CdSe core whereas electrons may reside in core or CdS shell. The presence of thin CdS shell domains then opens the possibility of O_2 quenching of electrons that venture to the QD surface.^{50–52} Exposure of the poorly passivated QDs on exchange in oxygenated cerebrospinal fluid

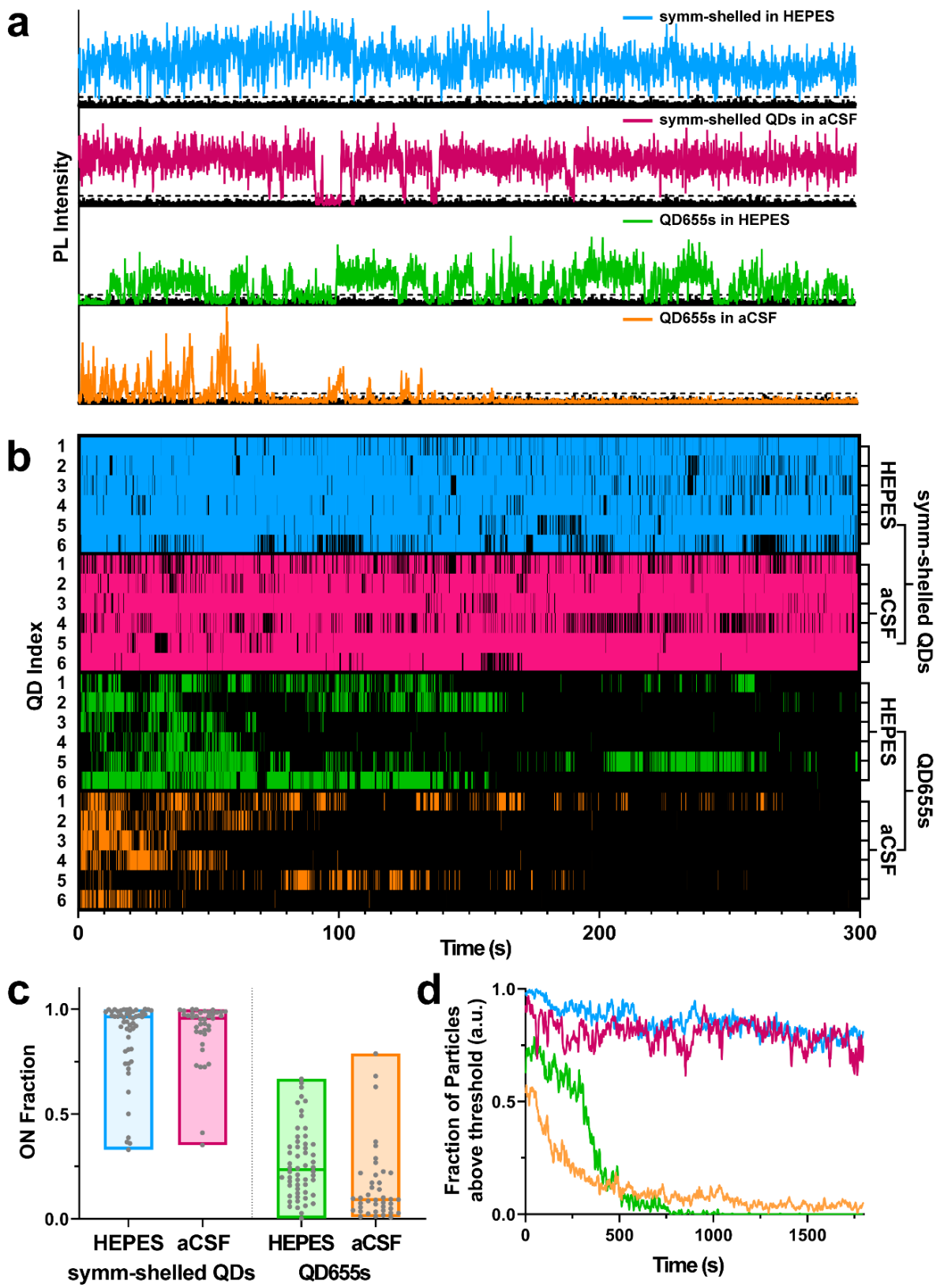


Figure 4.3. Time series and blinking behavior of single QDs. (a) Representative intensity trajectories for symmetrically shelled (symm-shelled) QDs and QD655s in both HEPES and oxygenated artificial cerebrospinal fluid (aCSF). (b) Subsets of blinking dynamics for symm-shelled QDs and QD655s in HEPES and aCSF. A total of 6 particles per condition were populated to display blinking behavior. Colors represent times that the particle was in the ON state. (c) Comparison of ON fraction populations under each condition ($N \geq 40$ QDs). (d) Comparison of photobleaching profiles for symm-shelled QDs vs. QD655s under each condition ($N > 40$ QDs).

additionally increases the number of available trap sites and further enhances blinking, concomitant with the shortening of the PL lifetimes observed for QD655s in ensemble.

To further investigate the photophysical properties of the two QD types under imaging conditions in brain slices, we examined the photobleaching behavior of the samples over 30 minutes under continuous photo-illumination. Using the same microscope and imaging parameters as the blinking analysis but increasing the bin time from 100 ms to 1 s, we compared the intensity traces of single QDs incubated in oxygenated cerebrospinal fluid *versus* control HEPES buffer. For the symmetrically shelled QDs, the majority of particles remain emissive (Figure 4.3d) in both HEPES (80%) and oxygenated cerebrospinal fluid (78%) over the course of 30 minutes, whereas nearly all QD655 particles completely photobleach during the first ~ 8 minutes of the experiment. Intriguingly, a small fraction ($< 5\%$) of QD655s remain luminescent in oxygenated cerebrospinal fluid, but completely bleach in HEPES, exhibiting no additional decline over the measured time. A similar effect has been observed in studies of O_2 sensing⁵³ and highlights the possibility that a small fraction of QDs are sufficiently passivated. Nonetheless, the degrees of depreciation in ON-fractions and photostability are pronounced in QD655 populations, which imposes major experimental limitations for single particle brain slice imaging. Taken together, the blinking and photobleaching studies suggest our symmetrically shelled QDs should provide superior photon

output under brain slice imaging conditions and should enable the capture of membrane diffusion dynamics of neuronal proteins with higher fidelity over extended periods of time compared to QD655s.

4.2.4 Imaging Ligand-conjugated SPT Probes in Acute Brain Slices

Acute brain slices are prepared such that slices undergo little change in physiological conditions (e.g. pH, oxygen concentration, glucose levels) from the time of dissection to image acquisition at the microscope (Figure 4.4a). During this time prior to mounting samples to the microscope stage, specimens are incubated with QDs diluted in oxygenated cerebrospinal fluid, allowing for fluorophores to reach depths of interest. Taking into account the ensemble and single particle characterizations included in this study, we propose the use of QDs with the symmetrically shelled composition reported here will greatly facilitate practical single target imaging in living brain tissue. Since the onset of any environmental effects on QD655s occurs at the exchange into oxygenated cerebrospinal fluid, we expect fluorescence to diminish mostly by the time of brain slice incubation (Figure 4.4b). Thus, imaging QDs in acute brain slices is dependent on the fate of emission efficiency in cerebrospinal fluid.

Using a simple spinning-disk confocal microscope and a dedicated 405 nm continuous-wave excitation source, we observed the symmetrically shelled QDs are detectable 50 μm deep in a brain slice (Figure 4.5). Prior to imaging, these QDs were PEGylated and conjugated with IDT725 (Figure 4.5a), which is furnished with a terminal cocaine analog previously used to label DAT proteins.⁵⁴ Accordingly, imaging was performed on striatal regions known to be rich in available DAT proteins. To show QD localization with SBRs suitable for tracking experiments

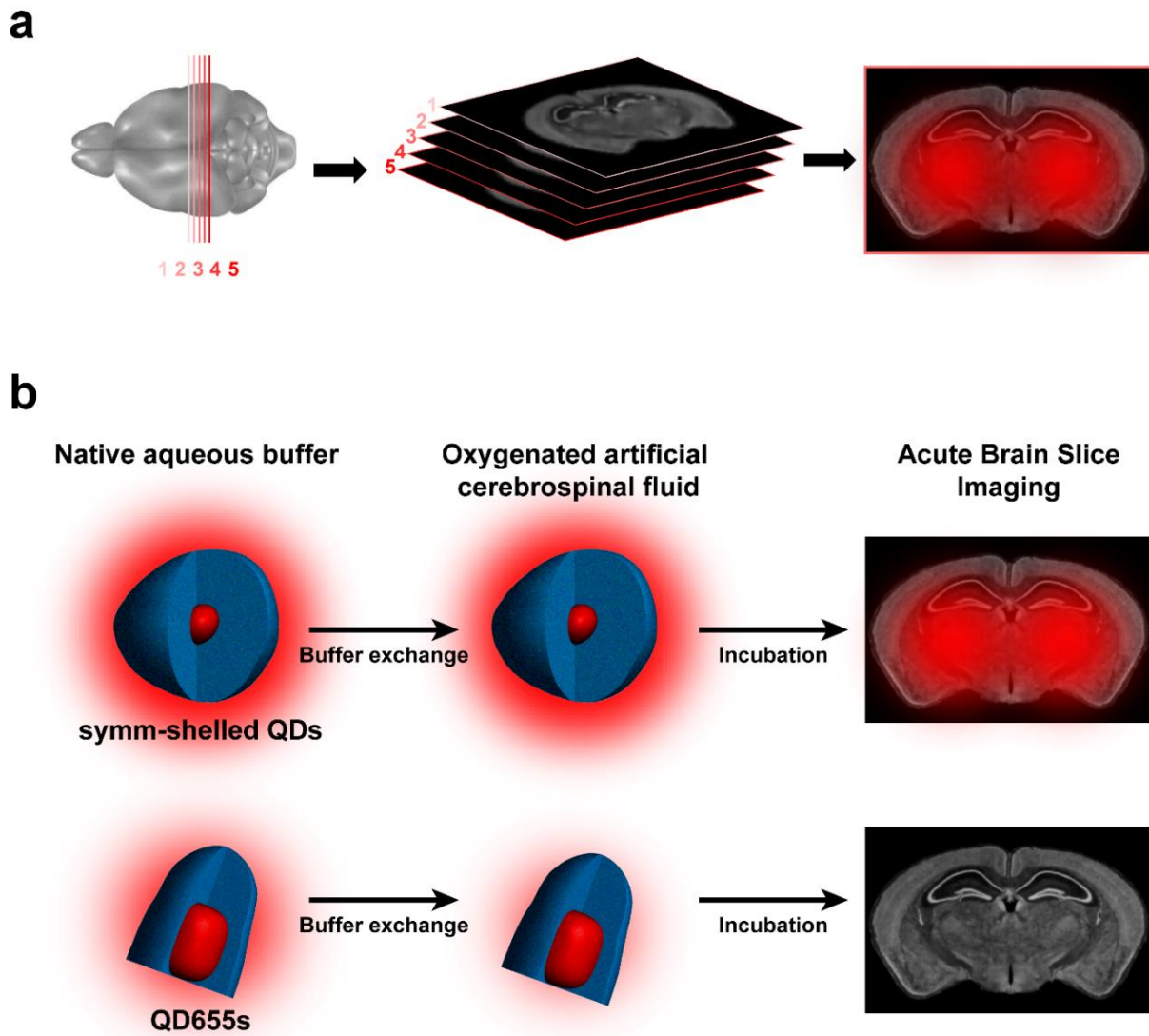


Figure 4.4. (a) Acute brain slice imaging with CdSe/CdS QDs. Mouse brain slices (1–5 300 μm slices) are cut by vibratome and incubated with ligand-conjugated QDs prior to imaging. (b) Schemes outlining buffer exchange of QDs (drawn to scale) into brain slice media (oxygenated artificial cerebrospinal fluid, aCSF) for symmetrically shelled QDs and commercial QD655s. The schemes illustrate comparison of symmetrically shelled QD and QD655 performance in oxygenated aCSF and their photoluminescence fate in tissue specimens. The auras surrounding QD structures illustrate relative photoluminescence and the fate of diminished performance of QD655 in slice media. Whole brain slice representations are provided by the Allen Institute.⁴⁴

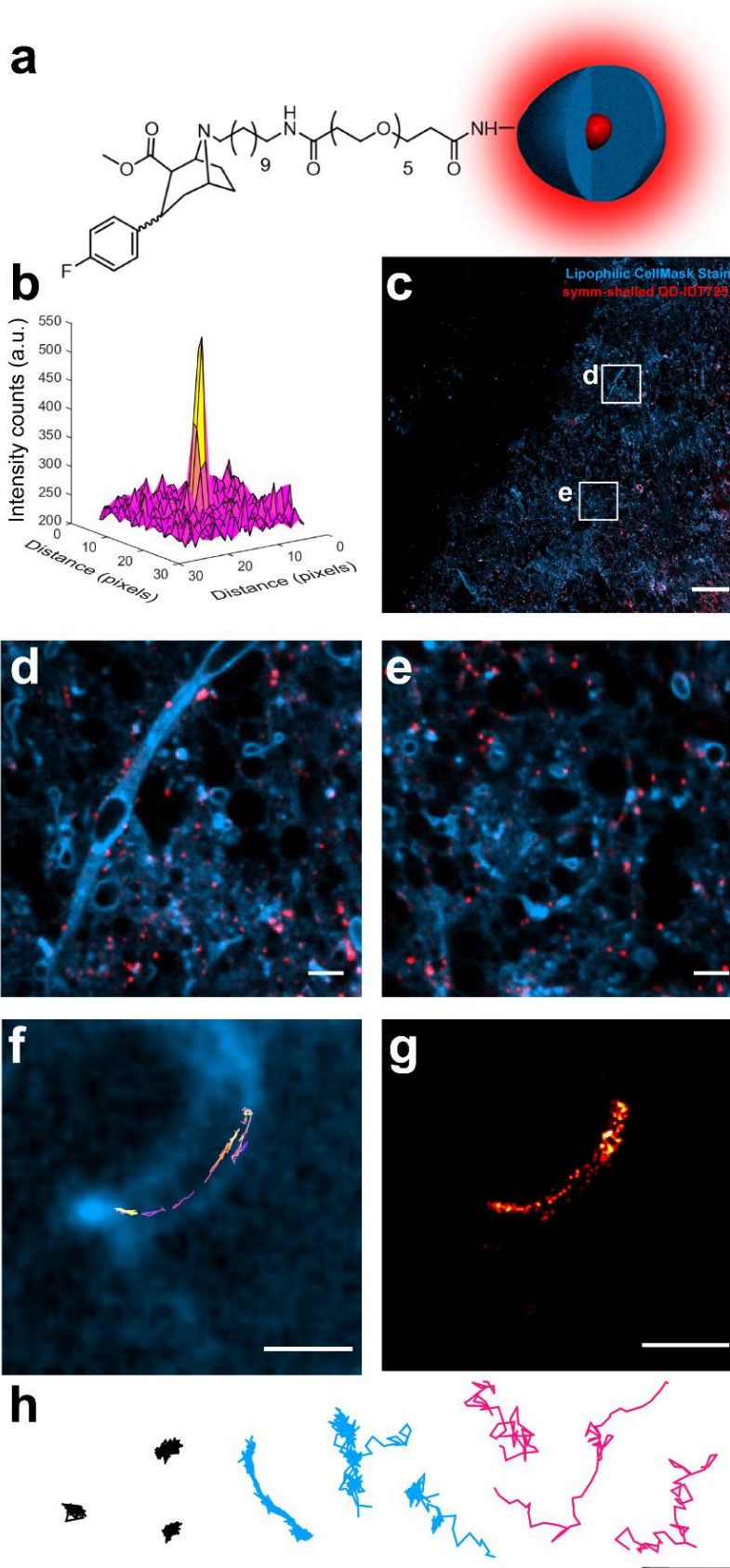


Figure 4.5. Detection and tracking analysis of QD probes in acute brain slices. (a) Structure of symmetrically shelled (symm-shelled) QD-IDT725 conjugate (not to scale). (b) Surface plot of a QD point spread function imaged 50 μm into a live brain slice. (c) Stitched image of symm-shelled QD conjugates dispersed in a brain tissue (scale bar = 50 μm). (d and e) 10 \times magnification of various regions captured in the stitched image in panel c (scale bar = 5 μm). (f) QD trajectory with non-Brownian diffusion dynamics along a neuron 50 μm into the slice (scale bar = 2 μm). (g) Localization map of the QD trajectory in panel e (scale bar = 2 μm). (h) Representative trajectories displaying diffusion of immobilized (black), neuron-bound (blue), and unbound (magenta) symm-shelled QD conjugates (scale bar = 2 μm). All images and tracking data were collected in striatal brain slices incubating in oxygenated aCSF. Lipophilic CellMask stain was used to outline the cell morphology.

(Figure 4.5b), 25 images (255,025 μm^2) of the QDs dispersed in a striatal slice were stitched together with a 100 ms exposure time for each image acquired (Figure 4.5c). Studies that include brain slice imaging typically outline network morphology by using genetic expression of fluorescent proteins, which only display a small fraction of neurons.^{55,56} To illuminate the whole slice, a lipophilic stain was used to outline the complex morphologies of a native neuronal architecture. Figure 4.5d shows that the QDs can be detected along axonal regions of neurons as well as regions that lie just outside of focal plane (Figure 4.5d,e). Excitingly, time series on the order of minutes were acquired such that we could generate high quality trajectories of QDs along a neuron at focal planes reaching 50 μm into brain tissue (Figure 4.5f). The localization map provides detailed hot spots where the QDs show extended residence times during the course of the tracking experiment (Figure 4.5g). A challenge to overcome in these experiments is washing unbound QDs from the slice. To circumvent this, QD diffusion patterns were characterized in accordance to the physical nature (Figure 4.5h), whereby immobilized and unbound diffusion patterns are filtered from trajectory sets with anomalous diffusion characteristic of QDs specifically bound to the respective target.

Given the photostability and photon output requirements of SPT analysis, QD655s have been used in the few examples of SPT in acute brain slices reported, rather than organic or protein-based fluorophores.^{29,30} For example, antibody-conjugated QD655s have been successful in imaging organotypic slices at depth with multi-photon imaging,²⁹ although organotypic slices do not require oxygenated cerebrospinal fluid. One example of SPT in acute brain slices incubated in oxygenated cerebrospinal fluid show successful detection of QD655s, but trajectories generated in these studies are limited to under 30 seconds.³⁰ The limited number of reports is likely a result of the difficulty in overcoming the O₂-dependent instability of conventional QDs. Since more than 80% of the QDs are photobleached 10 minutes after exchange into brain slice media (Figure 4.3), and a subpopulation (~8%) of QDs are expected to be non-emissive prior to excitation,³⁴ the possibility of crowding the tissue sample with undetectable QDs should be of concern. In this regard, the images (Figure 4.5) display QD dispersal that accurately represents the concentration of QDs used in our imaging experiments.

It is important to consider that Cd-containing QDs can induce dose-dependent cytotoxicity.⁵⁷ The QDs in this study are passivated with oleic acid and encapsulated within a PEGylated amphiphilic polymer layer, which forms a low dielectric layer that limits escape of metal ions.³³ Toxicology studies have shown that addition of PEG compounds to QD surfaces significantly reduces cytotoxicity effects.⁵⁸⁻⁶⁰ Our labeling concentration is far below concentrations that induce any considerable cytotoxicity seen for PEGylated CdSe/CdS QDs in *ex vivo* slices,⁶⁰ and we observe no apparent toxicity on live slices based on neuronal function. Additional experiments are needed to determine precise toxicity levels for our symmetrically shelled QDs.

4.3 Conclusions

This work introduced QD probes tailored for dynamic imaging of protein targets in native brain tissue. With ensemble and single-particle analysis, we compared QD performances in oxygenated brain slice media. Our findings show commercially available QDs are prone to fouling due to asymmetric shell coverage. On the other hand, our thick symmetrically shelled QDs feature superior photon output that is resilient to oxygenated cerebrospinal fluid. We conclude that not just shell thickness, but *geometry* of QD shells impact performance in physiologically relevant environments. Moreover, the effects of these architectural differences are silent in classic UV-visible/PL analysis. The considerations we reported here can be applied to all QD imaging platforms that involve chemically challenging systems. With our ligand-conjugated QD constructs, we also show that neuronal proteins can be imaged at the nanoscale for long time periods in live brain tissue. This is the critical step forward for future pursuits investigating molecular underpinnings of neurological diseases.

4.4 References

1. Patterson, G., Davidson, M., Manley, S., and Lippincott-Schwartz, J., Superresolution imaging using single-molecule localization, *Annu. Rev. Phys. Chem.*, **2010**, 61, 345–367.
2. Liu, Z., Lavis, L. D., and Betzig, E., Imaging live-cell dynamics and structure at the single-molecule level, *Mol. Cell*, **2015**, 58, 644–659.
3. Choquet, D. and Triller, A., The dynamic synapse, *Neuron*, **2013**, 80, 691–703.
4. Triller, A. and Choquet, D., New concepts in synaptic biology derived from single-molecule imaging, *Neuron*, **2008**, 59, 359–374.
5. Dahan, M., Lévi, S., Luccardini, C., Rostaing, P., Riveau, B., and Triller, A., Diffusion dynamics of glycine receptors revealed by single-quantum dot tracking, *Science*, **2003**, 302, 442–445.

6. Bouzigues, C., Morel, M., Triller, A., and Dahan, M., Asymmetric redistribution of GABA receptors during GABA gradient sensing by nerve growth cones analyzed by single quantum dot imaging, *Proc. Natl. Acad. Sci. U. S. A.*, **2007**, 104, 11251–11256.
7. Jézéquel, J., Johansson, E. M., Dupuis, J. P., Rogemond, V., Gréa, H., Kellermayer, B., Hamdani, N., Le Guen, E., Rabu, C., Lepleux, M., Spatola, M., Mathias, E., Bouchet, D., Ramsey, A. J., Yolken, R. H., Tamouza, R., Dalmau, J., Honnorat, J., Leboyer, M., and Groc, L., Dynamic disorganization of synaptic NMDA receptors triggered by autoantibodies from psychotic patients, *Nat. Commun.*, **2017**, 8, 1791.
8. Cai, E., Ge, P., Lee, S. H., Jeyifous, O., Wang, Y., Liu, Y., Wilson, K. M., Lim, S. J., Baird, M. A., Stone, J. E., Lee, K. Y., Davidson, M. W., Chung, H. J., Schulten, K., Smith, A. M., Green, W. N., and Selvin, P. R., Stable small quantum dots for synaptic receptor tracking on live neurons, *Angew. Chem., Int. Ed.*, **2014**, 53, 12484–12488.
9. Lee, S. H., Le, P., Youn, Y., Smith, A. M., and Selvin, P. R., The Position and Dynamics of Glutamate Receptors Measured by Brightness- and Size-Equalized Small Quantum Dots, *Biophys. J.*, **2018**, 114, 668a.
10. Kawashima, N., Nakayama, K., Itoh, K., Itoh, T., Ishikawa, M., and Biju, V., Reversible Dimerization of EGFR Revealed by Single-Molecule Fluorescence Imaging Using Quantum Dots, *Chemistry*, **2010**, 16, 1186–1192.
11. Freed, D. M., Bessman, N. J., Kiyatkin, A., Salazar-Cavazos, E., Byrne, P. O., Moore, J. O., Valley, C. C., Ferguson, K. M., Leahy, D. J., Lidke, D. S., and Lemmon, M. A., EGFR Ligands Differentially Stabilize Receptor Dimers to Specify Signaling Kinetics, *Cell*, **2017**, 171, 683–695.e18.
12. Lidke, D. S., Lidke, K. A., Rieger, B., Jovin, T. M., and Arndt-Jovin, D. J., Reaching out for signals: filopodia sense EGF and respond by directed retrograde transport of activated receptors, *J. Cell Biol.*, **2005**, 170, 619–626.
13. Yanagawa, M., Hiroshima, M., Togashi, Y., Abe, M., Yamashita, T., Shichida, Y., Murata, M., Ueda, M., and Sako, Y., Single-molecule diffusion-based estimation of ligand effects on G protein-coupled receptors, *Sci. Signaling*, **2018**, 11, eaao1917.
14. Rosenthal, S. J., Tomlinson, I., Adkins, E. M., Schroeter, S., Adams, S., Swafford, L., McBride, J., Wang, Y., DeFelice, L. J., and Blakely, R. D., Targeting Cell Surface Receptors with Ligand-Conjugated Nanocrystals, *J. Am. Chem. Soc.*, **2002**, 124, 4586–4594.
15. Kovtun, O., Tomlinson, I. D., Sakrikar, D. S., Chang, J. C., Blakely, R. D., and Rosenthal, S. J., Visualization of the Cocaine-Sensitive Dopamine Transporter with Ligand-Conjugated Quantum Dots, *ACS Chem. Neurosci.*, **2011**, 2, 370–378.
16. Chang, J. C., Tomlinson, I. D., Warnement, M. R., Ustione, A., Carneiro, A. M. D., Piston, D. W., Blakely, R. D., and Rosenthal, S. J., Single molecule analysis of serotonin transporter

regulation using antagonist-conjugated quantum dots reveals restricted, p38 MAPK-Dependent mobilization underlying uptake activation, *J. Neurosci.*, **2012**, 32, 8919–8929.

17. Kovtun, O., Sakrikar, D., Tomlinson, I. D., Chang, J. C., Arzeta-Ferrer, X., Blakely, R. D., and Rosenthal, S. J., Single-quantum-dot tracking reveals altered membrane dynamics of an attention-deficit/hyperactivity-disorder-derived dopamine transporter coding variant, *ACS Chem. Neurosci.*, **2015**, 6, 526–534.

18. Bailey, D. M., Catron, M. A., Kovtun, O., Macdonald, R. L., Zhang, Q., and Rosenthal, S. J., Single Quantum Dot Tracking Reveals Serotonin Transporter Diffusion Dynamics are Correlated with Cholesterol-Sensitive Threonine 276 Phosphorylation Status in Primary Midbrain Neurons, *ACS Chem. Neurosci.*, **2018**, 9, 2534–2541.

19. Thal, L. B., Tomlinson, I. D., Quinlan, M. A., Kovtun, O., Blakely, R. D., and Rosenthal, S. J., Single Quantum Dot Imaging Reveals PKC β -Dependent Alterations in Membrane Diffusion and Clustering of an Attention-Deficit Hyperactivity Disorder/Autism/Bipolar Disorder-Associated Dopamine Transporter Variant, *ACS Chem. Neurosci.*, **2019**, 10, 460–471.

20. Rosenthal, S. J., Nanotechnology in Neuroscience Reveals Membrane Mobility Matters, *ACS Chem. Neurosci.*, **2019**, 10, 30–32.

21. Thal, L. B., Bailey, D. M., Kovtun, O., and Rosenthal, S. J., Quantum Dot Toolbox in Membrane Neurotransmitter Transporter Research, in *Chemical and Synthetic Approaches in Membrane Biology*, Ed. A. K. Shukla, Springer New York, New York, NY, **2017**, pp. 219–230.

22. Ji, N., Magee, J. C., and Betzig, E., High-speed, low-photodamage nonlinear imaging using passive pulse splitters, *Nat. Methods*, **2008**, 5, 197–202.

23. Laissue, P. P., Alghamdi, R. A., Tomancak, P., Reynaud, E. G., and Shroff, H., Assessing phototoxicity in live fluorescence imaging, *Nat. Methods*, **2017**, 14, 657–661.

24. Wichner, S. M., Mann, V. R., Powers, A. S., Segal, M. A., Mir, M., Bandaria, J. N., DeWitt, M. A., Darzacq, X., Yildiz, A., and Cohen, B. E., Covalent Protein Labeling and Improved Single-Molecule Optical Properties of Aqueous CdSe/CdS Quantum Dots, *ACS Nano*, **2017**, 11, 6773–6781.

25. Rosenthal, S. J., Chang, J. C., Kovtun, O., McBride, J. R., and Tomlinson, I. D., Biocompatible quantum dots for biological applications, *Chem. Biol.*, **2011**, 18, 10–24.

26. Larson, D. R., Zipfel, W. R., Williams, R. M., Clark, S. W., Bruchez, M. P., Wise, F. W., and Webb, W. W., Water-soluble quantum dots for multiphoton fluorescence imaging in vivo, *Science*, **2003**, 300, 1434–1436.

27. So, M. K., Xu, C., Loening, A. M., Gambhir, S. S., and Rao, J., Self-illuminating quantum dot conjugates for in vivo imaging, *Nat. Biotechnol.*, **2006**, 24, 339–343.

28. Orndorff, R. L., Warnement, M. R., Mason, J. N., Blakely, R. D., and Rosenthal, S. J., Quantum Dot Ex Vivo Labeling of Neuromuscular Synapses, *Nano Lett.*, **2008**, 8, 780–785.
29. Biermann, B., Sokoll, S., Klueva, J., Missler, M., Wiegert, J., Sibarita, J. B., and Heine, M., Imaging of molecular surface dynamics in brain slices using single-particle tracking, *Nat. Commun.*, **2014**, 5, 3024.
30. Varela, J. A., Dupuis, J. P., Etchepare, L., Espana, A., Cognet, L., and Groc, L., Targeting neurotransmitter receptors with nanoparticles in vivo allows single-molecule tracking in acute brain slices, *Nat. Commun.*, **2016**, 7, 10947.
31. Varela, J. A., Ferreira, J. S., Dupuis, J. P., Durand, P., Bouchet-Tessier, D., and Groc, L., Single nanoparticle tracking of N-methyl-D-aspartate receptors in cultured and intact brain tissue, *Neurophotonics*, **2016**, 3, 041808.
32. Chen, O., Zhao, J., Chauhan, V. P., Cui, J., Wong, C., Harris, D. K., Wei, H., Han, H. S., Fukumura, D., Jain, R. K., and Bawendi, M. G., Compact high-quality CdSe-CdS core-shell nanocrystals with narrow emission linewidths and suppressed blinking, *Nat. Mater.*, **2013**, 12, 445–451.
33. Mann, V. R., Powers, A. S., Tilley, D. C., Sack, J. T., and Cohen, B. E., Azide-Alkyne Click Conjugation on Quantum Dots by Selective Copper Coordination, *ACS Nano*, **2018**, 12, 4469–4477.
34. Orfield, N. J., McBride, J. R., Keene, J. D., Davis, L. M., and Rosenthal, S. J., Correlation of atomic structure and photoluminescence of the same quantum dot: pinpointing surface and internal defects that inhibit photoluminescence, *ACS Nano*, **2015**, 9, 831–839.
35. van Embden, J., Jasieniak, J., and Mulvaney, P., Mapping the Optical Properties of CdSe/CdS Heterostructure Nanocrystals: The Effects of Core Size and Shell Thickness, *J. Am. Chem. Soc.*, **2009**, 131, 14299–14309.
36. Chen, Y., Vela, J., Htoon, H., Casson, J. L., Werder, D. J., Bussian, D. A., Klimov, V. I., and Hollingsworth, J. A., "Giant" multishell CdSe nanocrystal quantum dots with suppressed blinking, *J. Am. Chem. Soc.*, **2008**, 130, 5026–5027.
37. Orfield, N. J., McBride, J. R., Wang, F., Buck, M. R., Keene, J. D., Reid, K. R., Htoon, H., Hollingsworth, J. A., and Rosenthal, S. J., Quantum yield heterogeneity among single nonblinking quantum dots revealed by atomic structure-quantum optics correlation, *ACS Nano*, **2016**, 10, 1960–1968.
38. McBride, J., Treadway, J., Feldman, L. C., Pennycook, S. J., and Rosenthal, S. J., Structural basis for near unity quantum yield core/shell nanostructures, *Nano Lett.*, **2006**, 6, 1496–1501.
39. Reid, K. R., McBride, J. R., Freymeyer, N. J., Thal, L. B., and Rosenthal, S. J., Chemical Structure, Ensemble and Single-Particle Spectroscopy of Thick-Shell InP–ZnSe Quantum Dots,

Nano Lett., **2018**, 18, 709–716.

40. Qdot Nanocrystals – Section 6.6, <https://www.thermofisher.com/us/en/home/references/molecular-probes-the-handbook/ultrasensitive-detection-technology/qdot-nanocrystal-technology.html>.

41. van Sark, W. G. J. H. M., Frederix, P. L. T. M., Van den Heuvel, D. J., Gerritsen, H. C., Bol, A. A., van Lingen, J. N. J., de Mello Donegá, C., and Meijerink, A., Photooxidation and Photobleaching of Single CdSe/ZnS Quantum Dots Probed by Room-Temperature Time-Resolved Spectroscopy, *J. Phys. Chem. B*, **2001**, 105, 8281–8284.

42. van Sark, W. G. J. H. M., Frederix, P. L. T. M., Bol, A. A., Gerritsen, H. C., and Meijerink, A., Blueing, Bleaching, and Blinking of Single CdSe/ZnS Quantum Dots, *ChemPhysChem*, **2002**, 3, 871–879.

43. Lee, S. F. and Osborne, M. A., Brightening, Blinking, Bluing and Bleaching in the Life of a Quantum Dot: Friend or Foe?, *ChemPhysChem*, **2009**, 10, 2174–2191.

44. Lein, E. S., Hawrylycz, M. J., Ao, N., Ayres, M., Bensinger, A., Bernard, A., Boe, A. F., Boguski, M. S., Brockway, K. S., Byrnes, E. J., Chen, L., Chen, L., Chen, T. M., Chi Chin, M., Chong, J., Crook, B. E., Czaplinska, A., Dang, C. N., Datta, S., Dee, N. R., Desaki, A. L., Desta, T., Diep, E., Dolbeare, T. A., Donelan, M. J., Dong, H. W., Dougherty, J. G., Duncan, B. J., Ebbert, A. J., Eichele, G., Estin, L. K., Faber, C., Facer, B. A., Fields, R., Fischer, S. R., Fliss, T. P., Frensley, C., Gates, S. N., Glattfelder, K. J., Halverson, K. R., Hart, M. R., Hohmann, J. G., Howell, M. P., Jeung, D. P., Johnson, R. A., Karr, P. T., Kawal, R., Kidney, J. M., Knapik, R. H., Kuan, C. L., Lake, J. H., Laramee, A. R., Larsen, K. D., Lau, C., Lemon, T. A., Liang, A. J., Liu, Y., Luong, L. T., Michaels, J., Morgan, J. J., Morgan, R. J., Mortrud, M. T., Mosqueda, N. F., Ng, L. L., Ng, R., Orta, G. J., Overly, C. C., Pak, T. H., Parry, S. E., Pathak, S. D., Pearson, O. C., Puchalski, R. B., Riley, Z. L., Rockett, H. R., Rowland, S. A., Royall, J. J., Ruiz, M. J., Sarno, N. R., Schaffnit, K., Shapovalova, N. V., Sivisay, T., Slaughterbeck, C. R., Smith, S. C., Smith, K. A., Smith, B. I., Sodt, A. J., Stewart, N. N., Stumpf, K. R., Sunkin, S. M., Sutram, M., Tam, A., Teemer, C. D., Thaller, C., Thompson, C. L., Varnam, L. R., Visel, A., Whitlock, R. M., Wohnoutka, P. E., Wolkey, C. K., Wong, V. Y., Wood, M., Yaylaoglu, M. B., Young, R. C., Youngstrom, B. L., Yuan, X.F., Zhang, B., Zwingman, T. A., and Jones, A. R., Genome-wide atlas of gene expression in the adult mouse brain, *Nature*, **2006**, 445, 168–176.

45. Ho, J., Tumkaya, T., Aryal, S., Choi, H., and Claridge-Chang, A., Moving beyond P values: data analysis with estimation graphics, *Nat. Methods*, **2019**, 16, 565–566.

46. Efros, A. L. and Rosen, M., Random telegraph signal in the photoluminescence intensity of a single quantum dot, *Phys. Rev. Lett.*, **1997**, 78, 1110–1113.

47. Frantsuzov, P. A., Volkán-Kacsó, S., and Jankó, B., Model of fluorescence intermittency of single colloidal semiconductor quantum dots using multiple recombination centers, *Phys. Rev. Lett.*, **2009**, 103, 207402.

48. Qin, W. and Guyot-Sionnest, P., Evidence for the role of holes in blinking: negative and oxidized CdSe/CdS dots, *ACS Nano*, **2012**, 6, 9125– 9132.
49. Lim, S. J., Ma, L., Schleife, A., and Smith, A. M., Coord. Quantum dot surface engineering: toward inert fluorophores with compact size and bright, stable emission, *Chem. Rev.*, **2016**, 320–321, 216–237.
50. Talapin, D. V., Nelson, J. H., Shevchenko, E. V., Aloni, S., Sadtler, B., and Alivisatos, A. P., Seeded growth of highly luminescent CdSe/CdS nanoheterostructures with rod and tetrapod morphologies, *Nano Lett.*, **2007**, 7, 2951– 2959.
51. Luo, Y. and Wang, L. W., Electronic structures of the CdSe/CdS core– shell nanorods, *ACS Nano*, **2010**, 4, 91–98.
52. Rainò, G., Stöferle, T., Moreels, I., Gomes, R., Kamal, J. S., Hens, Z., and Mahrt, R. F., Probing the wave function delocalization in CdSe/CdS dot-in-rod nanocrystals by time-and temperature-resolved spectroscopy, *ACS Nano*, **2011**, 5, 4031–4036.
53. Lorenzon, M., Christodoulou, S., Vaccaro, G., Pedrini, J., Meinardi, F., Moreels, I., and Brovelli, S., Reversed oxygen sensing using colloidal quantum wells towards highly emissive photoresponsive varnishes, *Nat. Commun.*, **2015**, 6, 6434.
54. Kovtun, O., Tomlinson, I. D., Bailey, D. M., Thal, L. B., Ross, E. J., Harris, L., Frankland, M. P., Ferguson, R. S., Glaser, Z., Greer, J., and Rosenthal, S. J., Single quantum dot tracking illuminates neuroscience at the nanoscale, *Chem. Phys. Lett.*, **2018**, 706, 741–752.
55. Feng, G., Mellor, R. H., Bernstein, M., Keller-Peck, C., Nguyen, Q. T., Wallace, M., Nerbonne, J. M., Lichtman, J. W., and Sanes, J. R., Imaging neuronal subsets in transgenic mice expressing multiple spectral variants of GFP, *Neuron*, **2000**, 28, 41–51.
56. Karra, D. and Dahm, R., Transfection techniques for neuronal cells, *J. Neurosci.*, **2010**, 30, 6171–6177.
57. Oh, E., Liu, R., Nel, A., Gemill, K. B., Bilal, M., Cohen, Y., and Medintz, I. L., Meta-analysis of cellular toxicity for cadmium-containing quantum dots, *Nat. Nanotechnol.*, **2016**, 11, 479.
58. Selim, K. M. K., Xing, Z. C., Choi, M. J., Chang, Y., Guo, H., and Kang, I. K., Reduced cytotoxicity of insulin-immobilized CdS quantum dots using PEG as a spacer, *Nanoscale Res. Lett.*, **2011**, 6, 528.
59. Clift, M. J. D., Varet, J., Hankin, S. M., Brownlee, B., Davidson, A. M., Brandenberger, C., Rothen-Rutishauser, B., Brown, D. M., and Stone, V., Quantum dot cytotoxicity in vitro: An investigation into the cytotoxic effects of a series of different surface chemistries and their core/shell materials, *Nanotoxicology*, **2011**, 5, 664– 674.
60. Zhang, M., Bishop, B. P., Thompson, N. L., Hildahl, K., Dang, B., Mironchuk, O., Chen, N.,

Aoki, R., Holmberg, V. C., and Nance, E., Quantum dot cellular uptake and toxicity in the developing brain: implications for use as imaging probes, *Nanoscale Adv.*, **2019**, 1, 3424–34.

CHAPTER V

CONCLUSION

5.1 Concluding Remarks

In this work, the advantage of teasing apart physical properties at the single molecule level, whether it be of a protein target or a nanoparticle, was demonstrated by implementing a set of experiments at the microscope. I first discussed how a ligand-conjugated QD labeling approach led us to monitor single particle membrane dynamics of dysfunctional DAT mutant derived from subjects diagnosed with ADHD, autism, and bipolar disorder (Chapter 3). This work established a biophysical profile of the protein variant using a comprehensive examination of diffusion rates and clustering propensity. Furthermore, by providing experimental results that employed pharmacological tools and amino acid substitutions, this study demonstrated alterations in DAT membrane mobility are dependent on a PKC β -mediated phosphorylation pathway. These findings suggest the possibility of a case where the disease-associated mutants mistargets membrane domains on a kinase-dependent basis, ultimately disrupting the protein function.

Chapter 4 addressed the need for single molecule imaging in physiologically relevant specimens. In this case, the critical next step to further examine DAT dynamics at the single molecule level and determine the pathological role of DAT mobility is by imaging in intact brain tissue. Imaging at the high spatiotemporal resolution needed in single particle analysis demands probes specifically designed for the chemically and physically challenging environment of brain tissue. In this work, I discovered that not only composition and thickness, but also geometry of the QD heterostructure is a critical property to control when designing probes intended for imaging in

neurophysiological environments. Using single particle analysis, I showed that a symmetric shell around the QD core is required for prolonged photophysical integrity in cerebrospinal fluid, properties that are silent in conventional ensemble experiments. Importantly, the cerebrospinal fluid required to preserve the health brain tissue is rich in O₂. The results in this chapter suggest that the most widely used commercially available QDs fail in cerebrospinal fluid because the inadequate, asymmetric shelling, which in turn evokes O₂-mediated quenching of the vulnerable QD core. Finally, this work demonstrated that symmetrically shelled QD can be detected deep in living brain slices for prolonged time periods at the single particle level.

This multimethod approach also provides an experimental framework for probe development, allowing researchers to characterize photophysical nature before progressing to animal models. Reliance on conventional methods and ensemble averaging has the potential to overlook properties necessary to produce significant findings. My dissertation emphasizes the need for investigation using single particle regimes based on fully defined probes to generate accuracy and precision in optical imaging. Through the combination of innovative QD architecture and single particle tracking, my work establishes techniques that could open doors for experiments that directly link neuronal protein mobility to the behavior of neuropsychiatric disease models.

5.2 Future Directions

5.2.1 Interplay Between DAT and Membrane Binding Partners

Exploring the interactions between DAT and other membrane binding proteins presents an ideal area for further research. It would be particularly advantageous to tease apart the interactions

of presynaptic D2 autoreceptors (D2R) and DAT. The sparse publications pertaining to their physical interactions are limited to little more than classic immunoblot and crosslinking data.¹ Perhaps the transient membrane dynamics influenced by cholesterol- or PIP₂-enriched membrane domains play an important role in intrinsic functions of the two proteins. Since transient DAT and membrane partner dynamics could be a critical missing piece, designing a two-color single particle imaging experiment is the logical next step. One important aspect of the approach is that two different orthogonal conjugation strategies will be required for a successful characterization. The Rosenthal group's recently developed biotinylated ligand would be ideal in this experiment, especially if used in combination with the symmetrically shelled QDs introduced in Chapter 4.² These amine-functionalized QDs could easily undergo EDC/NHS coupling to a carboxylic acid-terminated ligand. Once the two-color tracking protocol is established, studies could then be extended to other known membrane partners in the DAT interactome (e.g. syntaxin 1A, and kappa opioid receptors).^{3,4}

5.2.2 Linking Endogenous DAT Membrane Dynamics to Animal Model Pathology

Tracking the membrane dynamics of endogenously expressed DAT undissociated from its native neuronal environment is the next step to investigating its underpinnings in pathological behavior. To accomplish this, DAT specificity of the QD probe must be verified, which may require more sophisticated characterization given that (i) the 3D neuronal architecture is vastly different (chemically and physically) from transfected monolayer cell cultures and (ii) the difficulty in sufficiently washing unbound and non-specifically bound QDs from tissue. One possible approach entails obtaining an enrichment factor, which is the ratio of bound QDs on

fluorescent-protein-fused DAT expressing neurons to unbound QDs – similar to an SNR.⁵ Indeed, one must also verify that the conjugate is intact prior to labeling. Appendix E details a useful characterization technique to verify intact QD conjugates that utilizes surface enhanced Raman spectroscopy. Another possible tool in establishing specificity relies on the categorization of discrete QD trajectory diffusion patterns. Once verified, animal behavioral analysis can be directly correlated with DAT membrane dynamics determined after dissection. Confirmation would add DAT surface trafficking as a key determinant of neurological health and neuropsychiatric disease.

5.3 References

1. Lee, F. J., Pei, L., Moszczynska, A., Vukusic, B., Fletcher, P. J., and Liu, F., Dopamine transporter cell surface localization facilitated by a direct interaction with the dopamine D2 receptor, *EMBO J.*, **2007**, 26, 2127–2136.
2. Tomlinson, I. D., Kovtun, O., Crescentini, T. M., and Rosenthal, S. J., Biotinylated-spiperone ligands for quantum dot labeling of the dopamine D2 receptor in live cell cultures, *Bioorg. Med. Chem. Lett.*, **2019**, 29, 959-964.
3. Binda, F., Dipace, C., Bowton, E., Robertson, S. D., Lute, B. J., Fog, J. U., Zhang, M., Sen, N., Colbran, R. J., Gnegy, M. E., Gether, U., Javitch, J. A., Erreger, K., and Galli, A., Syntaxin 1A interaction with the dopamine transporter promotes amphetamine-induced dopamine efflux, *Mol. Pharmacol.*, **2008**, 74, 1101–1108.
4. Kivell, B., Uzelac, Z., Sundaramurthy, S., Rajamanickam, J., Ewald, A., Chefer, V., Jaligam, V., Bolan, E., Simonson, B., Annamalai, B., Mannangatti, P., Prisinzano, T. E., Gomes, I., Devi, L. A., Jayanthi, L. D., Sitte, H. H., Ramamoorthy, S., and Shippenberg, T. S., Salvinorin A regulates dopamine transporter function via a kappa opioid receptor and ERK1/2-dependent mechanism, *Neuropharmacology*, **2014**, 86, 228–240.
5. Biermann, B., Sokoll, S., Klueva, J., Missler, M., Wiegert, J., Sibarita, J. B., and Heine, M., Imaging of molecular surface dynamics in brain slices using single-particle tracking, *Nat. Commun.*, **2014**, 5, 3024.

APPENDIX A

**SUPPORTING INFORMATION FOR CHAPTER III: SINGLE QUANTUM DOT
IMAGING REVEALS PKC β -DEPENDENT ALTERATIONS IN MEMBRANE
DIFFUSION AND CLUSTERING OF AN ATTENTION-DEFICIT HYPERACTIVITY
DISORDER/AUTISM/BIPOLAR DISORDER-ASSOCIATED DOPAMINE
TRANSPORTER VARIANT**

Table A.1. N for each population of trajectories analyzed in both HEK-293 and SK-NMC Cells.

	<i>N (trajectories)</i>		
	HEK293	SK-N-MC	
<i>hDAT</i>	Basal	464	411
	+PMA	243	646
	+Enz	305	211
<i>hDAT A559V</i>	Basal	378	936
	+PMA	391	515
	+Enz	392	266
<i>YFPDAT</i>		465	513
<i>YFPDAT S/D</i>		411	678
<i>hDAT S53A</i>		438	-
<i>hDAT S53D</i>		414	-
<i>hDAT A559V S53A</i>		766	-
<i>hDAT A559V S53D</i>		723	-

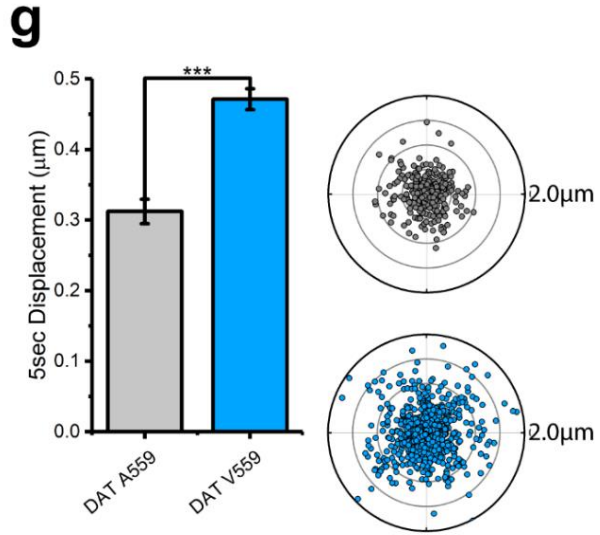
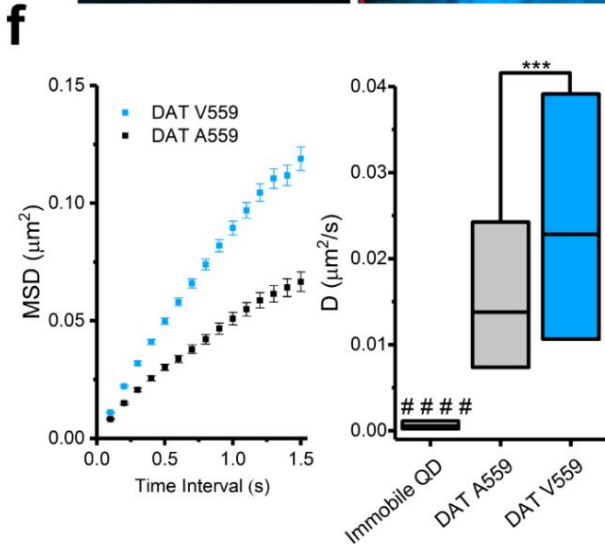
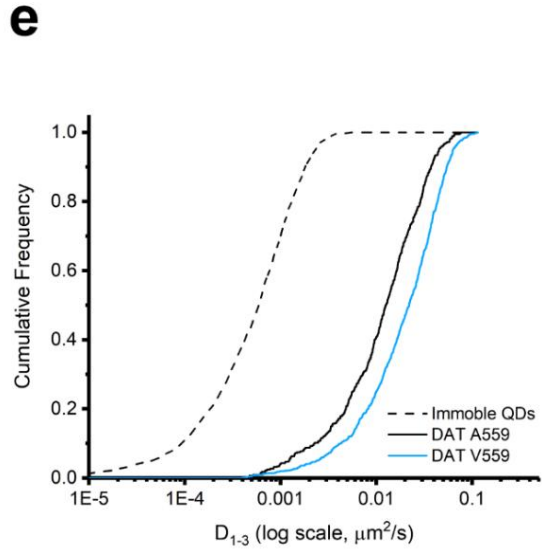
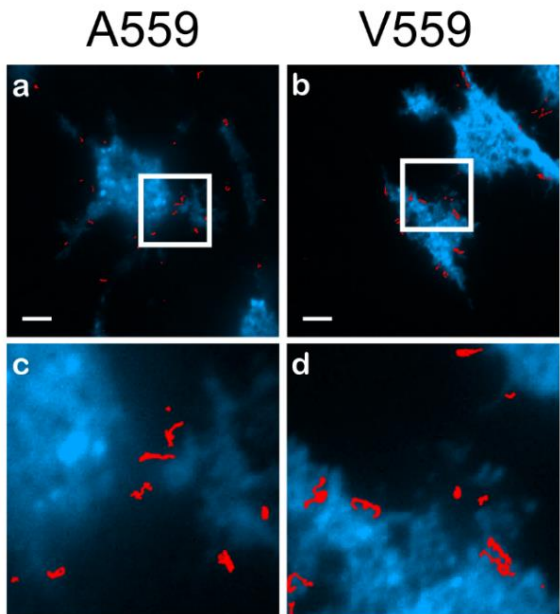


Figure A.1. DAT Val559 exhibits faster mobility compared to wild-type DAT transiently expressed in SK-N-MC cells. a,b) Representative trajectories collected over 60 s of QD-bound DAT and DAT Val559 superimposed to the IDT307 channel (scale bar = 5 μm). c,d) Images at 4x magnification of images in **a** and **b** respectively. e) Cumulative frequency distributions of diffusion coefficients (D_{1-3}) of immobile QDs, DAT Ala559, and DAT Val559. f) Averaged mean square displacement MSD plots (mean \pm S.E.M.) and diffusion coefficient box plots (median, 25% and 75% interquartiles, one-way ANOVA followed by Bonferroni's multiple comparison test, *** $p < 0.001$, #### $p < 0.001$ comparing data sets to immobilized QDs as control) of trajectories analyzed for DAT Ala559 and DAT Val559. g) 5-second displacement bar graph (mean \pm S.E.M., unpaired Student's t-test, *** $p < 0.001$) and polar plots (outer radius limit = 2 μm) of single DAT Ala559 (gray) and DAT Val559 (blue). DAT displacements are normalized to their spatial origin. N (trajectories) are provided in Table A.1.

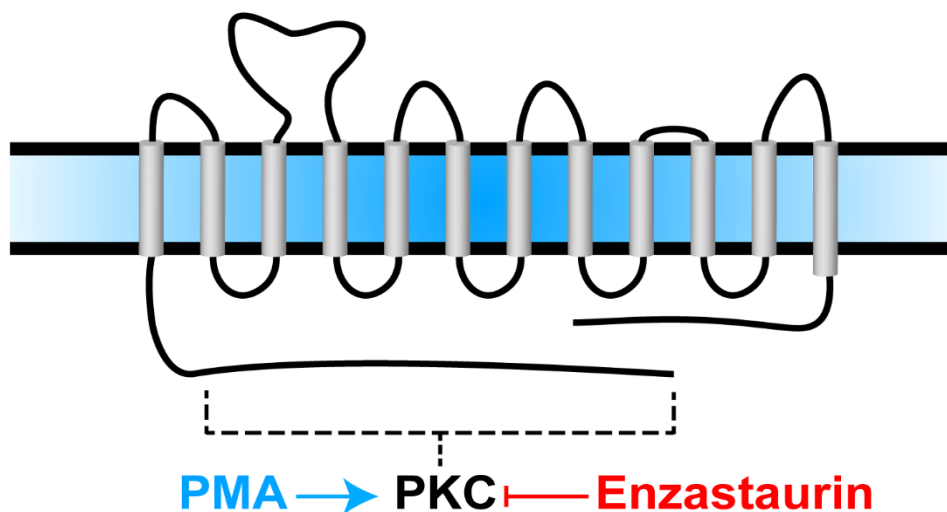
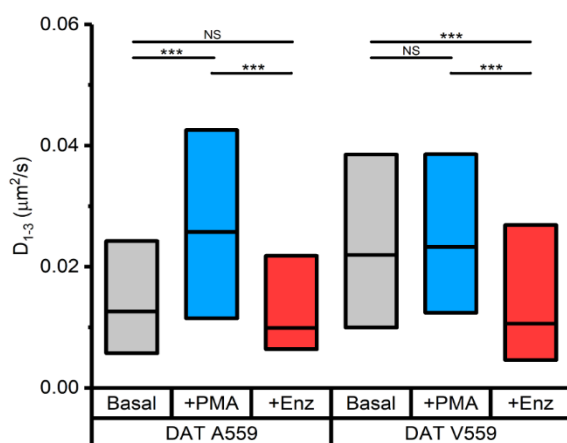
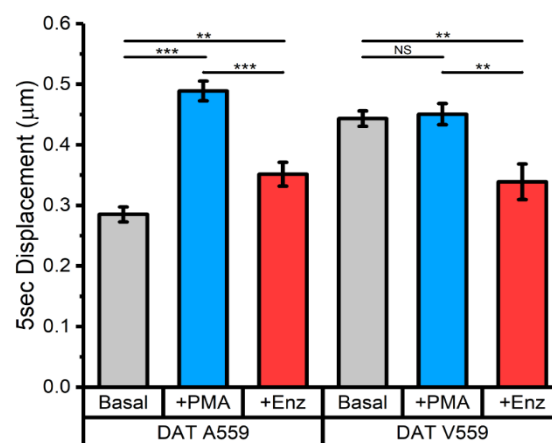
a**b****c**

Figure A.2. DAT Val559 diffusion is unresponsive to protein kinase C (PKC) activation and attenuated by PKC β inhibition in SK-N-MC cells. a) Schematic of DAT with PKC activation by PMA highlighted in blue and PKC β inhibition by enzastaurin (Enz) highlighted in red. The dashed line denotes the general region of phosphorylation mediated by PKC activation. b) Diffusion coefficient box plot (median, 25% and 75% interquartiles, one-way ANOVA followed by Bonferroni's multiple comparison test, *** p <0.001) of trajectories analyzed for DAT Ala559 and DAT Val559 under basal, stimulated (+PMA) conditions, and inhibited (+Enz) conditions. c) 5-second displacement bar graph (mean \pm S.E.M., unpaired Student's t -test, ** p <0.01, *** p <0.001) of trajectories analyzed for DAT Ala559 and DAT Val559 under basal, stimulated (+PMA), and inhibited (+Enz) conditions. N (trajectories) are provided in Table A.1.

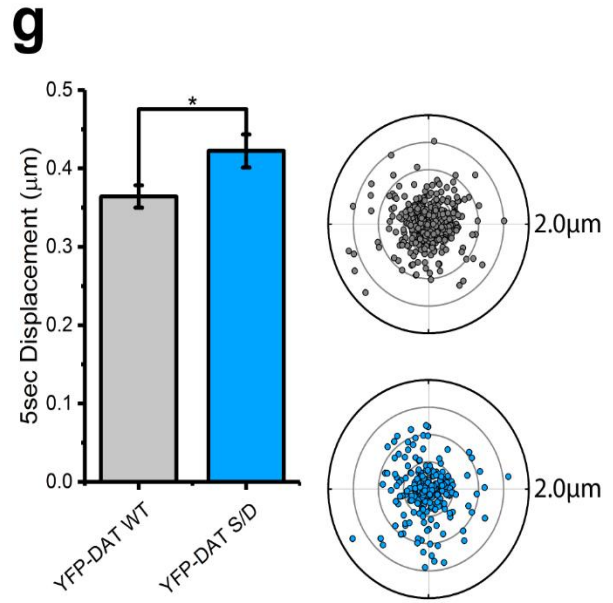
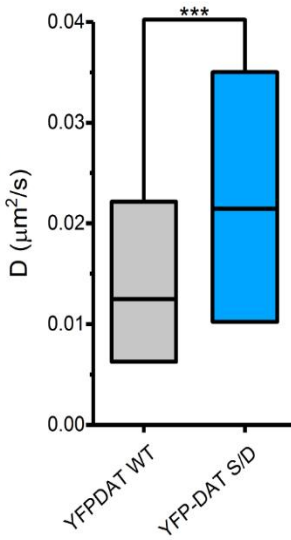
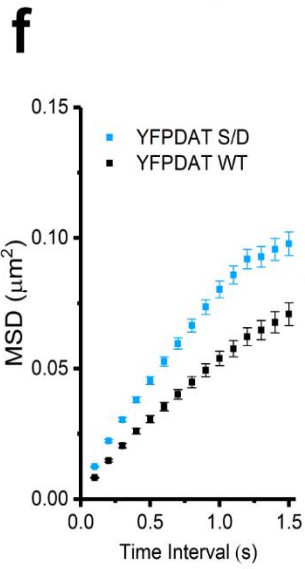
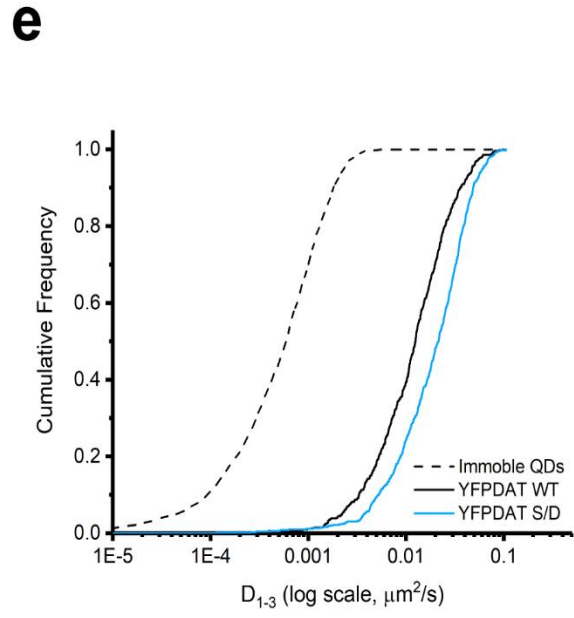
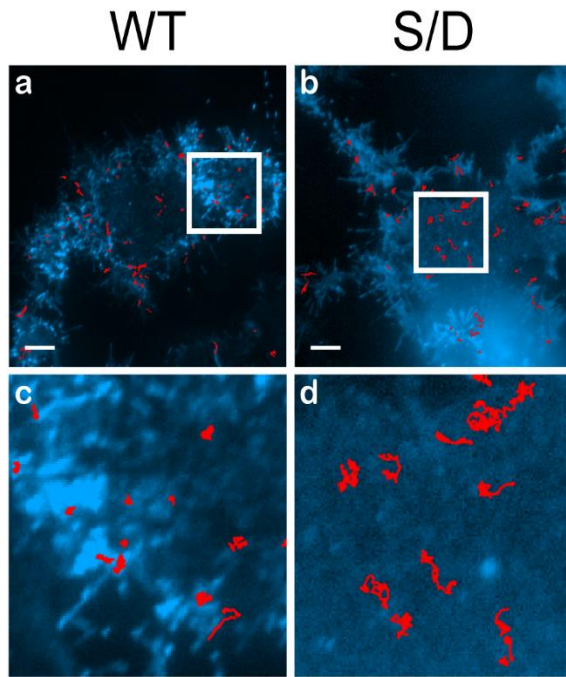


Figure A.3. Phosphomimetic YFP-DAT S/D exhibits faster membrane mobility than wild-type YFP-DAT in SK-N-MC cells. a,b) Representative trajectories collected over 60 s of QD-bound YFP-DAT WT and YFP-DAT S/D superimposed to cell membranes outlined by YFP (scale bar = 5 μm). c,d) Images at 4x magnification of images in **a** and **b** respectively. e) Cumulative frequency distributions of diffusion coefficients (D_{1-3}) of immobile QDs, YFP-DAT WT, and YFP-DAT S/D. f) Averaged mean square displacement MSD plots (mean \pm S.E.M.) and a diffusion coefficient box plot (median, 25% and 75% interquartiles, one-way ANOVA followed by Bonferroni's multiple comparison test, *** $p < 0.001$) of trajectories analyzed for YFP-DAT WT and YFP-DAT S/D. g) 5-second displacement bar graph (mean \pm S.E.M., Student's t-test, * $p < 0.05$) and polar plots (outer radius limit = 2 μm) of single YFP-DAT WT (gray) and YFP-DAT S/D (blue). DAT-QD displacements are normalized to their spatial origin. N (trajectories) are provided in Table A.1.

APPENDIX B

SUPPORTING INFORMATION FOR CHAPTER IV: LIGAND-CONJUGATED QUANTUM DOTS FOR FAST SUB-DIFFRACTION PROTEIN TRACKING IN ACUTE BRAIN SLICES

Table B.1. Time-resolved PL lifetimes and relative amplitudes of (c) QD655s and (d) symmetrically shelled (symm-shelled) CdSe/CdS QDs.

Sample	τ_1 (ns)	A_1	τ_2 (ns)	A_2	τ_3 (ns)	A_3	τ_{avg}
QD655s in HEPES	3.7 ± 0.3	0.17	21.3 ± 0.5	0.49	47.1 ± 0.5	0.34	27.0 ± 0.2
QD655s in aCSF	4.9 ± 0.4	0.19	19.4 ± 0.5	0.56	42.3 ± 0.6	0.25	22.4 ± 0.1
symm-shelled QDs in HEPES	6.4 ± 0.5	0.15	38.3 ± 0.9	0.59	88.1 ± 1.7	0.26	46.8 ± 0.2
Symm-shelled in aCSF	6.6 ± 0.6	0.13	87.2 ± 1.6	0.28	37.4 ± 0.9	0.59	47.7 ± 0.2

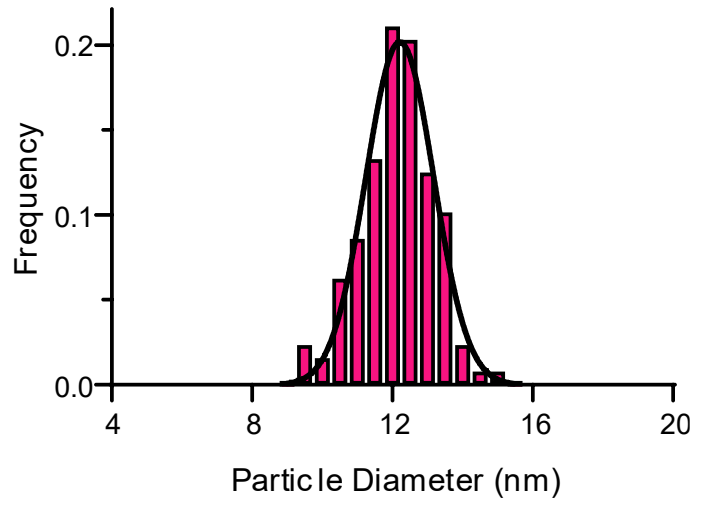
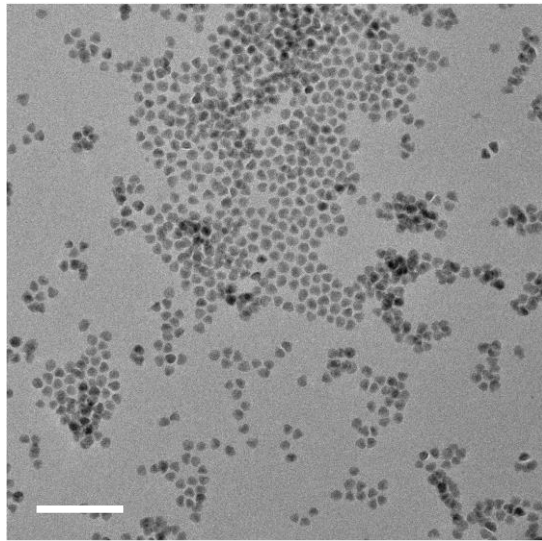


Figure B.1. Transmission electron microscopy (TEM) particle sizing of symmetrically shelled (symm-shelled) QDs.

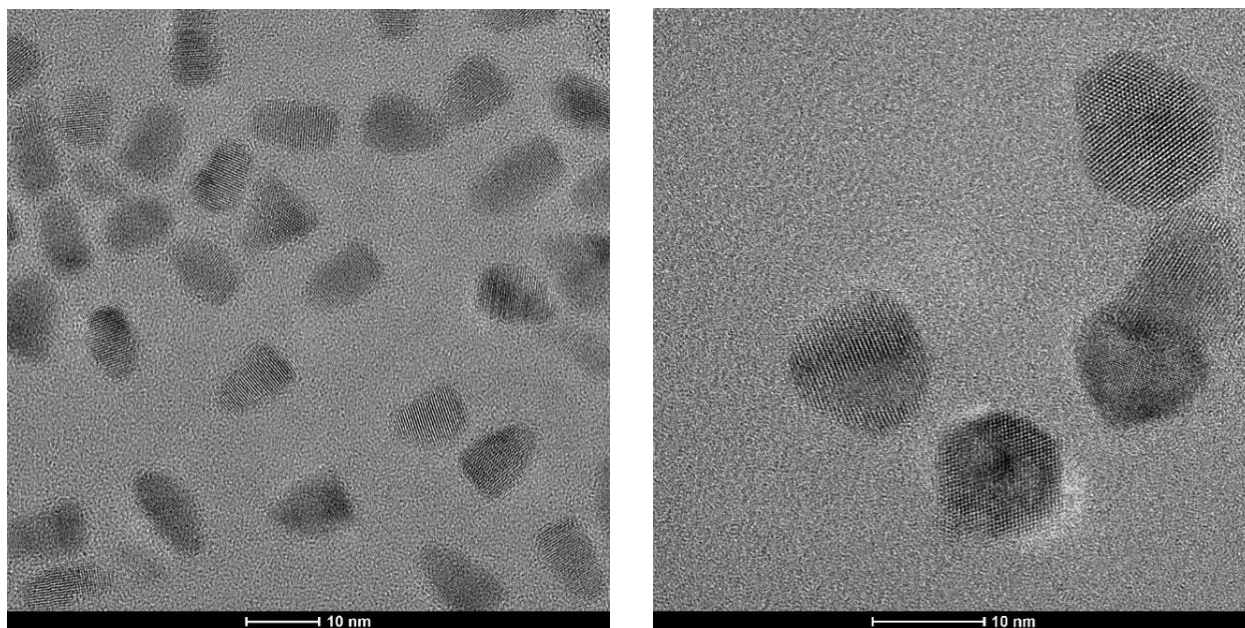


Figure B.2. High-resolution transmission electron microscopy (HRTEM) of (a) QD655s and (b) symm-shelled QDs. Images were acquired at different magnifications.

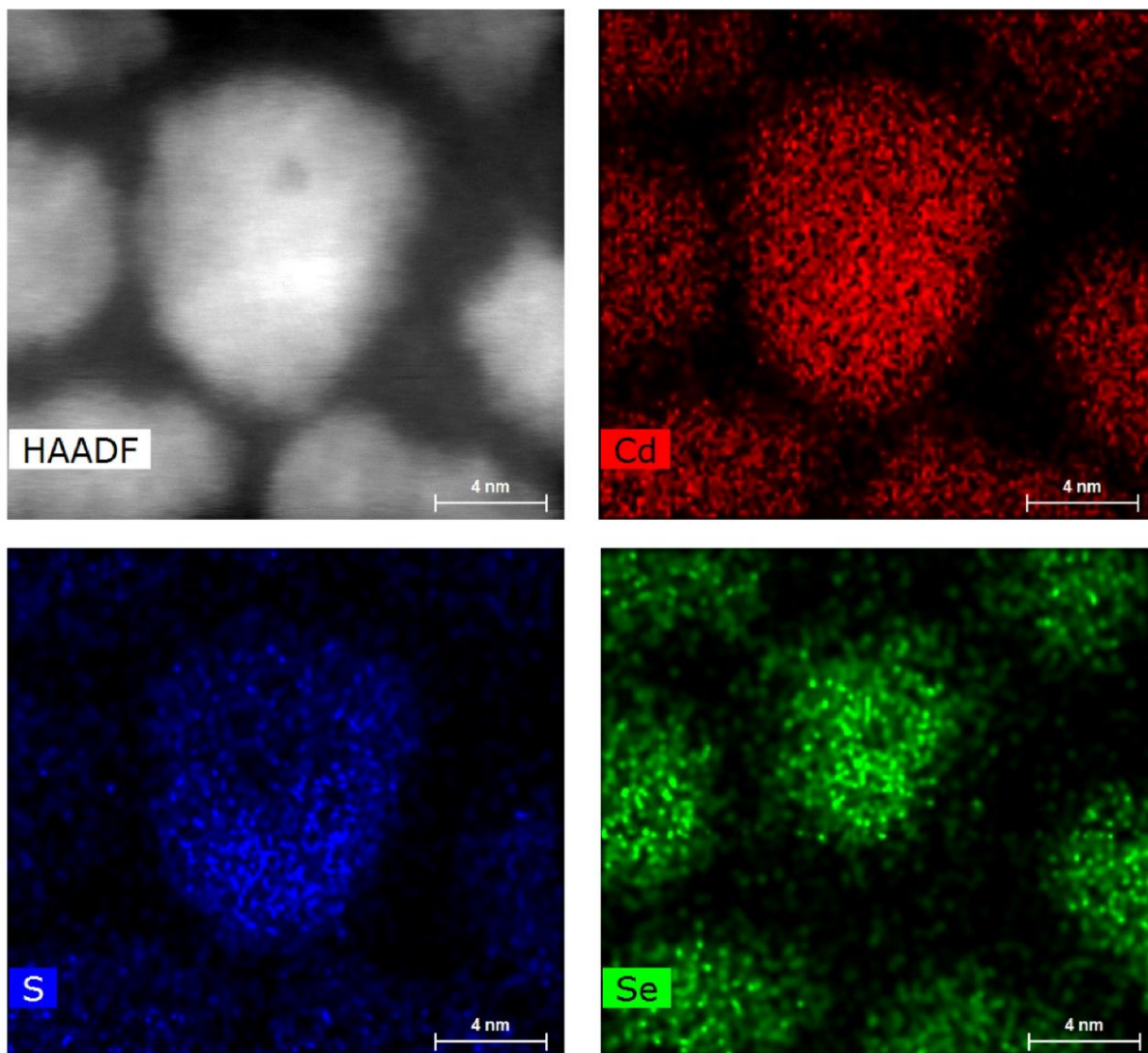


Figure B.3. Individual scanning transmission electron microscopy (STEM) images including high angle annular dark field (HAADF, grey) and Cd (red), S (blue) and Se (green) chemical maps for QD655s.

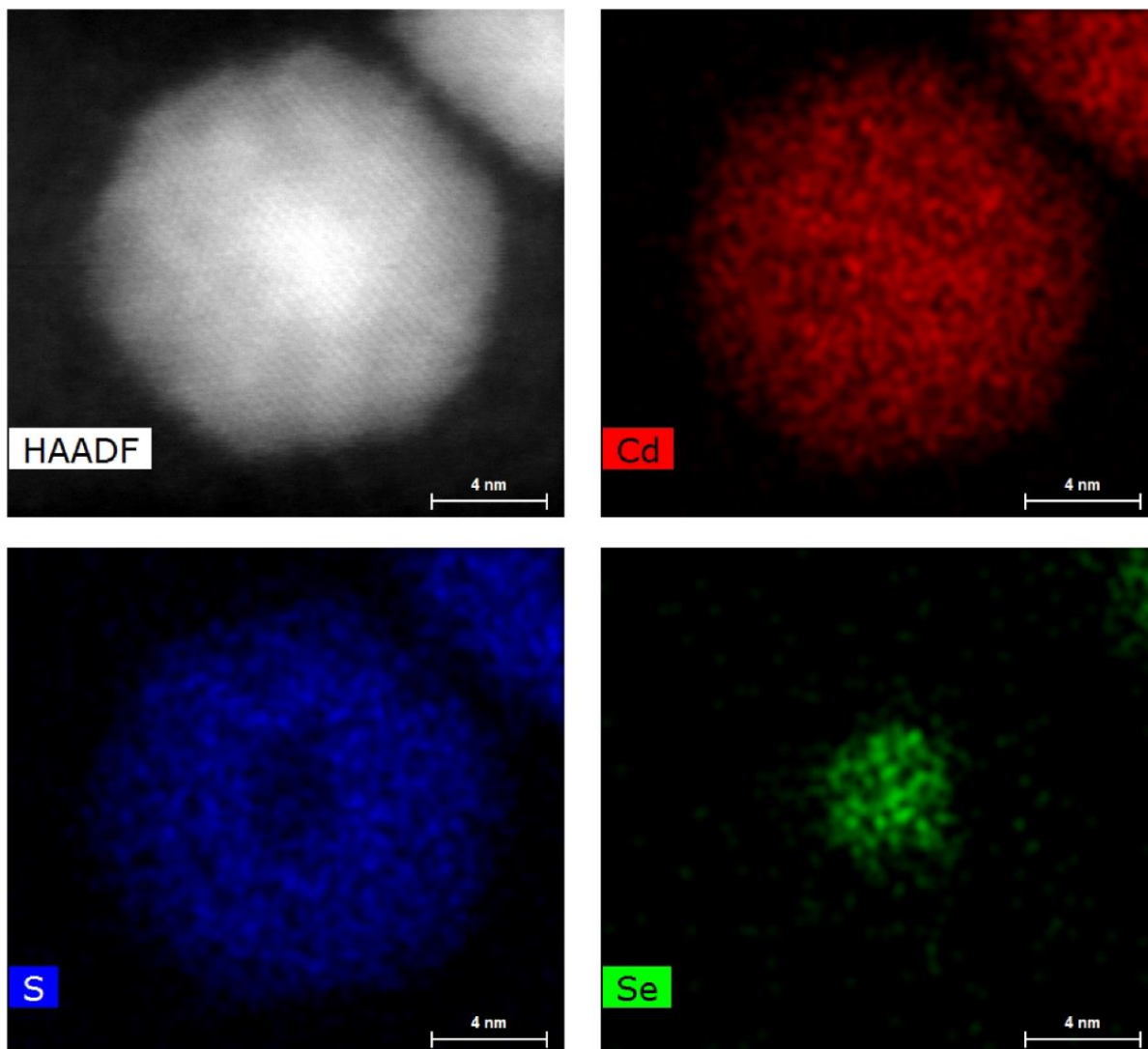


Figure B.4. Individual scanning transmission electron microscopy (STEM) images including high angle annular dark field (HAADF, grey) and Cd (red), S (blue) and Se (green) chemical maps for symmetrically shelled (symm-shelled) CdSe/CdS QDs.

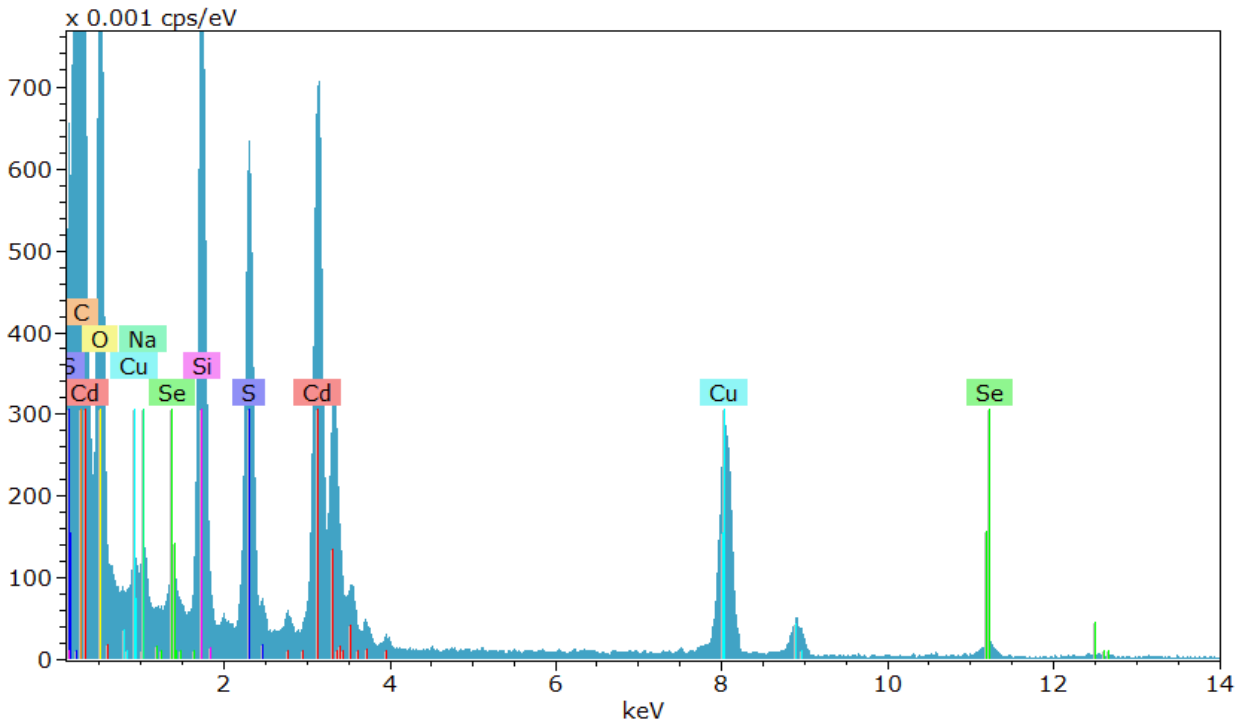


Figure B.5. Energy-dispersive X-ray spectrum of symmetrically shelled (symm-shelled) CdSe/CdS QDs.

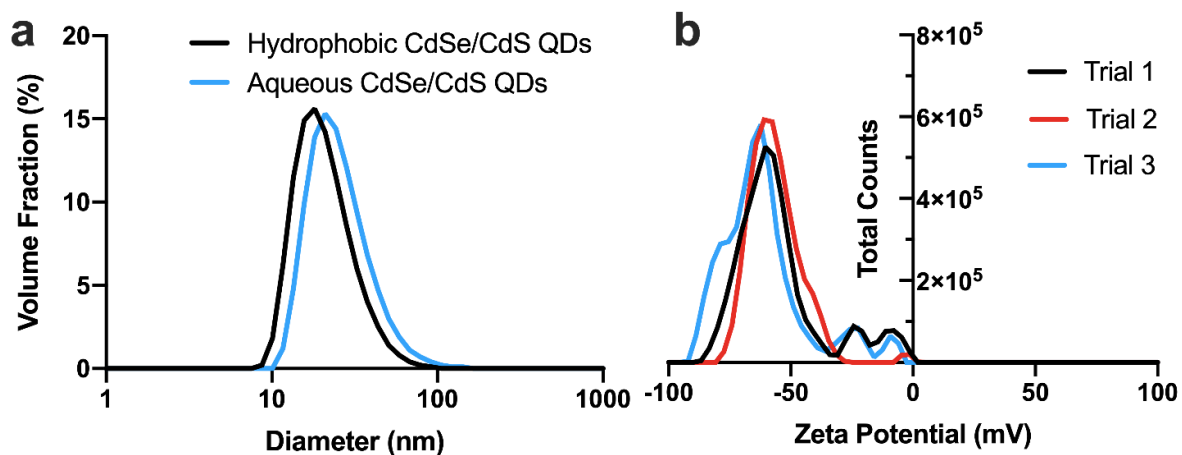


Figure B.6. (a) Dynamic light scattering size measurement of as-synthesized (hydrophobic, black) and PAOA-wrapped (aqueous, blue) symmetrically shelled CdSe/CdS QDs. Peak values found are 18.2 and 21.0 nm, respectively. (b) Three independent zeta potential scans of symmetrically shelled CdSe/CdS QDs with a mean potential of -60.6 ± 9.9 mV.

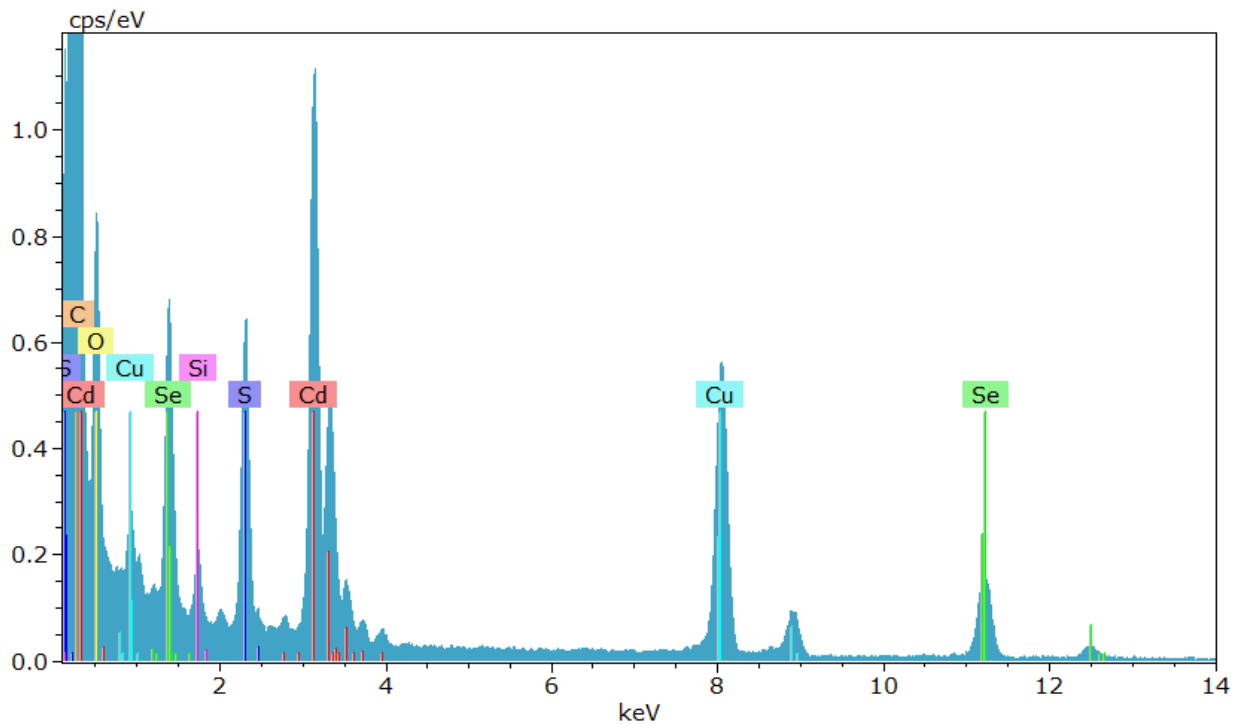


Figure B.7. Wide-window energy-dispersive X-ray spectrum of QD655s.

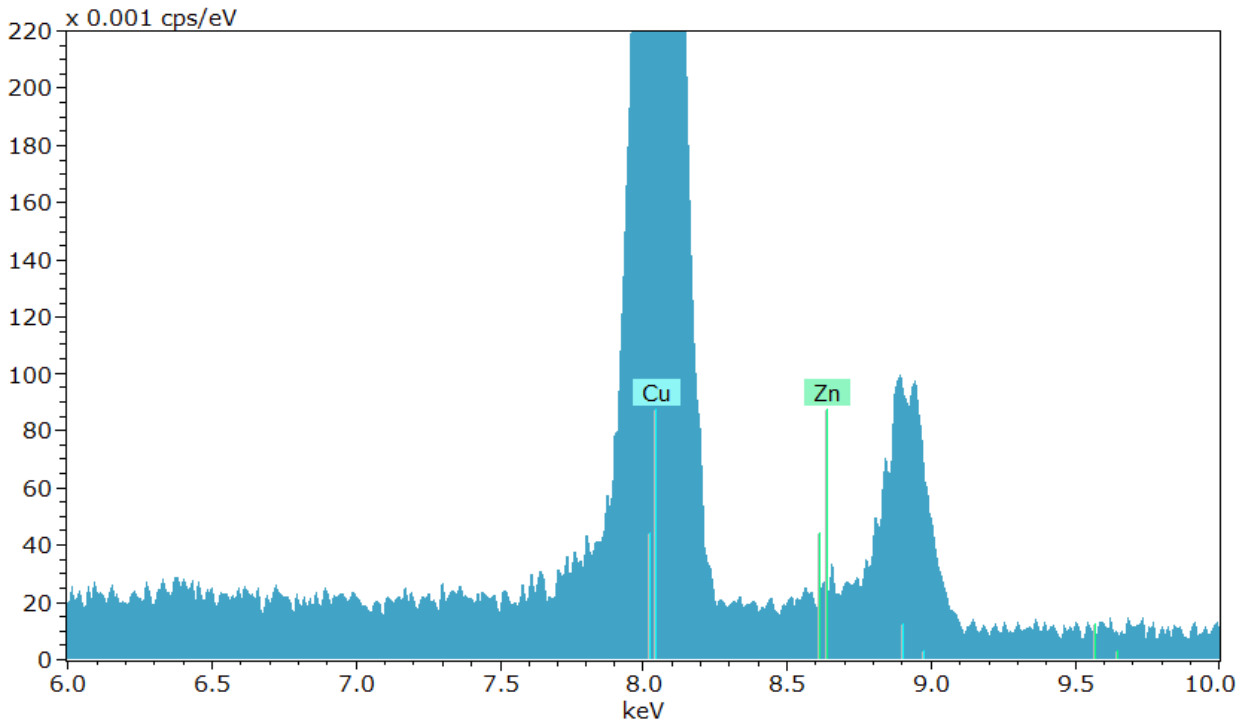


Figure B.8. Narrow-window energy-dispersive X-ray spectrum of QD655s highlighting little to no Zn signal.

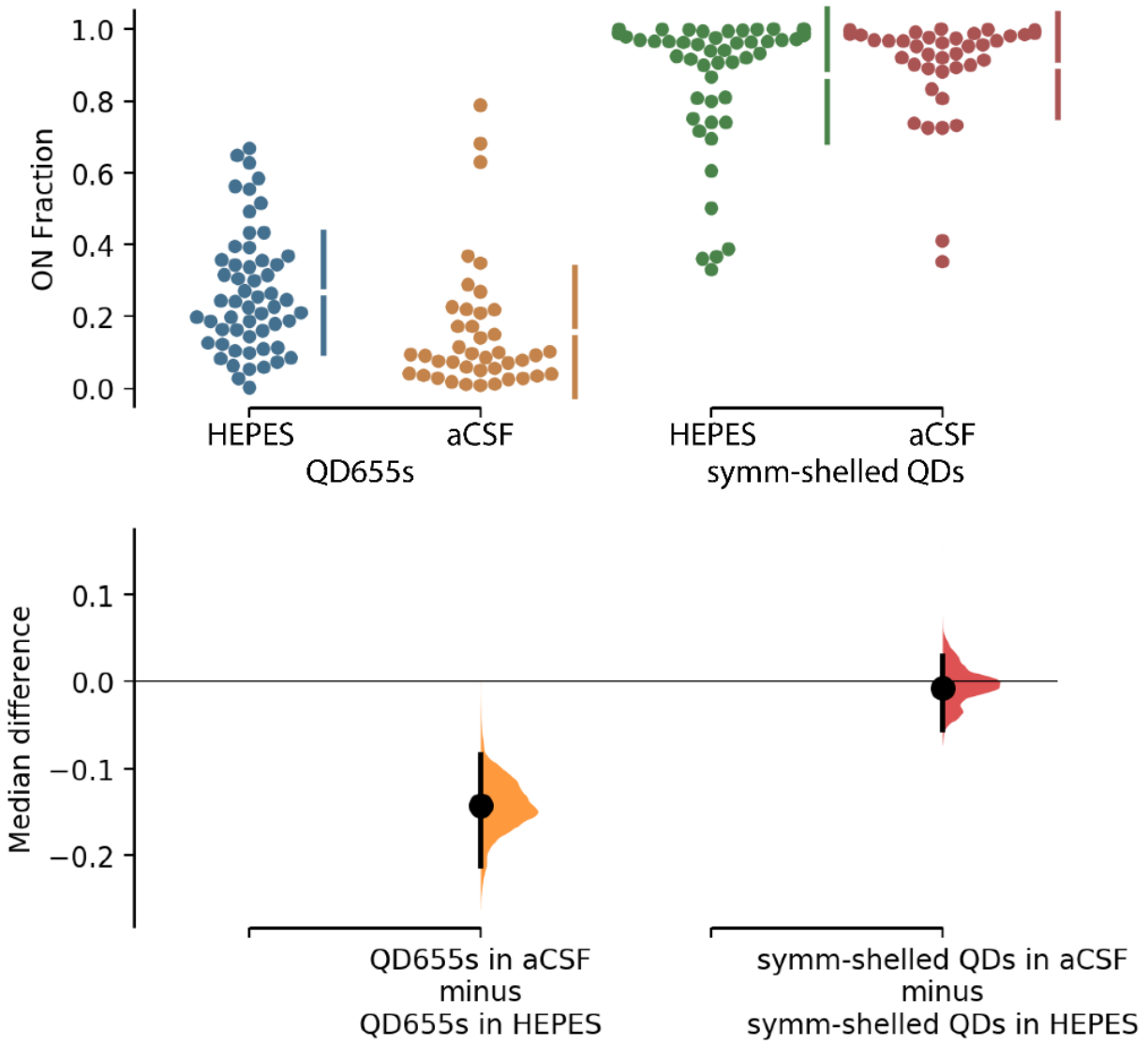


Figure B.9. Data analysis using bootstrap-coupled estimation (DABEST). Distributions of mean differences between QD subgroups displaying estimated effect sizes.

Table B.2. Summary of statistics value outputs from data analysis using bootstrap-coupled estimation (DABEST). P-values are outlined in blue.

Control Group	Test Group	Median Difference (ON-fraction)	Kruskal-Wallis p-value	Kruskal-Wallis H(2)
QD655s in HEPES symm-shelled QDs in HEPES	QD655s in aCSF	-0.142	7.32 x 10 ⁻⁵	15.72
	symm-shelled QDs in aCSF	-0.00783	0.909	0.013

APPENDIX C

QUANTUM DOT TOOLBOX IN MEMBRANE NEUROTRANSMITTER TRANSPORTER RESEARCH

Reprinted with permission of Thal, L. B., Bailey, D. M., Kovtun, O., and Rosenthal, S. J., Quantum Dot Toolbox in Membrane Neurotransmitter Transporter Research, in Chemical and Synthetic Approaches in Membrane Biology, Ed. A. K. Shukla, Springer New York, New York, NY, 2017, pp. 219–230. Copyright 2017. Springer Science+Business Media, LLC.

C.1 Introduction

Quantum dots (QDs) are semiconductor nanocrystals typically ranging from 4 to 10 nm in diameter. Owing to their inorganic nature, QDs exhibit unique photophysical properties controlled by shape, size, and composition (e.g. broad absorption spectra, high extinction coefficients, high quantum yield, narrow Gaussian emission spectra, photochemically stable). Nearly two decades ago, QDs were introduced as a new class of fluorescent probes for biological imaging.^{1,2} In contrast to organic dyes and fluorescent proteins, QDs undergo minimal photodegradation under continuous excitation and are easily resolved at video imaging rates. Consequently, QD probes have been particularly useful in the field of molecular neuroscience, where tracking of QD-labeled transmembrane neuronal receptors has shed light on the molecular mechanisms underlying receptor trafficking regulation.³⁻⁶ Our group focuses on the family of sodium-coupled transmembrane neurotransmitter transporters (NTTs), including serotonin transporter (SERT) and dopamine transporter (DAT). To address the lack of suitable antibodies against extracellular NTT epitopes, we pioneered the use of ligand-conjugated QDs for labeling NTTs and has expanded

	Technique	Parameters
Ensemble Analysis	<i>Fluorescence microscopy</i>	<i>Subcellular distribution with single cell sensitivity</i>
High Content Analysis	<i>Flow cytometry</i>	<i>Cellular expression level for $10^4 - 10^6$ cell populations</i>
Single Particle Tracking	<i>High-Speed Fluorescence microscopy</i>	<i>Lateral membrane diffusion at single molecule sensitivity</i>

Figure C.1. Quantum dot toolbox in NTT studies. We provide fluorescence detection methodology, achieved sensitivity, and obtained molecular parameters for each toolbox component.

these constructs to high-resolution microscopy, flow cytometry-based high content assays, and single QD tracking (Figure C.1). This chapter provides a set of detailed instructions and experimental considerations to allow readers to successfully implement our ligand-conjugated QD labeling approach in the study of NTTs and other neuronal transmembrane proteins. Specifically, we discuss the use of laser-scanning confocal microscopy, flow cytometry, and single particle tracking (SPT) to analyze localization, expression, and surface dynamics of NTTs, respectively.

C.2 Materials

1. No. 1.5 35-mm MatTek glass-bottom dishes (14 mm coverslip, MatTek Catalog # P35G-1.5-1.4-C)
2. Fluorobrite™ DMEM (ThermoFisher Catalog # A1896701)
3. 12 x 75 mm round bottom test tubes or 96-well round bottom microtiter plates
4. Phosphate-buffered saline (PBS; ThermoFisher Catalog #10010023)
5. Biotinylated NTT-specific ligand (1 mM stock in PBS)
6. Streptavidin-conjugated QDs (SavQDs; emission maximum at 655 nm; 1 μ M stock; ThermoFisher Catalog #Q10123MP)
7. QD binding buffer (borate buffer supplemented with 215 mM sucrose, 0.05% sodium azide, 1–5% bovine serum albumin (BSA) and/or 1–2% fetal bovine serum (FBS))
8. Staining buffer (PBS supplemented with 1–2% FBS)

9. Adherent cells transiently expressing NTT of interest
10. Analysis software (Microsoft Excel, ImageJ, MATLAB, FlowJo)
11. 24-well flat bottom culture plates
12. Optional: poly-D-lysine (working concentration of 0.01 mg/mL) to pre-coat 24-well culture plates when working with weakly adherent cell lines
13. Cell Stripper™ non-enzymatic cell dissociation solution (Corning Catalog #25-056-CI)
14. Optional: 0.25% Trypsin-EDTA (ThermoFisher Catalog #25200056)
15. 2.0-mL microcentrifuge tubes
16. 5-Laser BD LSRII flow cytometer configured with 355, 405, 488, 535, and 633 nm excitation lines as well as 8 PMT detectors
17. Carl Zeiss LSM 5 Live configured with a 63x 1.4NA oil immersion objective, solid-state laser diode (488 nm, 100 mW), and a linear array CCD

C.3 Subcellular Localization of QD-Bound Neurotransmitter Transporters

Ensemble fluorescence microscopy has emerged as an essential tool in biological research. Specifically, QD probes provide the user a spatial and visual guide for biomolecule accumulation and localization at subcellular levels. Our labeling approach based on antagonist-conjugated QDs has allowed us to visualize NTT delivery and localization within morphologically distinct subcellular compartments. Our group performed ensemble analysis utilizing a unique serotonin

transporter (SERT) antagonist, IDT318, to demonstrate polarized expression of QD-serotonin transporter (QD-SERT) in *Xenopus laevis* oocytes.⁷ We used the same ligand-QD system to show QD-SERT residing in ganglioside GM1-rich plasma membrane microdomains of immortalized rat serotonergic RN46A neuron.⁸ QD-based ensemble fluorescence microscopy has further enabled us to detect stimulated endocytosis of NTTs by monitoring the time course of QD internalization. By labeling dopamine transporters with streptavidin-conjugated QDs in conjugation with a biotinylated cocaine analog, IDT444, we detected internalization of QD dopamine transporter (QD-DAT) complexes upon protein kinase C (PKC) activation.⁹ We recommend using point scanning confocal microscope systems to generate high-resolution maps of NTT subcellular localization (Figure C.2). We provide in this section a general labeling approach for subcellular detection of NTTs in adherent cells (e.g., HeLa, HEK-293, N2A, CAD, SH-SY5Y) with antagonist-conjugated QDs.

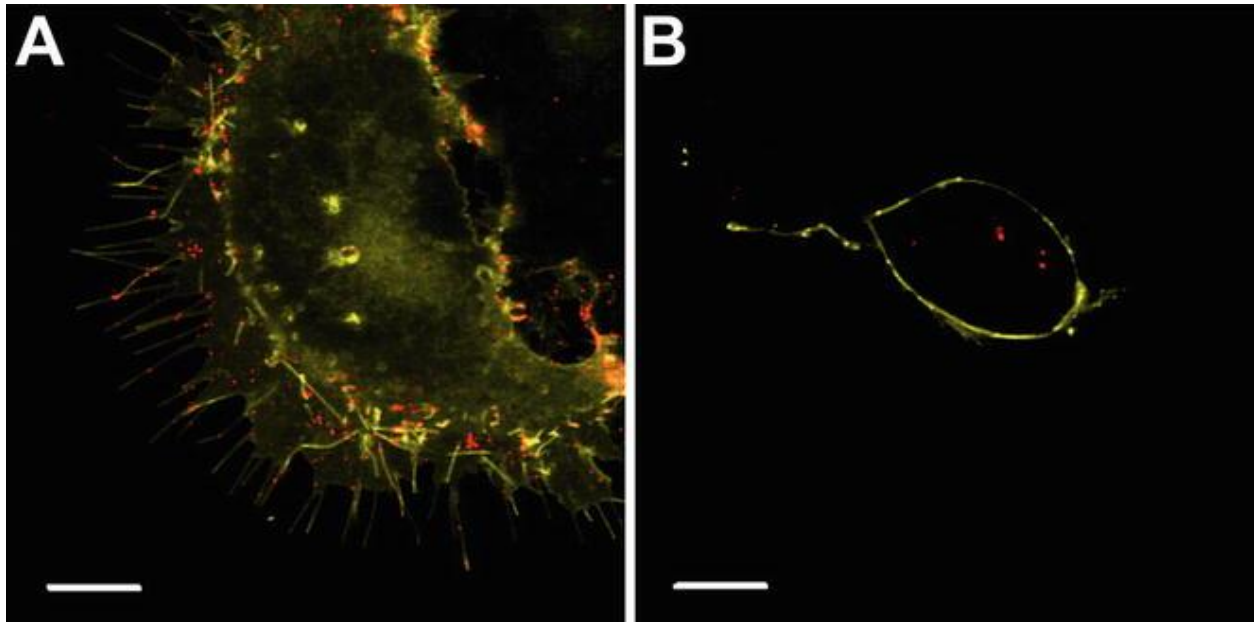


Figure C.2. Visualization of NTT subcellular localization using laser-scanning confocal microscopy. (a) QDs permit the user to readily identify whether NTTs are targeted to morphologically distinct membrane compartments (cell body, filopodia, lamellipodia). (b) QDs allow the user to observe and monitor the time course of NTT intracellular accumulation.

C.3.1 Protocol

1. Culture NTT-expressing cells in a No. 1.5 glass-bottom 35-mm MatTek dish. Optimal cell density for single-cell imaging is in the $0.5\text{--}5 \times 10^4$ cells/cm² range.
2. Prepare cells by aspirating complete growth medium and add 2 mL of 0.01–10 μM biotinylated NTT-specific ligand diluted in Fluorobrite™ DMEM. Alternatively, add a small aliquot of the 1 mM ligand stock solution directly to the complete growth medium.
3. Incubate the coverslip for 10–30 min in the cell culture incubator at 5% CO₂ and 37C.
4. Aspirate biotinylated NTT-specific ligand solution and wash the coverslip 3 times with pre-warmed Fluorobrite™ DMEM.

5. Promptly add a solution of 0.5–2.5 nM SavQDs in pre-warmed Fluorobrite™ DMEM supplemented with 1–5% BSA and/or 1–2% FBS to the MatTek dish.
6. Incubate the MatTek dish for 5–10 min in the cell culture incubator at 5% CO₂ and 37C.
7. Aspirate the QD solution and wash the MatTek dish 3–5 times with pre-warmed Fluorobrite™ DMEM.
8. Replenish the MatTek dish with pre-warmed Fluorobrite™ DMEM to prepare for imaging.
9. Immediately mount the MatTek dish on a heated microscope stage and acquire individual images using DIC and appropriate fluorescence bandpass filters.

C.3.2 Experimental Considerations

1. All QD labeling steps should be done with minimal exposure to light.
2. Use a complete set of controls including unstained cells, NTT-expressing cells labeled with SavQD only (-biotinylated NTT-specific ligand), non-expressing cells labeled with biotinylated ligand and QDs, and NTT-expressing cells preincubated with a high-affinity inhibitor to block the transporter–ligand interaction.
3. If the user is observing non-specific QD binding, decrease cell debris on coverslip by keeping cells in viable media, temperature, and atmosphere, increase percentage of BSA when incubating QDs, treat with other passivation reagents (casein, newborn calf serum, dehydrated fat-free milk) in addition to or replacing FBS, and/or increase number of wash steps.
4. If the user is experiencing low signal-to-noise ratio, adjust pinhole size, gain, and amplitude,

increase excitation intensity, and/or adjust SavQD concentration in step 5 in the labeling protocol.

C.4 Flow Cytometric Detection of Quantum Dot-Labeled Neurotransmitter Transporters in Single Cells

Flow cytometry has emerged as one of the premier analytical tools that enables rapid multi-parameter molecular phenotyping and functional profiling with a single-cell sensitivity. With recent advances in hardware, reagent availability, and software, it is now possible to routinely implement polychromatic (up to 17 spectrally distinct fluorophores on a 5-Laser BD LSRII instrument) flow cytometry analyses. QDs are particularly well suited for polychromatic applications of flow cytometry aimed at detection of surface biomolecules due to broad absorption spectra and size tunable narrow emission spectra. We have recently utilized antagonist-conjugated QDs to monitor changes in DAT surface levels and DAT-mediated antagonist binding in response to external stimuli in HEK-293 cells stably expressing transmembrane DAT molecules.¹⁰ This report was an experimental demonstration that flow cytometric detection of QD-labeled cells represents an attractive alternative to the current “gold standard” techniques in the field of NTT research – radioligand uptake assay and Western blot – effectively eliminating the need for radiolabeled isotopes and time-consuming, expensive immunoblotting. In this section, we provide detailed guidelines for detecting surface NTT molecules transiently expressed in an adherent cell platform (e.g., HeLa, HEK-293, N2A, CAD, SH-SY5Y) with ligand-conjugated QDs and implementing flow cytometric analysis of the resulting cell suspension.

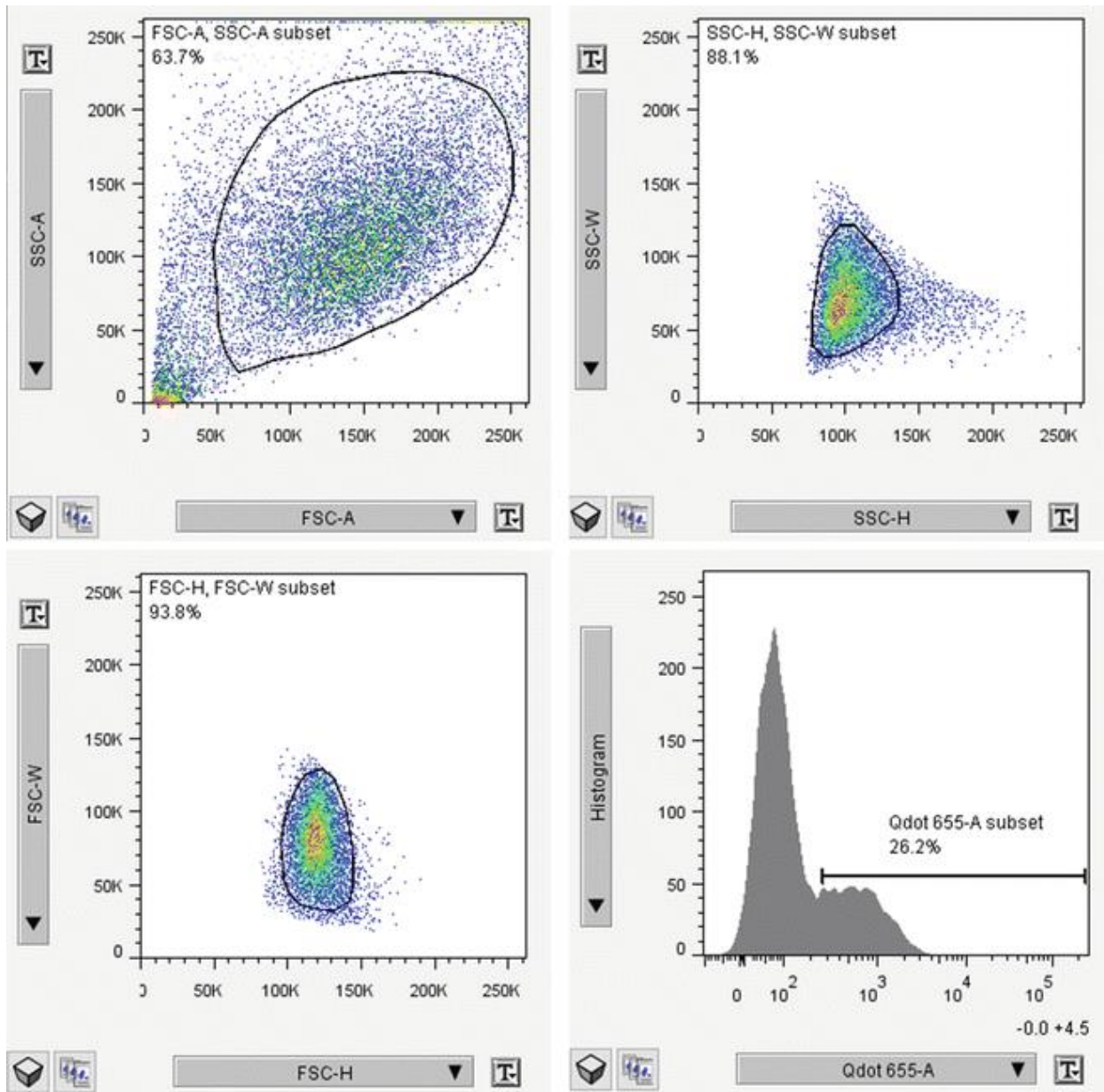


Figure C.3. Flow cytometric detection QD-labeled cells transiently expressing NTT of interest. Forward scatter (FSC) and side scatter (SSC) pulse area, height, and width are used to discriminate single-cell events from cell doublets and cell debris. The histogram of the gated population shows a fluorescence intensity distribution of single cells. The characteristic bimodal pattern indicates the presence of a dim population (non-transfected cells, hence low QD fluorescence intensity) and a bright fraction (transfected cells, higher QD fluorescence intensity)

C.4.1 Protocol

1. Allow NTT-expressing cells growing in a 24-well plate culture plate to reach 80–90% confluency.
2. Prepare cells by aspirating complete growth medium and add 500 μL of a 0.01–10 μM biotinylated NTT-specific ligand diluted in PBS.
3. Incubate the 24-well plate for 10–30 min in the cell culture incubator at 5% CO_2 and 37C.
4. Carefully aspirate the ligand solution, dissociate the cells from the plate bottom using Cell Stripper™ (use 0.25% Trypsin-EDTA for lifting strongly adherent cells), and transfer the resulting cell suspension to 2.0 mL microcentrifuge tubes.
5. Pellet the cells by centrifugation at 1,000–3,000 rpm for 5 min.
6. Discard supernatant by gentle aspiration and resuspend the labeled cells in 500 μL of cold QD binding buffer containing 0.5–2.5 nM streptavidin-conjugated QDs. Incubate on ice for 5–10 min.
7. Pellet the cell by centrifugation at 1,000–3,000 rpm for 5 min. Discard supernatant by aspiration and wash the cells by resuspending in cold staining buffer followed by immediate centrifugation at 1,000–3,000 rpm for 5 min.
8. Repeat for a total of two washes, discarding supernatant between washes.
9. Resuspend the pellet in 500 μL of cold staining buffer and transfer samples to either round bottom test tubes or a 96- well round bottom microtiter plate.

10. [OPTIONAL] Add a viability dye to each sample to exclude dead cells from analysis.
11. Acquire data on a flow cytometer. A representative data set is displayed in Figure C.3.
12. Use forward scatter (indicator of size) and side scatter (indicator of surface roughness, granularity, and internal complexity) pulse width, height, and area to discriminate single cells from cell doublets and cell debris.
13. Collect 20,000–100,000 single-cell events for the gated population.

C.4.2 Experimental Considerations

1. Single-cell suspensions at a density of 10^6 – 10^7 cells/mL are ideal.
2. All QD labeling steps should be done with minimal exposure to light.
3. Always include a rigorous set of controls and use a negative control to set voltages and gates. Recommended controls include unstained cells, NTT-expressing cells labeled with QD only, non-expressing cells labeled with biotinylated NTT-specific ligand and QDs, and NTT-expressing cells preincubated with a high-affinity inhibitor to block the transporter–ligand interaction.
4. Include BSA and/or FBS to block non-specific interactions of QDs with the cell surface.
5. Determine the number of single-cell events that must be collected to ensure that your sampling is statistically significant (10^4 – 10^5 single viable cells per final scatter gate per sample is usually sufficient).
6. For multicolor experiments, always include single-color controls to determine fluorescence

compensation settings to address the spectral overlap of fluorophores used.

C.5 Single Particle Tracking of Neurotransmitter Transporters

In contrast to ensemble approaches discussed in Sects. 3 and 4, SPT permits real-time observation of NTTs in the plasma membrane at a subdiffraction-limited spatial resolution and imaging rates at ≥ 10 Hz. As surface NTT trafficking appears to be an important post-translational regulatory mechanism, SPT analysis can provide invaluable information about NTT lateral diffusion dynamics, membrane compartmentalization, and dynamic interactions with its binding partners. QDs are bright, robust point-like emitters characterized by a narrow, well-defined point-spread function (PSF) and therefore a probe choice in SPT studies (Figure C.4).¹¹ QDs act as point emitters (Figure C.4) that can be modeled with the PSF for use in SPT. The point emitters must be separated farther than the diffraction-limited regime and thus must be in sufficiently low concentration. The centroid positions can then be localized with subpixel accuracy by fitting the intensity distribution to a 2D Gaussian function:

$$I_{xy} = A_0 + A \times e^{-\frac{(x-x_0)^2+(y-y_0)^2}{w^2}}$$

where I_{xy} is the pixel intensity, A is signal amplitude, A_0 is local background, x_0 and y_0 are the local maximum coordinates of the Gaussian fit, and w is the width of the curve.¹² The accuracy of the fit depends on the signal-to-noise ratio (SNR):

$$SNR = \frac{I_0}{\sqrt{\sigma_{bg}^2 + \sigma_{I_0}^2}}$$

where I_0 is the signal intensity, σ_{bg} is the variance of the background intensity, and σ_I is the variance of the signal intensity.¹² QDs significantly increase the SNR compared to common organic fluorophores, providing another advantage as single molecule imaging probes. Once precise localization data (x, y) is determined, QD positions in successive frames must be linked to construct trajectories. We previously described in detail basic analysis using ImageJ.¹² Once trajectories are constructed, net displacement and velocities can be determined, as well as mean square displacement (MSD) (Figure C.5):

$$MSD(n\Delta t) = (N - n)^{-1} \sum_{i=1}^{N-1} [(x_{i+n} - x_i)^2 + (y_{i+n} - y_i)^2]$$

where $n\Delta t$ is the time interval in which the MSD is calculated, N is the total number of frames, and x_i and y_i are positions of the particle over time. Our recent group efforts focused on visualizing and analyzing NTT membrane dynamics using antagonist-conjugated QDs. We first utilized a SERT antagonist, IDT318, to specifically label individual SERT proteins within the membranes of serotonergic RN46A cells. We observed two distinct populations, one that freely diffused across the membrane and one that displayed restricted mobility and was confined to membrane microdomains. Upon SERT stimulation, individual proteins remained confined within microdomains but displayed untethering from cytoskeletons that allowed for increased mobility through a p38 MAPK pathway.⁸ Next we visualized the dynamics of wild-type and ADHD-associated mutant (R615C) DAT using a high-affinity biotinylated cocaine analog, IDT444, and streptavidin-conjugated QDs in living transfected HEK-293 cells. From QD trajectory analysis, the R615C mutant showed increased lateral mobility in the membrane compared to the wild-type protein and lacked response to cholesterol depletion and amphetamine stimulation.¹³ These findings demonstrate, for the first time, how a disease-associated mutation affects the surface

dynamics of single DAT molecules, which opens up possibilities for future studies linking disease states with individual molecular behavior. This protocol outlines QD labeling in NTT-expressing adherent cell lines and provides a set of common troubleshooting tips.

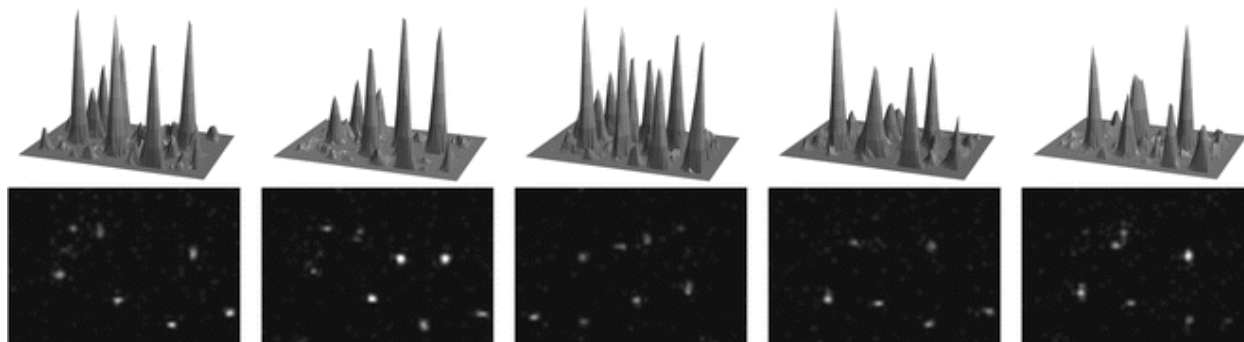


Figure C.4. Typical video frame sequence of single QDs bound to NTT molecules. Bottom: Raw image sequence of diffusing QDs. Top: Corresponding surface intensity plots used for QD localization

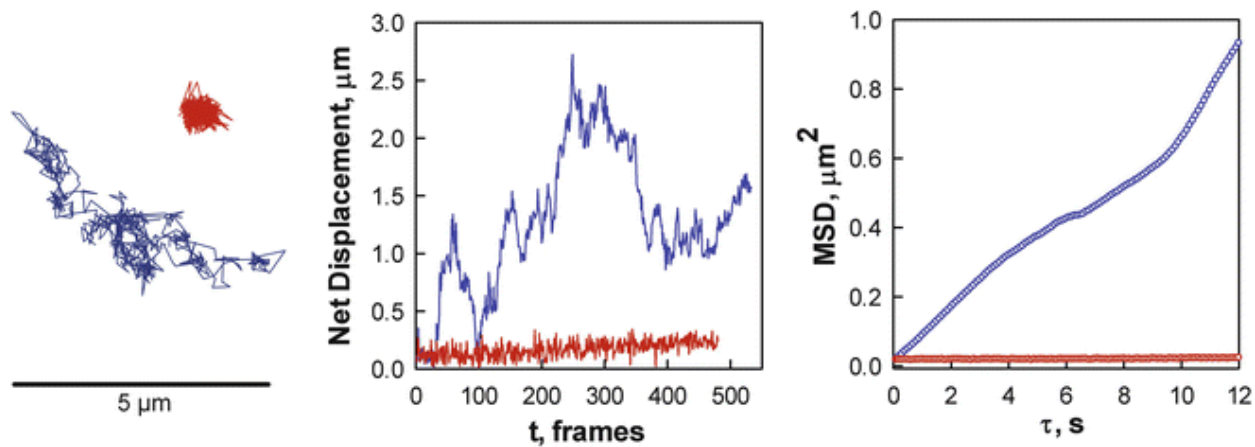


Figure C.5. Basic analysis of example trajectories shows plots of displacement from the starting position and MSD for a confined (red) and freely diffusing (blue) particle

C.5.1 Protocol

1. Culture NTT-expressing cells in glass-bottom dishes until they are 50–60% confluent.
2. Prepare a solution of 0.01–0.1 nM SavQDs in warm Fluorobrite™ DMEM media containing 2–5% BSA or 1–2% dialyzed FBS. Vortex for 5 s to break up aggregates.
3. Add 0.1–0.5 nM biotinylated NTT-specific ligand directly to culture media and incubate for 5 min.
4. Wash cells gently 3–5 times with phenol-red free DMEM or Fluorobrite™ DMEM.
5. Add QD solution to cells and incubate at 37C for 5 min.
6. Wash cells gently 3–5 times with warm Fluorobrite™ DMEM. 7. Place the dish on a heated (37C) microscope stage and acquire time-lapse images.

C.5.2 Experimental Considerations

1. A frame rate of 10 frames per second or faster is recommended using an appropriate filter for the type of QD. A 600/30 bandpass filter is used for 605 QDs.
2. Image in a low-background buffer, like Fluorobrite™ DMEM, to improve signal-to noise ratio.
3. Include a blocking reagent, such as BSA, dialyzed FBS, or casein, to decrease non-specific labeling of QDs.
4. Avoid QD internalization by imaging immediately after labeling.
5. Decrease QD incubation time if QDs are internalizing.

6. Determine ligand specificity using controls (see section C.3.2 for example control experiments).

C.6 References

1. Bruchez, M, Moronne, M, Gin, P, Weiss, S, and Alivisatos, A. P., Semiconductor nanocrystals as fluorescent biological labels, *Science*, **1998**, 281, 2013–2016.
2. Chan, W. C. W., and Nie, S, Quantum dot bioconjugates for ultrasensitive nonisotopic detection, *Science*, **1998**, 281, 2016–2018.
3. Dahan, M., Levi, S., Luccardini, C., Rostaing, P., Riveau, B., and Triller, A., Diffusion dynamics of glycine receptors revealed by single-quantum dot tracking, *Science*, **2003**, 302, 442–445.
4. Bouzigues, C., Morel, M., Triller, A., and Dahan, M., Asymmetric redistribution of GABA receptors during GABA gradient sensing by nerve growth cones analyzed by single quantum dot imaging, *Proc. Natl. Acad. Sci. U. S. A.*, **2007**, 104, 11251–11256.
5. Rosenthal, S. J., Chang, J. C., Kovtun, O., McBride, J. R., and Tomlinson, I. D., Biocompatible Quantum Dots for Biological Applications, *Chem. Biol.*, **2011**, 18, 10-24.
6. Frischknecht, R., Heine, M., Perrais, D., Seidenbecher, C. I., Choquet, D., and Gundelfinger, E. D., Brain extracellular matrix affects AMPA receptor lateral mobility and short-term synaptic plasticity, *Nat. Neurosci.*, **2009**, 12, 897–904.
7. Chang, J. C., Tomlinson, I.D., Warnement, M.R., Iwamoto, H., DeFelice, L. J., Blakely, R.D., and Rosenthal, S.J., A fluorescence displacement assay for antidepressant drug discovery based on ligand-conjugated quantum dots, *J. Am. Chem. Soc.*, **2011**, 133, 17528–17531.
8. Chang, J. C., Tomlinson, I. D., Warnement, M. R., Ustione, A., Carneiro, A. M. D., Piston, D. W., Blakely, R. D., and Rosenthal, S. J., Single Molecule Analysis of Serotonin Transporter Regulation Using Antagonist-Conjugated Quantum Dots Reveals Restricted, p38 MAPK-Dependent Mobilization Underlying Uptake Activation, *J. Neurosci.*, **2012**, 32, 8919-8929.
9. Kovtun, O., Tomlinson, I. D., Sakrikar, D. S., Chang, J. C., Blakely, R. D., and Rosenthal, S. J., Visualization of the Cocaine-Sensitive Dopamine Transporter with Ligand-Conjugated Quantum Dots, *ACS Chem. Neurosci.*, **2011**, 2, 370-378.
10. Kovtun, O., Ross, E.J., Tomlinson, I.D., and Rosenthal, S.J., A flow cytometry-based dopamine transporter binding assay using antagonist-conjugated quantum dots. *Chem. Commun.*, **2012**, 48, 5428–5430.
11. Chang, J.C., and Rosenthal, S.J., A bright light to reveal mobility: single quantum dot tracking

reveals membrane dynamics and cellular mechanisms, *J. Phys. Chem. Lett.*, **2013**, 4, 2858–2866.

12. Chang, J.C., Rosenthal, S.J., Quantum Dot-Based Single-Molecule Microscopy for the Study of Protein Dynamics, In *NanoBiotechnology Protocols*, Rosenthal, S.J., Wright D.W., Eds, Humana Press, New York, pp 71–84.

13. Kovtun, O., Sakrikar, D., Tomlinson, I. D., Chang, J. C., ArzetaFerrer, X., Blakely, R. D., and Rosenthal, S. J., Single-quantum dot tracking reveals altered membrane dynamics of an attentiondeficit/hyperactivity-disorder-derived dopamine transporter coding variant, *ACS Chem. Neurosci.*, **2015**, 6, 526–534.

APPENDIX D

QD-BASED APPROACH TO SURVEY 3D DISTRIBUTION AND DYNAMICS OF ENDOCYTOSED TRANSPORTERS

*This section includes adapted text with permission of Kovtun, O., Tomlinson, I. D., Bailey, D. M., Thal, L. B., Ross, E. J., Harris, L., Frankland, M. P., Ferguson, R. S., Glaser, Z., Greer, J., and Rosenthal, S. J., Single quantum dot tracking illuminates neuroscience at the nanoscale, Chem. Phys. Lett., **2018**, 706, 741–752. Copyright 2018. Elsevier.*

Decades of research efforts aimed at unraveling the intricacies of neurotransmitter transporter trafficking support the notion that membrane pool of transporters is in constant flux, and proper transporter turnover represents an important modulatory mechanism of synaptic plasticity. Membrane transporters undergo marked constitutive and regulated redistribution away from the plasma membrane driven in part by amino-/carboxy-terminal linear motifs, conformational shifts, and covalent modifications.¹⁻³ Although transporter turnover is an essential component of neurotransmission, the intracellular dynamics and subsequent fate of individual transporters remain poorly understood. Our ligand-conjugated QD approach is uniquely suited to interrogate the intracellular dynamics of transporters in living cells because (i) pseudoirreversible ligand binding ensures that the transporter-QD complex remains intact post-endocytosis and (ii) bright and stable QD signal enables prolonged observation of single cargo trafficking.⁴⁻⁶ A proof-of-concept implementation of our QD labeling approach together with spinning-disk confocal microscopy to investigate DAT endocytic trafficking is shown in Figure D.1A. Notably, the

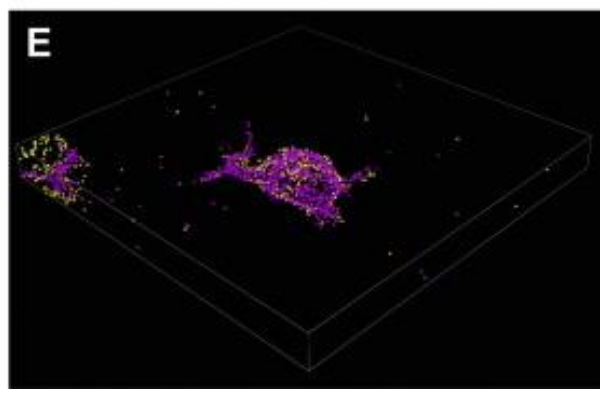
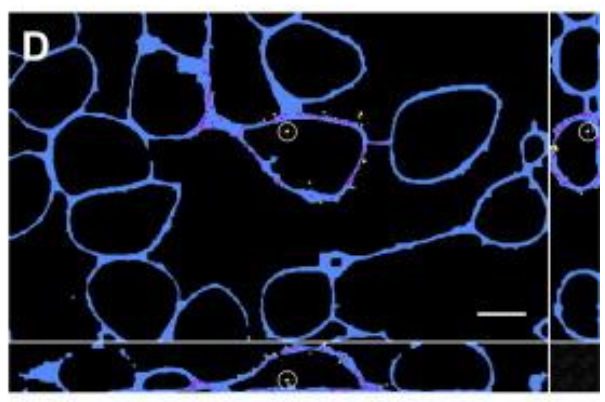
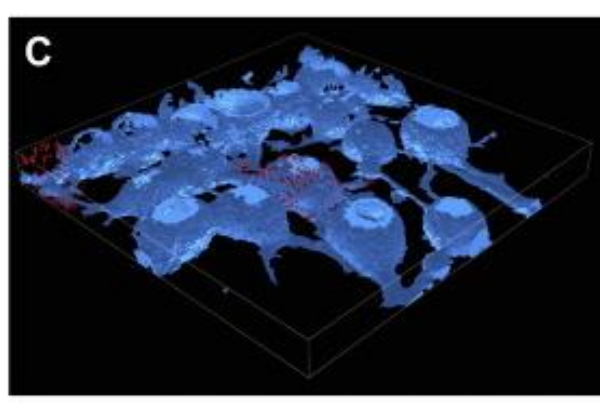
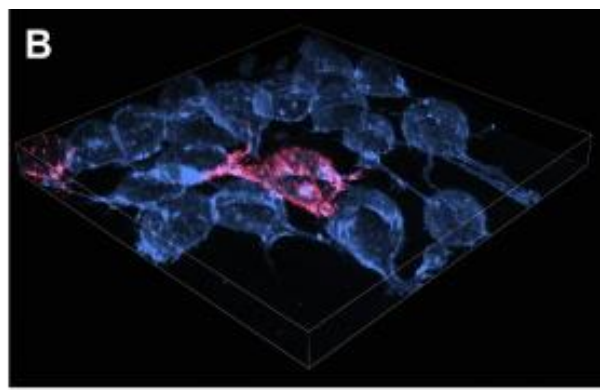
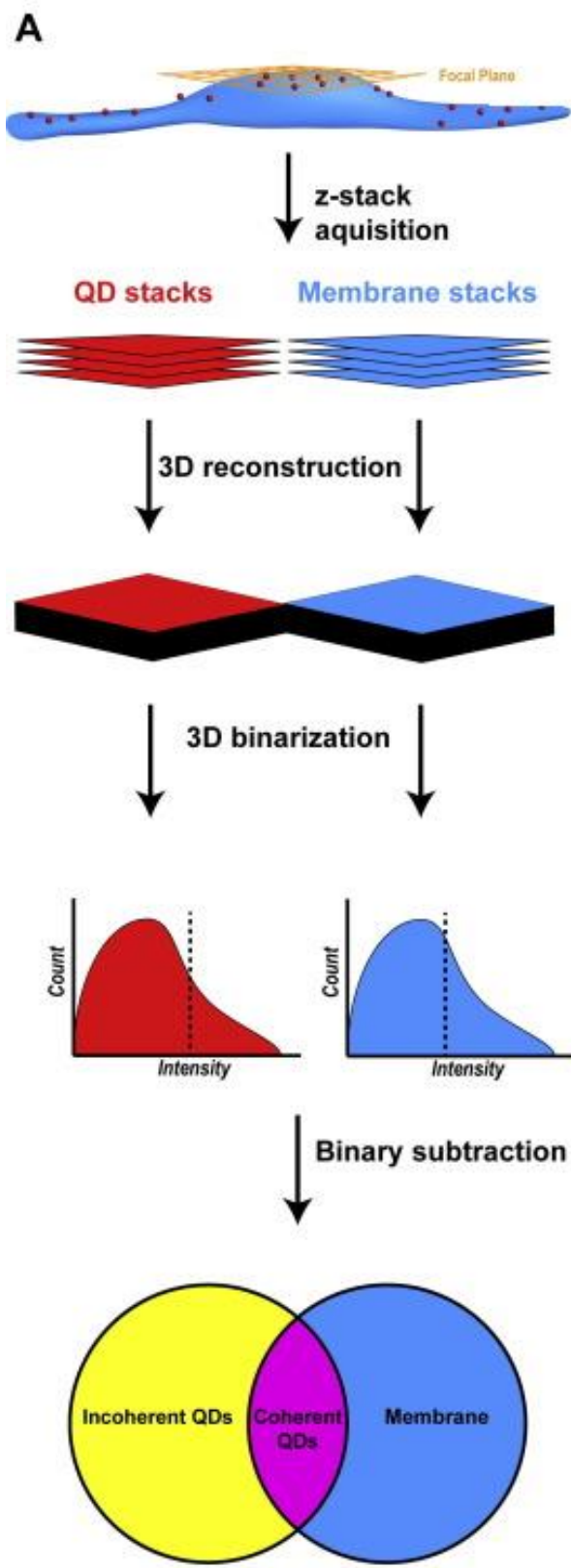


Figure D.1. Spinning-disk confocal microscopy and single QD localization to analyze endocytosed DAT. (A) An analytical workflow outlining image z-stack acquisition, 3D reconstruction, 2channel 3D binarization, and subtractive object analysis. Note the Venn diagram demonstrates discrimination of QD object coherence to the cell membrane localization. (B) A representative 3D image overlay of an HEK-293 cell expressing DAT labeled with ligand-conjugated QDs (red) and cell membranes labeled with CellMask (blue). (C) 3D binarized imaging data represented in (B) of both QD and CellMask channels. (D) A Z-slice accompanied by orthogonal XZ and YZ slices highlighting membranous (magenta) and nonmembranous (yellow) DAT-QDs. The endocytosed DAT-QD is clearly demonstrated (white circles). (E) A 3D representation of the binarized QD channel in [C] nonmembranous and membranous DAT-QDs.

spinning-disk microscope is equipped with a z-axis piezo nanopositioning stage, which enabled capture of transient endocytic events and robust single cargo localization analysis. At z-speeds of 10 300-nm steps per second, 3D image stacks were acquired to detect DAT-QD complexes relative to the plasma membrane of transiently transfected HEK-293 cells, conveniently labeled with a CellMask™ lipophilic membrane stain (Figure D.1B). Binarizing the acquired z-stacks and performing 2-channel colocalization analysis allows us to discriminate intracellular QDs from those localized to the plasma membrane (Figure D.1C-E). By incorporating an additional fluorescent marker of early recycling endosomes or late degradative compartments, our approach could be a valuable tool for quantitative determination of DAT intracellular fate at the single-cargo level in 3D.

D.2 References

1. Melikian, H.E., Neurotransmitter transporter trafficking: endocytosis, recycling, and regulation, *Pharmacol. Ther.*, **2004**, 104, 17–27.
2. Eriksen, J., Bjorn-Yoshimoto, W.E., Jorgensen, T.N., Newman, A.H., Gether, U., Postendocytic sorting of constitutively internalized dopamine transporter in cell lines and dopaminergic neurons, *J. Biol. Chem.*, **2010**, 285, 27289–27301.
3. Bermingham, D. P. and Blakely, R. D., Kinase-dependent regulation of monoamine neurotransmitter transporters, *Pharmacol. Rev.*, **2016**, 68, 888–953.
4. Kovtun, O., Tomlinson, I. D., Sakrikar, D. S., Chang, J. C., Blakely, R. D., and Rosenthal, S. J., Visualization of the Cocaine-Sensitive Dopamine Transporter with Ligand-Conjugated Quantum Dots, *ACS Chem. Neurosci.*, **2011**, 2, 370-378.
5. Kovtun, O., Sakrikar, D., Tomlinson, I. D., Chang, J. C., ArzetaFerrer, X., Blakely, R. D., and Rosenthal, S. J., Single-quantum dot tracking reveals altered membrane dynamics of an attentiondeficit/hyperactivity-disorder-derived dopamine transporter coding variant, *ACS Chem. Neurosci.*, **2015**, 6, 526–534.
6. Thal, L. B., Tomlinson, I. D., Quinlan, M. A., Kovtun, O., Blakely, R. D., and Rosenthal, S. J., Single Quantum Dot Imaging Reveals PKC β -Dependent Alterations in Membrane Diffusion and Clustering of an Attention-Deficit Hyperactivity Disorder/Autism/Bipolar Disorder-Associated Dopamine Transporter Variant, *ACS Chem. Neurosci.*, **2019**, 10, 460–471.

APPENDIX E

VERIFICATION OF AN INTACT QD-IDT725 CONJUGATE BY SURFACE- ENHANCED RAMAN SPECTROSCOPY

Since the symm-shelled QDs in Chapter 4 were conjugate stocks on the order of nanograms, the sensitivity of nuclear magnetic resonance spectroscopy (NMR) is too low to characterize the ligand-conjugated QD structure. Consequently, surface-enhanced Raman spectroscopy (SERS) was used to verify the intact conjugate. Upon preliminary evaluation of a wide spectral window (Figure E.1A), the region between 900 cm^{-1} and 1200 cm^{-1} was chosen for further analysis (Figure E.1B). The spectra for QD-IDT725 were remarkably distinct from the SERS substrate spectra and the QD (-IDT725) spectra. Signature asymmetric and symmetric aromatic stretches from the β -CFT cocaine analog were present, consistent with previously reported results.¹

Commercial SERS substrates contributed to the reproducibility of the workflow given the quality control in manufacturing (Figure E.2A, Ocean Optics). However, the short shelf life combined with long shipping times from the manufacturer motivated me to construct in-house substrates. By cutting circular Whatman #1 filter paper using a handheld hole puncher, paper pads were prepared as a matrix for the SERS substrates (Figure E.2B). These paper pads were incubated in a colloidal suspension of 60 nm Ag nanoparticles (AgNPs) producing substrates that resemble the commercially manufactured product (Figure E.2B). At closer look under the microscope, the quartz fibers (Figure E.2C) in the purchased substrates were not nearly as thick as the paper fibers (Figure E.2D). Nonetheless, this difference did not seem to have any deleterious effects on SERS substrate performance as indicated in Figure E.3. To determine whether the paper-based SERS

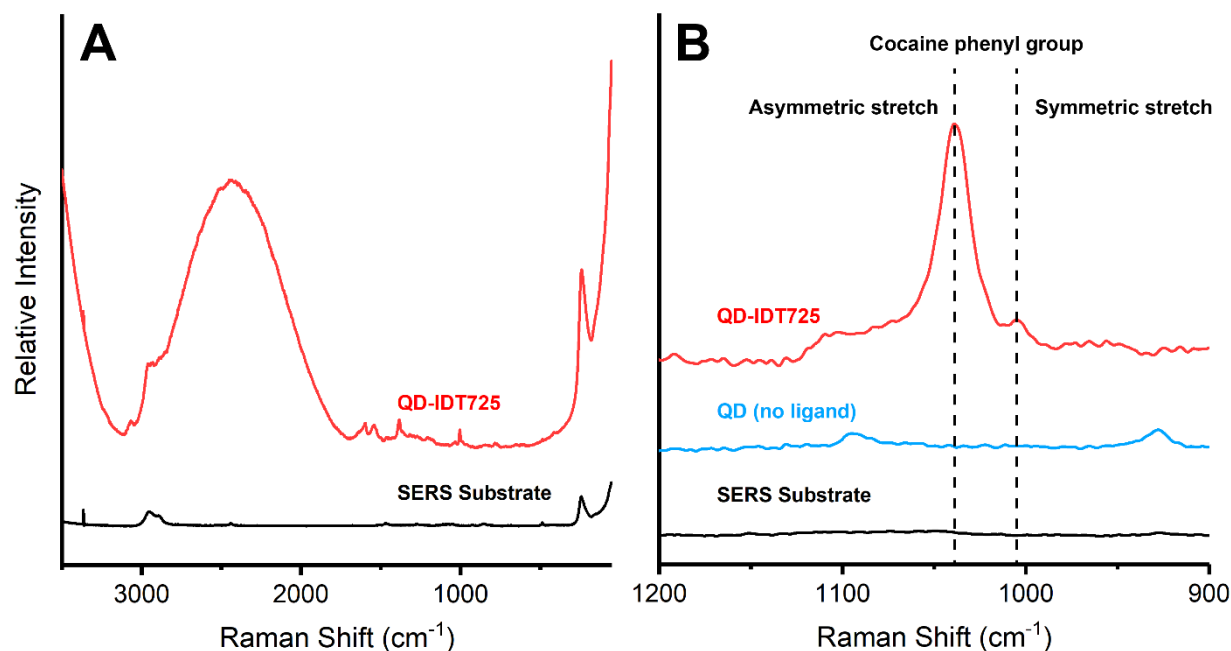


Figure E.1. Surface-enhanced Raman spectroscopy (SERS) of QD-IDT725 using Ag nanoparticle substrates. A) Wide spectral range of QD-IDT725 and the SERS substrate averaged spectra (N=25). B) Narrow spectral range of QD-IDT725, QD (no ligand), and the SERS substrate averaged spectra (N = 25). The cocaine phenyl group Raman modes are highlighted by the dashed lines (asymmetric stretch = 1038 cm^{-1} , symmetric stretch = 1004 cm^{-1}).

substrates were effective, Raman spectroscopy was performed on a ubiquitous SERS chemical standard (4-mercapto benzoic acid, MBA). Large peaks characteristic of enhanced MBA Raman modes were present and distinct from all negative controls, including paper pads only, paper pads soaked in dimethyl sulfoxide (DMSO), paper pads with MBA diluted in DMSO, AgNPs embedded in paper pads, and AgNP-embedded paper pads soaked in DMSO (Figure E.3). Although in-house produced substrates have yet to be used for analysis of QD probe structure, these results highlight the utility of these paper-based SERS substrates. In this regard, the use of these substrates could be an inexpensive and readily available alternative to the commercial substrates mentioned, ultimately improving throughput for characterizing ligand-conjugated QD probe structures.

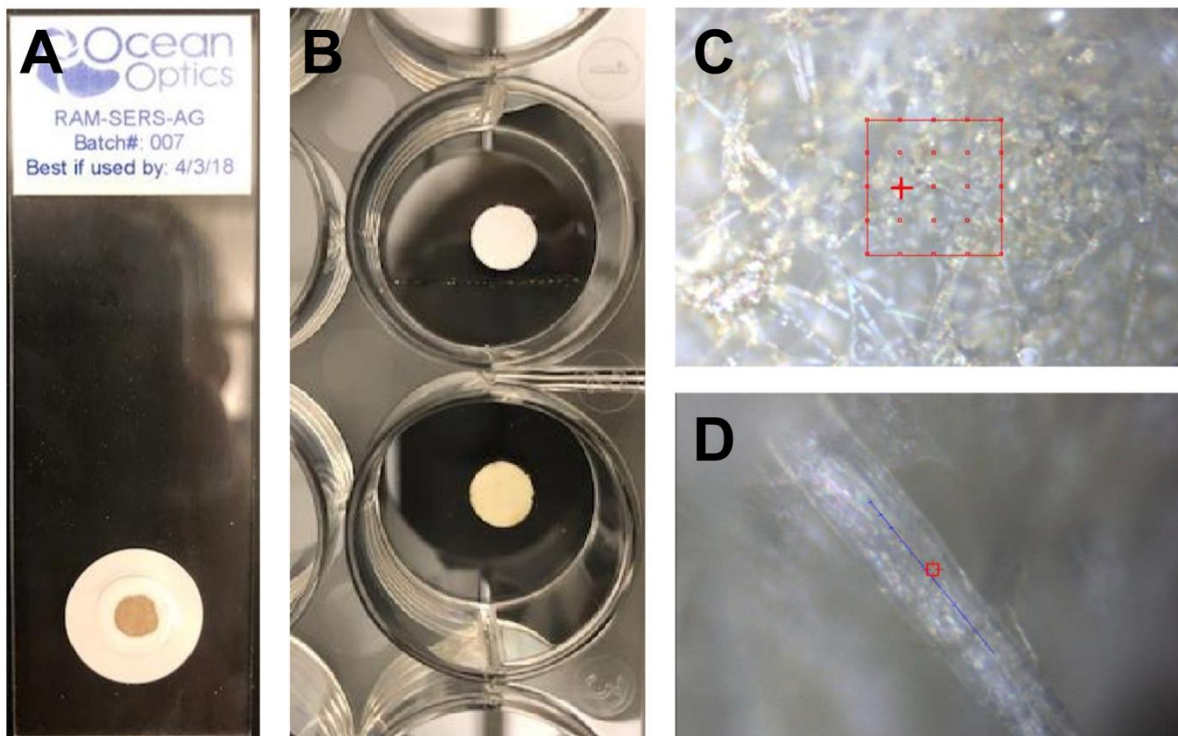


Figure E.2. Comparison of commercially available SERS substrates (Ocean Optics) to in-house produced paper-based SERS substrates. A) Photograph of a commercially available SERS substrate. B) Photograph of paper pads before (top) and after (bottom) incubation in a suspension of Ag nanoparticles. C) Brightfield microscopy image of the commercially available SERS substrate. D) Brightfield microscopy image of in-house produce paper-based SERS substrate.

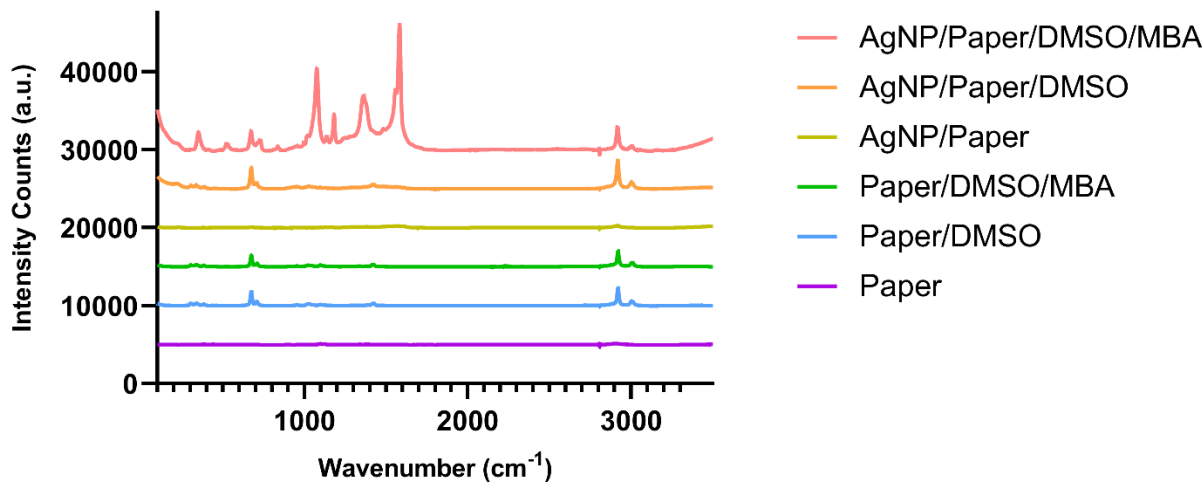


Figure E.3. Determining the effectiveness of the in-house produced SERS substrates. Stacked Raman spectra of AgNP-embedded paper pads with 4-mercapto benzoic acid (MBA, red) diluted in dimethyl sulfoxide compared to negative controls – AgNP-embedded paper pads soaked in DMSO (orange), AgNP-embedded paper pads (yellow), paper pads (without AgNP) with MBA diluted in DMSO (green), paper pads soaked in DMSO (blue), and bare paper pads (purple).

E.2 References

1. de Oliveira Penido, C. A. F., Pacheco, M. T. T., Lednev, I. K., and Silveira, L., Raman spectroscopy in forensic analysis: identification of cocaine and other illegal drugs of abuse, *J. Raman Spectrosc.*, **2016**, 47, 28-38.

APPENDIX F

STRUCTURAL CONFIRMATION OF IDT725-SUCCINIMIDYL ESTER

Coupling carboxylic acid groups to amines is commonly performed by EDC/NHS conjugation chemistry. In a typical reaction, the two coupling species are mixed with both EDC and NHS in one pot such that EDC catalyzes the generation of the succinimidyl ester (SE) for the amine to attack. NHS is cleaved and the resulting covalent bond is an amide. Because EDC quenches QD fluorescence, our approach to couple the acid-containing IDT725 compound to terminal amines on symm-shelled QDs involved generating and isolating the SE (IDT725SE) prior to QD amine coupling. A common concern in this conjugation chemistry is the hydrolysis of SEs, which renders the acid species unavailable for amine coupling. Considering the possibility of SE hydrolysis, a series of structural characterizations was performed by 2D nuclear magnetic resonance (NMR) spectroscopy, which in turn confirmed that the SE was intact prior to coupling. First, heteronuclear multiple bond correlation (HMBC, Figure F.1 and F.2) reveals that the protons (2.68 ppm) couple only to the SE carbonyls (172 ppm), confirming the SE is present. Only one CH₂ peak at 2.68 ppm for ¹H and 25.2 ppm for ¹³C in the heteronuclear single quantum coherence (HSQC, Figure F.3) spectra provides further confirmation that the SE is present. Additionally, ¹H Correlation Spectroscopy (COSY, Figure F.4) shows that SE backbone protons at 2.68 ppm couples only to themselves and not any other species, which confirms that this is an isolated spin system. Together, these spectra are evidence that the SE was still intact at the time of coupling.

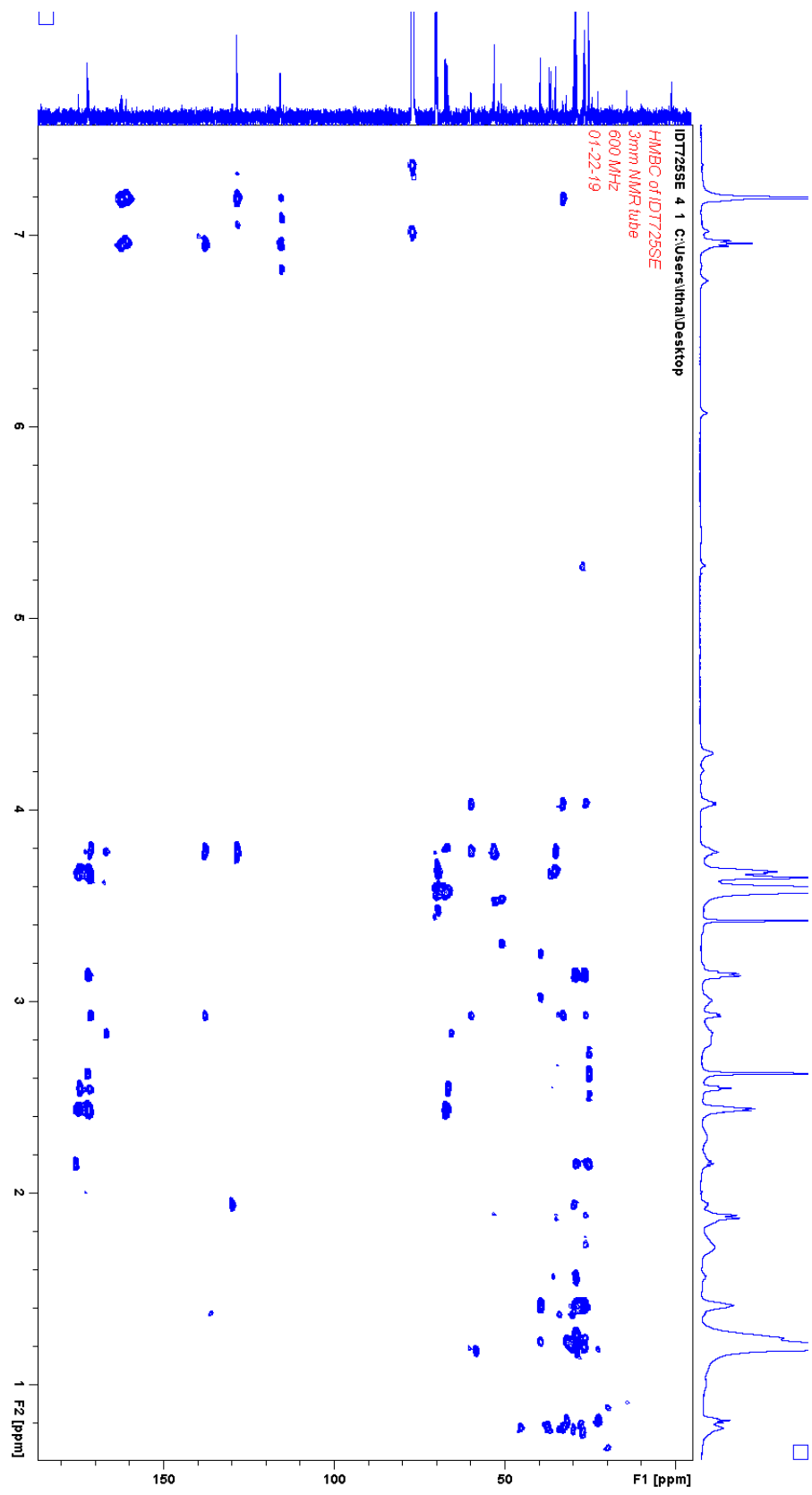


Figure F.1. HMBC of IDT725SE (600 MHz, CDCl₃).

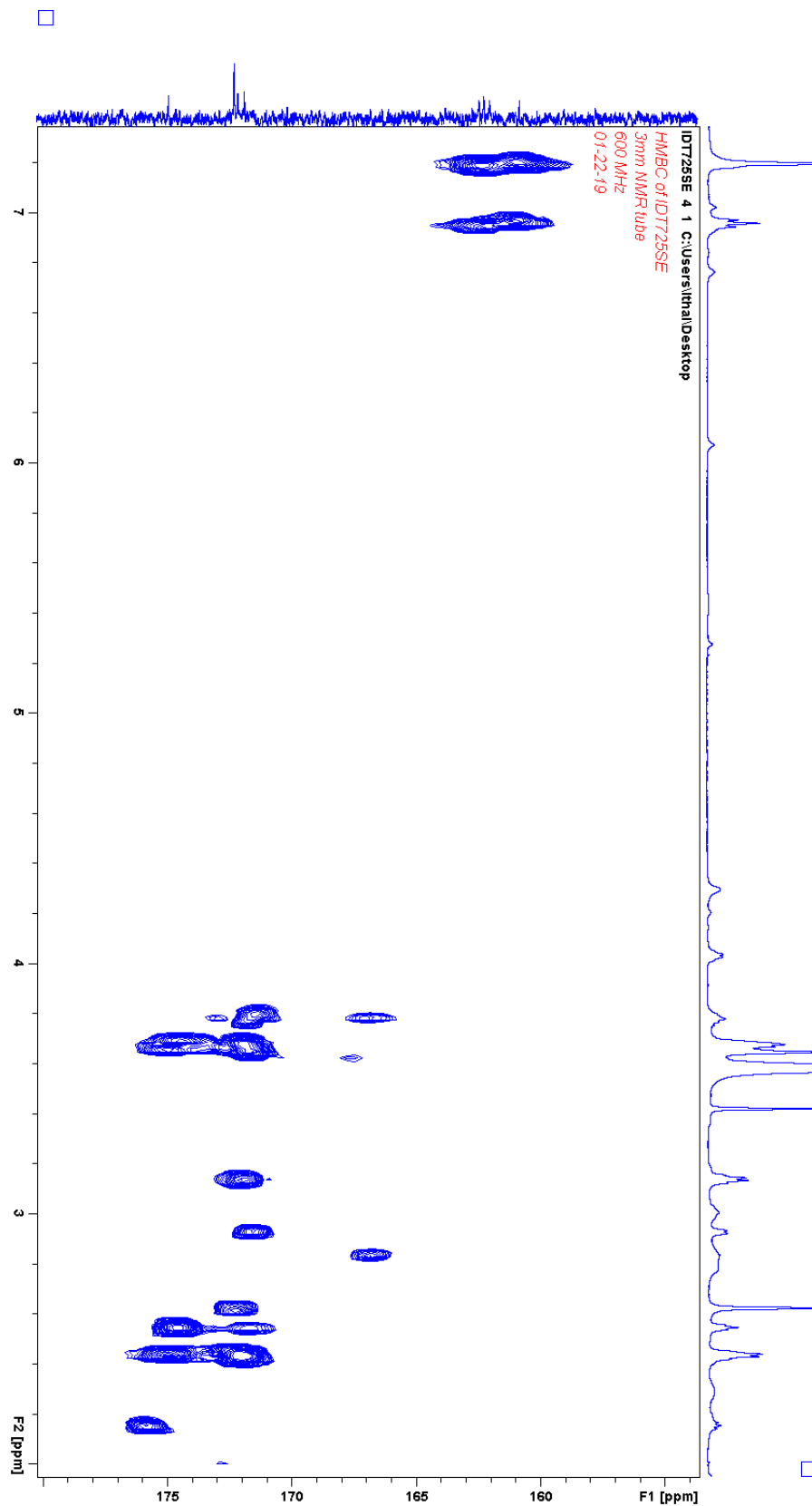


Figure F.2. HMBC of IDT725SE (600 MHz, CDCl_3 , subset around ^{13}C 172 ppm).

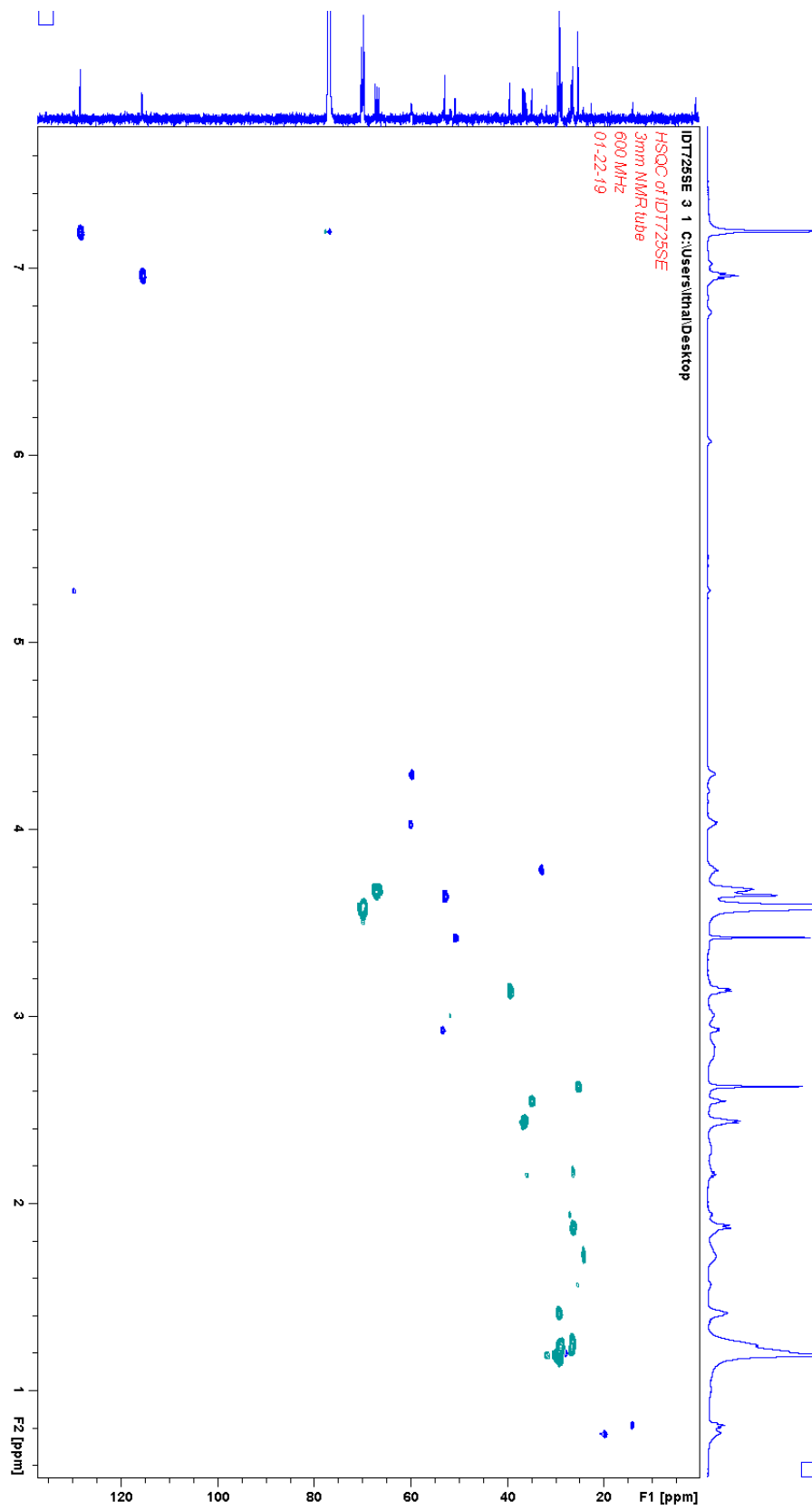


Figure F.3. HSQC of IDT725SE (600 MHz, CDCl_3).

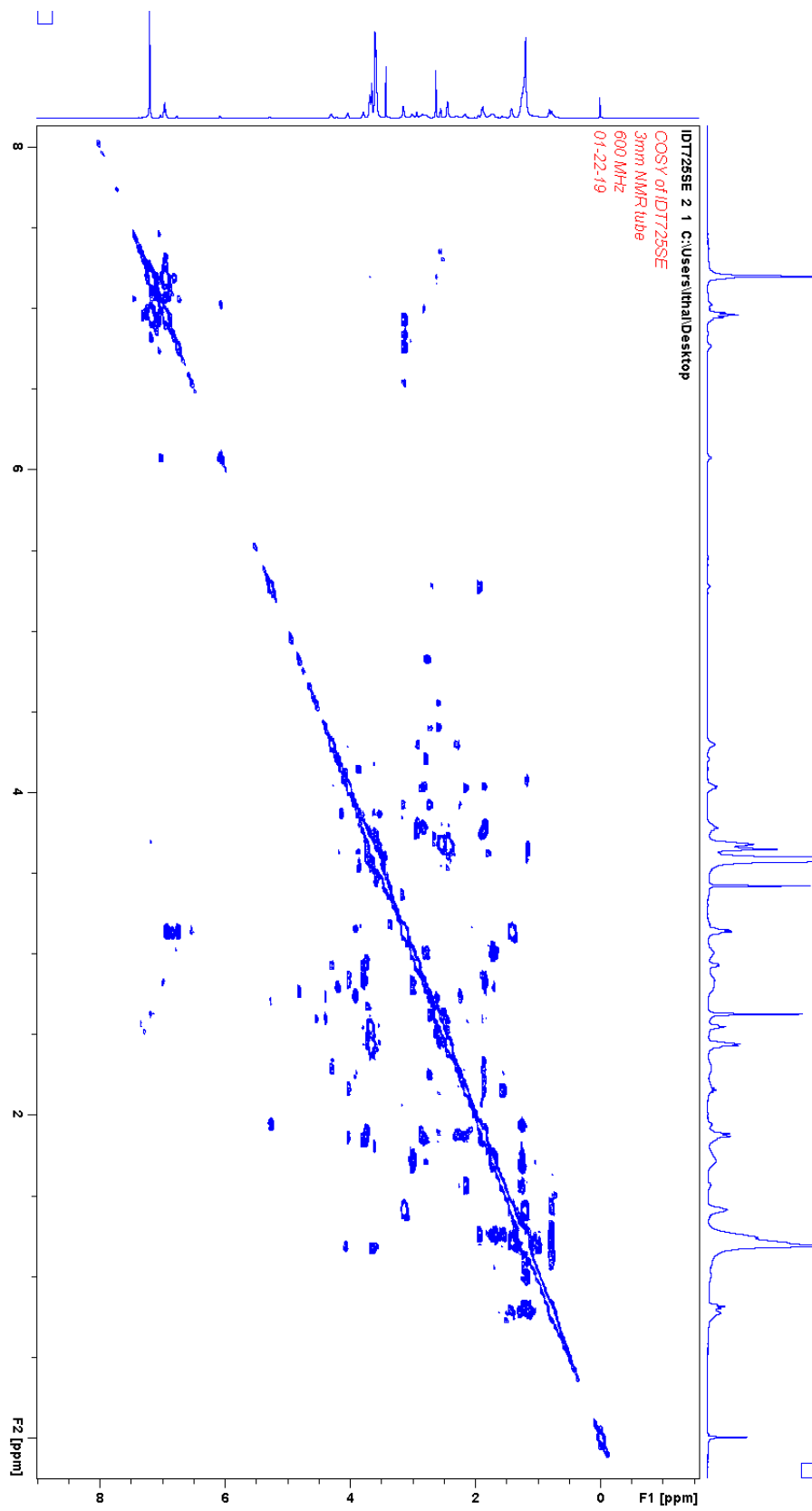


Figure F.4. COSY of IDT725SE (600 MHz, CDCl_3).

APPENDIX G

SINGLE PARTICLE ANALYSIS OF CADMIUM-FREE QUANTUM DOTS IN AMBIENT AMOSPHERE

Elements of this section are derived from Reid, K. R., McBride, J. R., Freymeyer, N. J., Thal, L. B., and Rosenthal, S. J., Chemical Structure, Ensemble and Single-Particle Spectroscopy of Thick-Shell InP–ZnSe Quantum Dots, Nano Lett., 2018, 18, 709–716. Copyright 2018. American Chemical Society.

Cd toxicity is a concern shared across the biological imaging community. Although amphiphilic polymer encapsulation and PEGylation mitigates cytotoxic effects of Cd-containing quantum dots (QDs) (see section 4.2.4),¹ exclusion of Cd in QD composition is the next step in the development of less toxic probes. In the interest of developing high performing Cd-free quantum dots, we synthesized InP/ZnSe core/shell quantum dots. While InP is an attractive non-Cd semiconductor candidate for QDs due to the size-tunability across the visible to near-IR window and the lower intrinsic toxicity,^{2,3} InP QDs suffer from synthetically induced broad size distributions, and have relatively low photoluminescence (PL) quantum yields (QYs) and poor environmental stability.⁴ This work highlighted these core/shell heterostructures performance with high ON-time fractions that can exceed 95% and a 7-fold increase in the biexciton lifetime compared to large lattice mismatched ZnS-shelled QDs. Intriguingly, energy-dispersive X-ray spectroscopy chemical maps show indium was incorporated in the shell of these QDs (Figure G.1), which is a likely culprit of the poor quantum yields previously reported.

Concomitantly, these QDs did not suffer from poor environmental stability at the single

particle level. Using a fast-scanning spinning-disk confocal microscope, we imaged drop-casted InP/ZnSe QDs to generate single-emitter intensity traces (Figure G.2). The large ON fraction over a period of 5 minutes under ambient atmosphere highlights these QDs environmental stability and the possibility of InP-based QDs to be used in single particle biological imaging experiments.

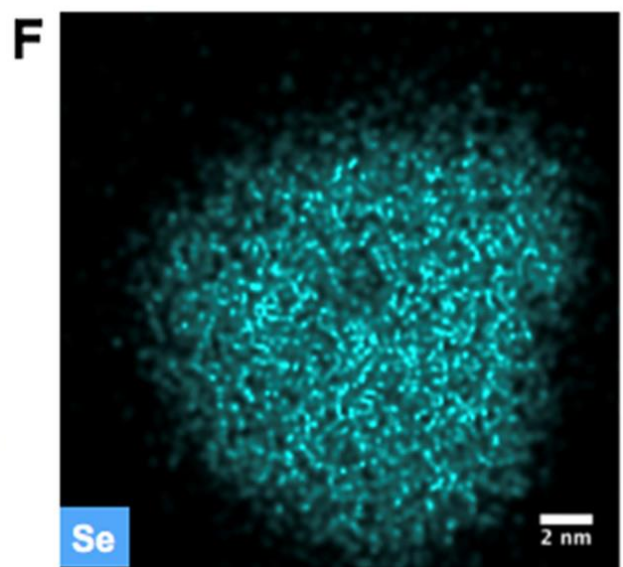
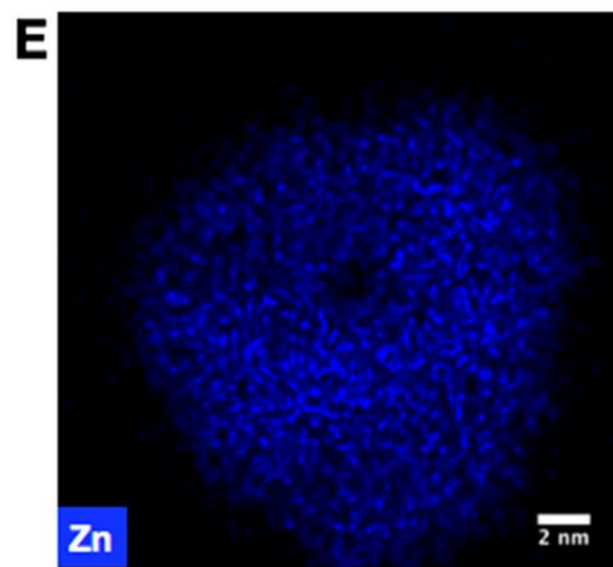
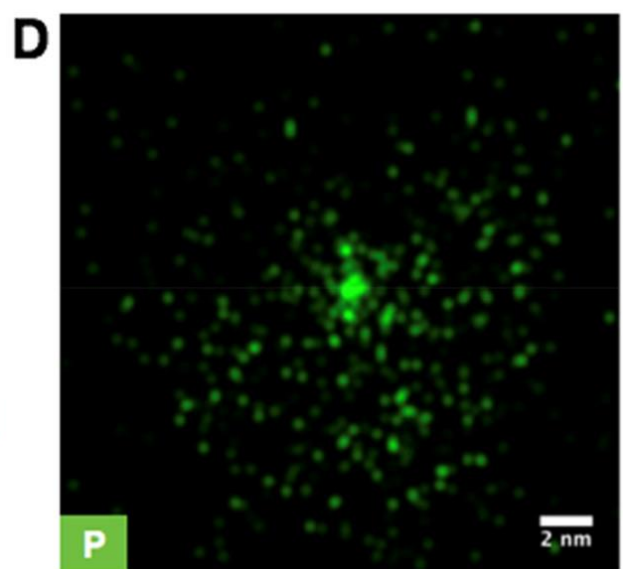
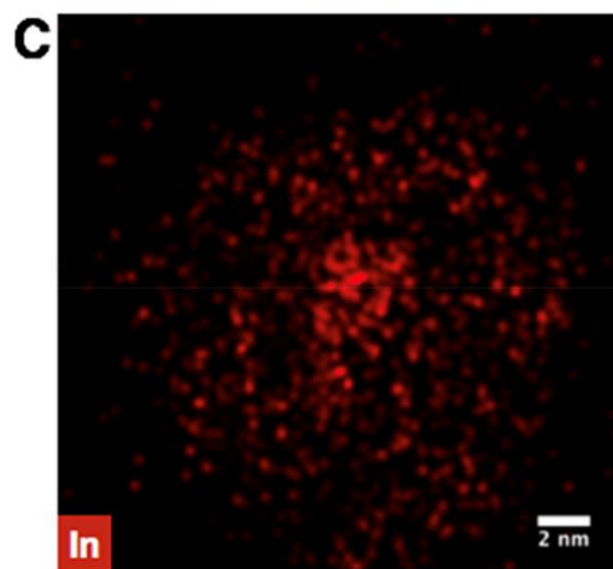
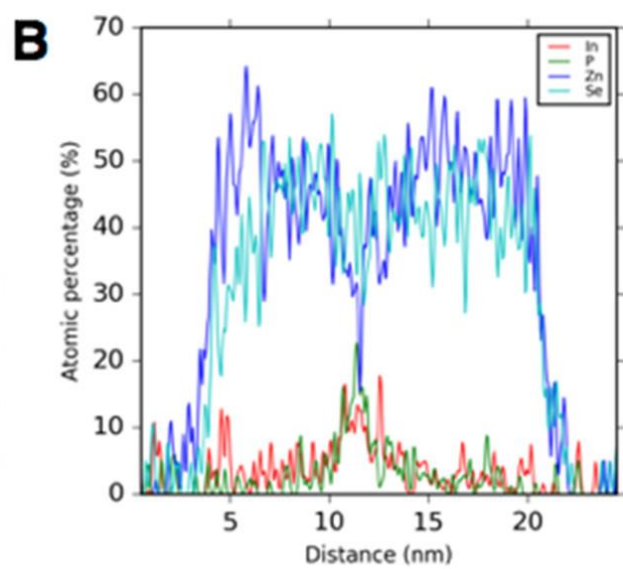
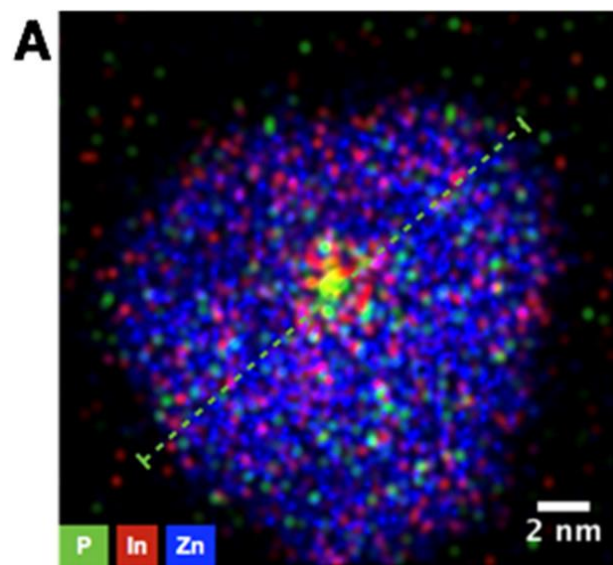


Figure G.1. Elemental characterization of thick-shell InP–ZnSe QDs. (A) Energy dispersive X-ray (EDX) chemical map of a core–shell InP–ZnSe QD. (B) Corresponding line scan showing the intensity profile of each element across the diameter of the particle. (C) Indium, (D) phosphorus, (E) zinc, and (F) selenium chemical maps from the particle in part A.

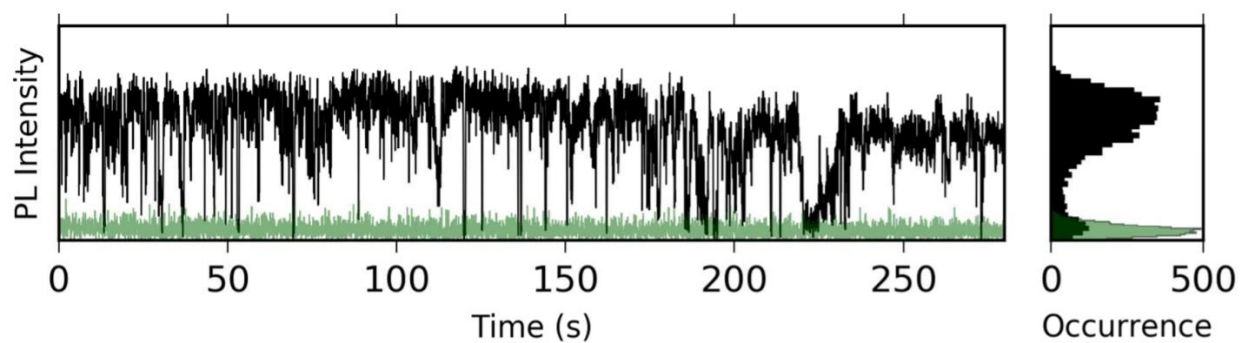


Figure G.2. Blinking trace and intensity histogram of an individual thick-shell InP-ZnSe QD recorded in air using a low energy excitation source (488 nm, 2.5 eV). The background (green trace) was recorded from a region with no QDs.

F.2 References

1. Thal, L.B., Mann, V.R., Sprinzen, D., McBride, J.R., Reid, K.R., Tomlinson, I.D., McMahon, D.G., Cohen, B.E., and Rosenthal S.J., Ligand-conjugated quantum dots for fast sub-diffraction protein tracking in acute brain slices, *Biomater Sci.* **2020**, *Advance Article*.
2. Xie, R., Battaglia, D., and Peng, X., Colloidal InP Nanocrystals as Efficient Emitters Covering Blue to Near-Infrared, *J. Am. Chem. Soc.*, **2007**, 129, 15432-15433.
3. Brunetti, V., Chibli, H., Fiammengo, R., Galeone, A., Malvindi, M.A., Vecchio, G., Cingolani, R., Nadeau, J.L., Pompa, P.P., InP/ZnS as a safer alternative to CdSe/ZnS core/shell quantum dots: in vitro and in vivo toxicity assessment, *Nanoscale*, **2013**, 5, 307-17.
4. Tamang, S., Lincheneau, C., Hermans, Y., Jeong, S., Reiss, P., Chemistry of InP Nanocrystal Syntheses, *Chem. Mater.*, **2016**, 28, 2491-2506.